Dual-Wavelength Internal-Optically-Pumped Semiconductor Laser Diodes

by

Benjamin Green

A Dissertation Presented in Partial Fulfillment
of the Requirements for the Degree
Doctor of Philosophy

Approved November 2011 by the
Graduate Supervisory Committee:

Yong-Hang Zhang, Chair
Cun-Zheng Ning
Nongjian Tao
Ronald Roedel

ARIZONA STATE UNIVERSITY

December 2011

ABSTRACT

Dual-wavelength laser sources have various existing and potential applications in wavelength division multiplexing, differential techniques in spectroscopy for chemical sensing, multiple-wavelength interferometry, terahertz-wave generation, microelectromechanical systems, and microfluidic lab-on-chip systems. In the drive for ever smaller and increasingly mobile electronic devices, dual-wavelength coherent light output from a single semiconductor laser diode would enable further advances and deployment of these technologies. The output of conventional laser diodes is however limited to a single wavelength band with a few subsequent lasing modes depending on the device design. This thesis investigates a novel semiconductor laser device design with a single cavity waveguide capable of dual-wavelength laser output with large spectral separation.

The novel dual-wavelength semiconductor laser diode uses two shorter- and longer-wavelength active regions that have separate electron and hole quasi-Fermi energy levels and carrier distributions. The shorter-wavelength active region is based on electrical injection as in conventional laser diodes, and the longer-wavelength active region is then pumped optically by the internal optical field of the shorter-wavelength laser mode, resulting in stable dual-wavelength laser emission at two different wavelengths quite far apart.

Different designs of the device are studied using a theoretical model developed in this work to describe the internal optical pumping scheme. The carrier transport and separation of the quasi-Fermi distributions are then modeled using a software package that solves Poisson's equation and the continuity

equations to simulate semiconductor devices. Three different designs are grown using molecular beam epitaxy, and broad-area-contact laser diodes are processed using conventional methods. The modeling and experimental results of the first generation design indicate that the optical confinement factor of the longer-wavelength active region is a critical element in realizing dual-wavelength laser output. The modeling predicts lower laser thresholds for the second and third generation designs; however, the experimental results of the second and third generation devices confirm challenges related to the epitaxial growth of the structures in eventually demonstrating dual-wavelength laser output.

DEDICATION

To Amy for her constant love, support, and motivation in this journey. Without her I never would have accomplished that which I have, nor would I be the person that I am today.

To our girls, Hailey and Kiersten. Their gentle smiles always remind me what is most important in life and the joy there is in simplicity. I'm grateful to the many sacrifices Amy and our girls have made to allow me to pursue my goals.

Finally, to my Father who has given me so much and been so loving and patient in extending His tender mercies to me.

ACKNOWLEDGMENTS

I would like to thank Dr. Yong-Hang Zhang for his support and guidance in conducting this doctoral research and for his motivation in the educational process. I express my gratitude to the committee members, Dr. Nongjian Tao, Dr. Cun-Zheng Ning, and Dr. Ronald Roedel. I am grateful to those who provided mentoring in my first years as a graduate researcher, and I thank Shui-Qing (Fisher) Yu and Stephen Sweeney for their instruction and advice in those years. I would also like to thank Songnan Wu and Elizabeth Steenbergen for their friendships and the many conversations we enjoyed during these years of graduate school, and my associations with the following have helped make the experience overall an enjoyable one: Ding Ding, Kevin O'Brien, Shane Johnson, Robin Scott, Hank Dettlaff, Michael DiNezza, Jingjing Li, and Jin Fan.

I would like to thank Shi Liu for his assistance in conducting the last set of photoluminescence measurements, and I thank Kalyan Nunna, Fisher, and Dongsheng Fan for the epitaxial growth and processing of the later generation designs of the unique dual-wavelength semiconductor laser diode. I acknowledge the financial support of the National Science Foundation and Arizona Board of Regents in conducting this research. I am also deeply grateful to William and Terry Wilhoit for their financial support through the ARCS Foundation.

Finally, I thank my parents for their love and support and for teaching me to value education and hard work.

TABLE OF CONTENTS

Page

LIST OF TABLES

Table Page

LIST OF FIGURES

Figure Page

Figure Page

Figure Page

Figure Page

Figure Page

1 Introduction

Over the last half of a century advancements have been made in the design, performance, and manufacturing of semiconductor laser diodes such that they are nearly ubiquitous today in a host of applications. The impact of laser diodes has been revolutionary both economically and socially with applications ranging from telecommunications, the internet, media storage, security, sensing, biology, to medicine. The history and development of the laser diode is marked with many creative ideas and engineering of semiconductor physics to overcome then current limitations, and many of these advancements relate either to: 1) reducing the laser threshold current density; 2) achieving laser output at new wavelengths with new materials; or 3) improving the modulation bandwidth, characteristic temperature, spectral width, or other parameters key to communication applications.

The inherent nature of carrier scattering and the band structures in conventional semiconductor laser diodes results in laser output which is generally considered as being at a single wavelength with subsequent spectral modes depending on the type of laser diode. In this work a novel semiconductor laser diode design is investigated to enable simultaneous laser output at two wavelengths that have a large spectral separation by using two asymmetric active regions and a creative internal optical pumping scheme. To begin, a brief review of some of the most creative ideas and advancements in laser diode device

technology is given, and then a high-level introduction of the novel dual-wavelength laser diode is presented along with its potential applications.

I. CREATIVE ADVANCEMENTS OF LASER DIODES

Multiple individuals and research groups were involved in the early development and invention of the first semiconductor laser diodes. As to whom the true inventor of the laser diode is, there is still today some debate, and an excellent review of the different parties and their contributions is provided by Dupuis [1]. Dupuis notes John von Neumann as the first to suggest using carrier injection in a semiconductor *p*-*n* junction to upset carrier equilibrium to achieve stimulated emission and create an amplifier of incident radiation. His ideas were originally part of an unpublished manuscript written in 1953, a year before Charles Townes, James Gordon, and Herbert Zeiger demonstrated the first maser at Columbia University in 1954 [2]. (Although von Neumann's manuscript was later historically included in a 1987 issue of IEEE Journal of Quantum Electronics reviewing the invention of the semiconductor laser [3].)

Among the other contributors Dupuis notes are Bernard and Duraffourg as the first to publish a paper using quasi-Fermi levels to describe the requirements for carrier population inversion inside a semiconductor *p*-*n* junction in 1961 [4], and Nikolai G. Basov in the Soviet Union for suggesting the use of heavily-degenerate *p*-*n* junctions to establish the necessary population inversion of carriers and using the change in the index of refraction due to the heavy doping as a waveguide [5]. Dupuis provides a detailed review of the many groups working independently at that time who were proposing similar ideas for using *p*-*n*

junctions to realize semiconductor lasers, but he carefully notes that none of the groups had the complete theory correct [1].

Experimentally, the first semiconductor laser diodes were demonstrated in 1962 by four groups working independently. Robert N. Hall *et al.* at General Electric R&D Labs are widely acknowledged as the first to experimentally demonstrate a semiconductor laser diode in 1962, although at liquid nitrogen temperatures and under high pulsed current [6]. On the same day the results were published in Physical Review Letters, another paper by Marshall I. Nathan *et al*. at IBM appeared in Applied Physics Letters also announcing experimental evidence of laser emission from a semiconductor diode, however their manuscript was received 10 days after Hall's paper [7]. The devices of both groups were infrared GaAs *p-n* homojunctions, and only a few weeks later, Nick Holonyak, who was also at General Electric, was the first to report visible laser emission using $GaAs_{1-x}P_x$ junctions [8]. The fourth group to demonstrate a semiconductor laser diode was T. M. Quist *et al*. at Lincoln Laboratory, and their paper was received only one month after Hall's first [9].

These first laser diodes were all *p-n* homojunction devices and operated only at cryogenic temperatures or under high pulsed currents. In 1963, Herbert Kroemer and Zhores Alferov independently proposed double heterostructure laser diodes to improve carrier confinement and reduce the laser thresholds [10], [11]. In heterojunctions, the injected carriers are confined by the heterobarriers, and larger carrier densities not possible in homojunctions are realized. Kroemer noted that with wider-gap layers on the sides of the "radiative semiconductor layer,"

quasi-Fermi level separations greater than the radiative active region band gap are possible. In 1970 Alferov's group in the former Soviet Union was the first to demonstrate continuous-wave (CW), operation of a laser diode at room temperature by using a double heterostructure design, and shortly after Hayashi and Panish in the United States also reported CW operation [12], [13]. In 2000, Kroemer and Alferov shared the Noble Prize in physics for their creative proposal of double heterostructures.

In 1973 while working on some simple calculations of slab optical waveguides for integrated optics, Charles H. Henry at Bell Laboratories recognized a correlation between the confinement of light in a slab waveguide and the confinement of electrons in the potential well created by a thin heterostructure or quantum well [14]. He proposed there should be discrete modes or levels in a quantum well (QW), and the absorption edge should contain a series of discrete steps. At that time the thinnest heterostructure layers that could be grown using liquid phase epitaxy were near 200 nm, but A. Y. Cho, also at Bell Labs, was developing molecular beam epitaxy (MBE), into a reliable and alternative method for growing semiconductor heterostructures with near atomic monolayer precision. Using a thin MBE-grown GaAs/AlGaAs heterostructure, Dingle, Wiegmann, and Henry in 1974 reported the first absorption spectra that clearly showed a distinct series of steps indicative of quantum confinement in the heterostructure [15]. They quickly filed a patent application in 1975 claiming both reduced thresholds in laser diodes with quantum well active regions and the ability to tune the laser wavelength by adjusting the well thickness, and the

earliest quantum well laser diodes were reported in the late 1970s by Dupuis and Dapkus of Rockwell International in collaboration with Holonyak at the University of Illinois using metal organic chemical vapor deposition (MOCVD), [16]-[19].

Demonstration of MBE-grown quantum well laser diodes was not realized until later due to the low quality and very short nonradiative lifetimes of the AlGaAs layers. Absorption of carbon and oxygen while growing AlGaAs leads to defects and nonradiative recombination centers, and early improvements of MBE sought to eliminate hydrocarbon and water vapor sources. These improvements included Ti sublimation and liquid-nitrogen-cooled shrouds to significantly reduce residual carbon-containing gases [20]. W. T. Tsang, who was also at Bell Labs, added an interlock chamber to keep the growth chamber under ultrahigh vacuum, and with other improvements reported MBE-grown double heterostructure lasers with current thresholds as low as similar devices grown by other methods [21]. Tsang also improved the material quality of AlGaAs layers by increasing the growth temperature of AlGaAs, observing a four times reduction in laser threshold when the AlGaAs growth temperature was increased from ~ 500 °C to over 620 °C [22], [23]. Further, Tsang optimized the barrier heights, barrier widths, and quantum well thicknesses in a multiple-quantum-well $GaAs/Al_xGa_{1-x}As$ structure to reach threshold current densities as low as 250 A/cm^2 [24]. Finally, Tsang noted continued reductions in the thresholds of laser diodes using a graded-index waveguide separate-confinement heterostructure (GRINSCH) due to increases of the optical confinement factor of the active

region with Schubert later noting improved carrier injection into the active region of laser diodes using graded-index heterostructures [25], [26].

The development of quantum well active regions resulted in lower threshold current densities, higher differential gains, and larger characteristic temperatures for laser diodes. Many of these improvements are results of the one-dimensional quantum confinement and change in the electronic density of states. Arakawa and Sakaki at the University of Tokyo, proposed continued advances with additional quantum confinement in the other dimensions and were the first to propose quantum dot lasers in 1982 [27]. However, it was not until the development of the Stranski-Krastanow method that the epitaxial growth of quantum dot layers was realized and the first quantum dot lasers were demonstrated. Some of the first quantum dot lasers were reported in 1994 by Bimberg's group at Technical University Berlin working together with Ledentsov's group at St. Peterburg's Ioffe Institute [28]. The devices had low thresholds and large characteristic temperatures at low temperature, but at room temperatures the performance was worse than quantum well devices, and it wasn't until 1996 that room-temperature CW operation was realized by a group at the University of Michigan [29]. Finally in 1999, Lester's group at the University of New Mexico was the first to report quantum dot lasers with thresholds lower than quantum well lasers [30]. By positioning the dots within a quantum well ("dots-in-a-well or DWELL"), Lester *et al.* reported thresholds of 26 A/cm^2, the lowest of any semiconductor laser diode to that point.

In addition to the creative advancements using heterostructures and nanostructures to improve the threshold and performance of laser diodes, creative research has extended the range of wavelengths at which laser diodes can be made. Despite the availability of compound semiconductor alloys with direct band gaps with corresponding wavelengths from ~ 200 nm to past 7 μm, laser diodes have not been realized at all these wavelengths due to problems related to efficiencies, doping, and adequate lattice-matched substrates. The GaAs/AlGaAs material system is well developed with λ ~870 nm. Laser diodes at this wavelength are often used for short-distance communication and local-area networks, whereas for long distance optical fiber transmission in telecommunications, lasers at 1.3 μm and 1.5 μm are used due to the minimum dispersion and minimum absorption loss of optical fibers at these wavelengths. The main material system at these wavelengths is the quaternary $In_{1-x}Ga_xAs_yP_{1-y}$/InP [31]. For laser emission at even longer wavelengths, the quantum cascade laser, developed at Bell Labs by Federico Capasso relies on intersubband transitions rather than direct interband transitions to enable laser output at mid and far infrared wavelengths (2-70 μm), [32]. The unique design of quantum cascade lasers has led to the realization of laser diodes with wavelengths even longer than the smallest III-V band gap for applications in chemical sensing and terahertz generation.

At the visible wavelengths, light-emitting diodes have been developed for nearly all the visible colors; however, laser diodes have not been achieved at all these wavelengths. For red laser diodes, the quaternary semiconductor (Al_xGa_{1-}

$_x)_{0.5}In_{0.5}P$ lattice-matched to GaAs covers the longer visible wavelengths in addition to the near infrared, and DVD players and red laser pointers use $In_{0.5}Ga_{0.5}P$ active regions to emit at 650 nm. At the other end of the visible spectrum, S. Nakamura at Nichia Chemical in Japan and later at the University of California, Santa Barbara, was the pioneer leader in the development of blue laser diodes using GaN-based semiconductors. In 1996, his group was the first to report a room-temperature CW blue laser diode at 408.3 nm with a device that consisted of three $In_{0.2}Ga_{0.8}N$ quantum wells each 4 nm wide separated by 8 nm $In_{0.05}Ga_{0.95}N$ barriers [33].

II. DUAL-WAVELENGTH SEMICONDUCTOR LASER DIODES USING INTERNAL OPTICAL PUMPING

A small area of the continued research and development associated with laser diodes relates to creative approaches to achieve multi-wavelength laser output for certain applications such as wavelength division multiplexing, differential techniques in spectroscopy and sensing, multiple-wavelength interferometry, and THz generation. Initially the largest driving force for research on dual-wavelength laser diode sources was for use in optical communications and wavelength division multiplexing. With different modulated wavelength sources, multiple channels can propagate simultaneously within a single fiber optic cable with little crosstalk, and wavelength division multiplexing can be used to increase the capacity of an existing fiber network without the need to lay additional fiber. In this application, ideally the spectral separation between the

laser modes should be minimal to match the losses and dispersion of the different channels.

Another application for dual-wavelength laser sources is chemical and gas sensing using differential spectroscopy techniques. In this approach, a medium is probed using two different laser wavelengths, one at a resonant absorption wavelength λ_{abs} and the other a reference wavelength that is an off-resonant wavelength λ_{ref}. The intensity of the transmitted or backscattered light at the absorbed wavelength λ_{abs} is compared to that of the unabsorbed wavelength λ_{ref}. With this differential technique, linear and absolute measurements can be made that are independent of other environmental factors [34]. The method has been implemented in a range of applications from remote sensing of trace gases in the atmosphere and differential absorption lidar [34], [35], to fiber optic based sensors for measuring pH, pressure, temperature, and other bio-parameters within the human body [36], [37]. Another application for dual-wavelength lasers is multi-wavelength interferometry since the degree of ambiguity in optical path-length and surface profile measurements can be decreased with techniques involving multiple wavelengths [38]. Dual-wavelength laser output can also be used in the generation of THz radiation through wave-mixing for its uses spectroscopy, biomedical imaging, DNA analysis, communication systems, and security imaging [39].

Often for these applications, the needed multi-wavelength laser signal is achieved by combining the output of multiple laser sources through various optical elements. There is a continued demand however in today's fast-paced

climate for miniaturization and increased mobility of electronic devices. Dual-wavelength laser output from a single diode device would enable such advances in the applications noted here, and with increased mobility and reduction in costs, it is easy to envision the emergence of new applications. Future ideas include integrating a dual-wavelength laser diode in small-footprint devices where two laser wavelengths within the same optical beam would be highly advantageous, such as in microelectromechanical systems and/or lab-on-chip microfluidic systems.

The challenge in realizing dual-wavelength output from a single laser diode is that carrier scattering and quasi thermal equilibration within the active junction region limit laser output to what is generally considered single-wavelength with possible subsequent spectral modes depending on the laser design. In a diode junction region with asymmetric quantum wells of different effective band gaps or transition energies, the carrier dynamics and thermal equilibration result in a single electron/hole quasi-Fermi level and distribution that extends across the junction active region as illustrated in Fig. 1.1. This scattering and broadening prevents sustaining simultaneous stable laser output from both quantum wells if the two wavelengths are very different. With applied current to the laser diode, carriers are injected and band filling occurs starting at the lowest energy quantum well, and the spontaneous emission and gain spectra increase with continued injection of carriers into the active region. At laser threshold the carrier concentration, gain, and quasi-Fermi levels theoretically become fixed due to the high recombination rate of the stimulated emission, and this pinning of the

carrier concentration prevents any further increase of the gain to achieve laser threshold at shorter wavelengths.

To enable dual-wavelength laser output at wavelengths with large spectral separation from a single *p-i-n* junction device and waveguide, a creative laser diode design with dual active region is introduced that decouples the quasi-Fermi levels/distributions of the two regions and uses a novel internal optical pumping scheme. This novel internal-optically-pumped dual-wavelength laser design is illustrated in Fig. 1.2. The first laser active region, termed the master active region, consists of a larger band gap material placed within the junction of the diode as in conventional laser diode devices, and the second laser active region, termed the slave active region, consists of a smaller band gap material placed outside the *p-n* junction but still within the guided optical field of the cavity waveguide. The placement of the two active regions prevents quasi thermal equilibration or decouples the quasi-Fermi levels between the two regions. The master active region is driven by the applied current as in conventional laser diodes, and a portion of the shorter-wavelength laser emission from this master laser then optically pumps the longer-wavelength slave region to its laser threshold, resulting in simultaneous laser output at two wavelengths with large spectral separation. The master and slave regions are considered separate active regions based on the decoupled quasi-Fermi levels and the different methods for carrier injection.

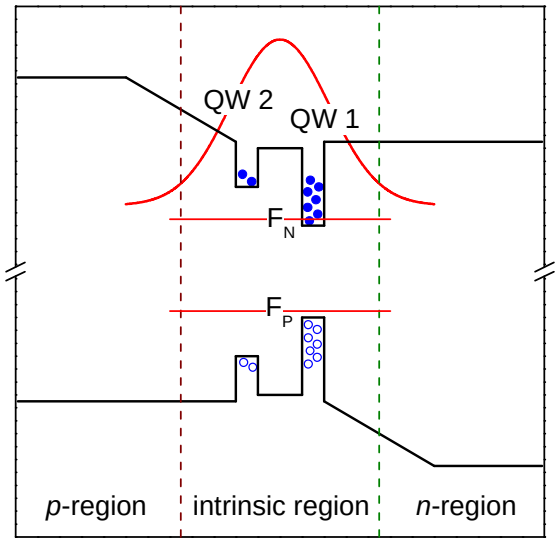

Conventional MQW laser diode band diagram

Fig. 1.1. Conceptual band diagram of a conventional multiple-quantum-well laser diode with asymmetric quantum wells sharing common quasi-Fermi levels.

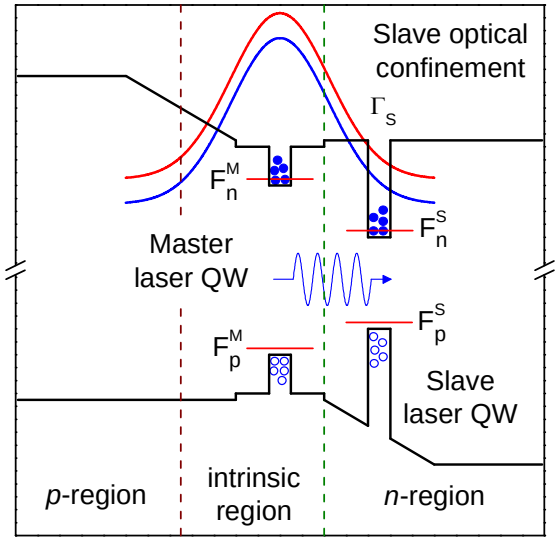

Novel internal-optically-pumped DWLD band diagram

Fig. 1.2. Conceptual diagram of the novel dual-wavelength laser design with decoupled quasi-Fermi levels and internal optical pumping.

The research presented here covers detailed theoretical modeling to specific device designs and efforts to demonstrate the novel dual-wavelength laser diode experimentally. First, an overview of previous multi-wavelength laser diode research by other groups is given in chapter two. A theoretical model is developed in chapter three of the internal optical pumping scheme, and the key parameters in optimizing the device performance are identified. Chapter four discusses other modeling methods used in developing and predicting the performance of actual device designs, and chapter five covers the experimental methods related to epitaxy growth, device processing, and device testing. The modeling and experimental results of three generations of dual-wavelength laser diode designs are then presented in chapters six and seven.

2 Previous Research on Dual-Wavelength Laser Diodes

Conventional semiconductor laser diodes are nearly single-wavelength devices or at least devices with a single wavelength band supporting a few subsequent spectral modes. Applications for laser diodes consisting of two wavelength bands far apart in the optical spectrum were noted in the previous chapter. The difficulty of achieving such a device with conventional laser diode designs was also pointed out as carrier scattering and quasi thermal equilibration result in carriers preferentially populating the lower energy active region or longer wavelength band. It is then difficult to populate a second shorter wavelength active region and produce the desired dual-wavelength output.

This chapter reviews previous research by other groups in developing dual-wavelength laser diodes, which is categorized into four groups. The first group includes approaches to engineer the resonant cavity of a semiconductor laser to selective support laser output from two non-subsequent longitudinal modes (or lateral modes in vertical cavity device), with the same gain medium. The spectral difference of these devices is not very large as the modes are supported by the same gain medium or the same wavelength band. Hence there are also mode-competition and stability issues with these devices. The second area of research is efforts to produce two laser diodes with different wavelengths monolithically on the same chip in close proximity. Some of the early literature labels these devices as dual-wavelength lasers wherein they are really monolithic arrays of individual devices. The third category relates to the research and

development of asymmetric multiple-quantum-well (AMQW), laser diodes where multiple quantum wells with different dimensions or material band gaps are located within a diode junction and the carrier dynamics are modulated by unique heterostructure designs. There are however limitations to the design and performance of these devices. Finally the fourth group relates to research on optically-pumped dual-wavelength devices, and their relation to the internal optical pumping scheme and the novel dual-wavelength laser diode introduced will be covered.

I. ENGINEERING THE RESONANT CAVITY

Different research groups have sought to modify the resonant cavity of semiconductor lasers to enable dual-wavelength laser operation. Independently, two groups in Taiwan and Germany developed two-color lasers using a special external cavity design [40], [39]. The designs use a laser-diode array with an antireflection coating on the front facet and then use an external diffraction grating at grazing incidence for wavelength selection and output coupling. The first-order reflection of the grating is focused on an end mirror that has a V-shaped double slit placed immediately in front of it to select two cavity resonant wavelengths. Horizontal translation of the slit leads to tandem tuning of the two wavelengths, and vertical translation controls the spectral difference of the modes. The spectral separation of the two modes is limited by the gain bandwidth of the semiconductor active region, and the largest separation demonstrated was 17 nm [41]. Concerning competition of the two laser modes, it was noted from the far-

field pattern that the two laser modes were initially using different gain regions of the laser diode array, and when a single laser diode was used, stable simultaneous dual-wavelength output due to strong mode competition was difficult to achieve [41].

A few groups have sought to realize dual-wavelength laser diodes without an external cavity by altering the distributed Bragg reflector (DBR), of DBR laser diodes. Iio *et al.* first demonstrated DBR laser diodes with output at two wavelengths 10.6 nm apart by using periodic-phase-shifting gratings fabricated by electron-beam lithography, ion implantation, and a two-step epitaxial growth [42]. Another group at the University of Illinois, Urbana, used two separate uniform gratings instead of periodically modulated gratings to realize dual-wavelength DBR lasers [43]. Using an $In_{0.29}Ga_{0.71}As$ quantum well active region, they demonstrated dual-wavelength laser operation with 16.9 nm wavelength separation, and in a later design, the group realized tunable wavelength separation by depositing separate metal contacts on the DBR sections and applying current to realize tuning of the DBR by thermal effects [44].

A few other approaches have been taken to engineer the resonant cavity of a semiconductor laser to support dual-wavelength laser modes. Common through the different works however are stability problems in supporting the two modes as most of the devices only demonstrate dual-wavelength output over certain temperature and current ranges. The wavelength separation is also limited as the lasers are still really single wavelength band devices relying on the same active region.

II. MULTI-WAVELENGTH LASER DIODE ARRAYS

To realize dual-wavelength laser diodes with larger spectral separations and stable outputs, most of the early research on dual-wavelength lasers relates to laser diode arrays rather than individual devices. These arrays consist of individual addressable laser diodes monolithically on the same chip, but while spatially close, they emit at different wavelengths. Many of the methods to realize such arrays involve special processing steps and/or epitaxial regrowth. In one creative approach, a group at Mitsubishi developed a dual-wavelength laser diode array by changing the internal optical losses of subsequent diodes in an array by varying the waveguide lateral width [45]. By processing a narrow waveguide laser next to a wide one and optimizing the cavity length, the laser thresholds of the two devices can be made such that laser emission from the wider device corresponds to the lowest quantized state transition ($n = 1$), while the narrower device corresponds to the second transition ($n = 2$). The group demonstrated dual-wavelength operation of the side-by-side monolithic devices at ~810 nm and ~830 nm while using the same active region material and quantum well width.

Sakai *et al.* at the Nagoya Institute of Technology in Japan, developed dual-wavelength laser diode arrays with outputs at ~1.2 μm and 1.3 μm with two similar designs [46], [47]. In the first design, an *n*-*i*-*p*-*i*-*n* structure is grown by epitaxy, where the first-grown intrinsic region is the smaller band gap 1.3 μm region, and the second is the 1.2 μm active region. A mesa is etched with the etch depth extending into the *p*-region, and separate contacts are then deposited on and

off the mesa. In this design each active region has separate *n*-contacts but shared a common *p*-contact, and with the proper bias, the two lasers reach threshold [46]. The authors note resistance problems due to the common *p*-region design and modify the design by growing instead an *n*-*i*-*n*-*i*-*n* structure [47]. The same etch is performed as before, but then zinc is diffused to form the proper *p*-regions. The active regions then have separate *p*-contacts and a common *n*-contact. The emission from the two devices is not very close as the spatial separation of the two laser spots are 50 μm and 80 μm respectively in the two designs.

Multiple groups have sought to extend the range of the wavelength separation of monolithic laser diode arrays by first etching and then doing selective-area epitaxial regrowth to form different compositional active regions with small spatial separation. A group at NTT in Japan used liquid phase epitaxy (LPE), regrowth to integrate 1.26 μm and 1.55 μm devices in a buried heterostructure design [48]. The near-field laser spot separation was 30 μm for their device. Bouadma *et al.* used liquid phase epitaxy regrowth to realize a laser diode array structure emitting at 850 nm and 885 nm with GaAs and $Al_{0.05}Ga_{0.95}As$ active regions respectively, and the spatial mode separation of their device was 25 μm [49]. Most of the early regrowth approaches used either metal organic chemical vapor deposition (MOCVD), or LPE due to the available *in situ* etching and growth inhibition on dielectric masks. A group at Bell Labs however developed close integration of GaAs and $In_{0.2}Ga_{0.8}As$ lasers with molecular beam epitaxy (MBE), regrowth [50]. In their devices, undercut of the etch mask, careful

cleaning, and the growth of a thick cladding buffer layer enabled devices with thresholds comparable to respective single-growth laser diodes.

Development of dual wavelength laser diodes was of interest to a group at Xerox in the 1990s. One of their first approaches involved epitaxial regrowth, however only the upper *p*-cladding region was regrown rather than an active region [51]. In the initial growth, two different quantum well active regions are grown over the entire wafer with the shorter-wavelength region grown first or closest to the substrate. Using a patterned etch, the longer-wavelength active region is then selectively removed where the shorter-wavelength laser will be processed. After the etching, a *p*-cladding region is regrown on top of all the devices. In the longer-wavelength devices, the carriers naturally populate the lowest band gap quantum well first and laser emission occurs at the longer wavelength. Then in the shorter-wavelength devices, the longer-wavelength active region no longer exists, so the emission is at the shorter wavelength. The spatial separation of the two monolithic laser diodes reported by the Xerox group is 15 – 20 μm.

In another creative approach developed by the same group, localized intermixing to raise the band gap of the lower active quantum well is used rather than etching to enable laser output at the shorter wavelength[52]. The barrier layers next to the lower band gap quantum well are doped with Si at 5×10^{18} cm^{-3}, and when annealed intermixing occurs. The authors note in intermixing a SiN_x surface layer is needed to prevent loss of As since an As-poor condition inhibits intermixing. Thus by patterning a SiN_x layer, the lower quantum well can

alternately either be intermixed or left intact, enabling a monolithic dual-wavelength laser diode array. Whereas the technique worked for infrared AlGaAs/GaAs dual-wavelength devices, the authors noted the high annealing temperature and long annealing time resulted in defect generation in phosphorous based compounds, and the technique could not be used for the fabrication of red/IR dual-wavelength devices. For dual-wavelength laser devices at these wavelengths, the Xerox group had to rely on selective etching and regrowth [53].

With the laser diode arrays, the laser modes of the two devices still have significant spatial separation that limits the overall coupling efficiency into an optical fiber. Osowski *et al.* used a *y*-junction coupler to combine the output of two monolithically integrated laser elements into a single waveguide for coupling into a fiber [54]. The group used a selective-area MOCVD process with a silicon dioxide mask to both inhibit and enhance the epitaxial growth rate. By varying the stripe width of openings in the oxide mask, the growth rate can be selectively controlled, and quantum wells of different thickness are grown on a single substrate. Their device then consists of two parallel active region channels with different transition wavelengths that then couple into the trunk of the *y*-junction coupler. With this configuration and the integration of electroabsorption modulators, the device can be operated with laser output at either one of the wavelengths or at both wavelengths simultaneously from the same spatial location. The device design is complex, and it requires three separate epitaxial growth steps with intermediate processing steps. The spectral separation of the

two laser modes is also limited since only the quantum well thicknesses and not the composition is varied.

III. ASYMMETRIC MULTIPLE QUANTUM WELL LASERS

Asymmetric multiple-quantum-well (AMQW), devices are of high interest for realizing dual-wavelength output from a single laser diode. In this design quantum wells of varying thickness and/or composition are located within a single active region within the core of a single optical waveguide, and the individual wells have different transition energies and associated wavelengths. Quantum wells of varying thickness are referred to as dimensionally asymmetric, and devices of varying composition are compositionally asymmetric [55].

In AMQW devices it is critical that the carrier dynamics are altered by unique heterostructure designs when compared to the design of a conventional multiple-quantum-well laser (MQW). In conventional lasers, the barrier heights and thicknesses between the wells are usually optimized to obtain the lowest possible threshold current [24]. The timescale of carrier transport between the wells is much shorter than the energy relaxation processes which results in quasi thermal equilibration of the carriers between the wells. The quasi-Fermi levels are then approximately flat and constant across the different wells and single Fermi distributions exist for electrons and holes throughout the junction active region. Carriers then populate the lowest energy states first as described earlier, and the MQW gain medium is considered a homogeneously broadened gain medium,

from which it is difficult to sustain stable laser output at two wavelengths simultaneously.

Disruption of the carrier transport and quasi thermal equilibration between the asymmetric wells is achieved by employing high and/or thick barriers between the wells. This leads to separate quasi-Fermi levels or Fermi distributions of carriers for each individual well and enables a degree of control over the carrier densities in the individual asymmetric wells and more equal emission and gain from the different wells. Broader gain spectrums can then be achieved in AMQW devices, and they are of high interest for broad wavelength tuning of external cavity semiconductor lasers and for broad-band superluminescent diodes [56]. Due to the disruption of carrier quasi thermal equilibration, the gain medium of an AMQW device approaches inhomogeneous broadening, and dual-wavelength laser emission is possible in contrast to conventional homogeneously broadened quantum well laser diodes.

Sotomitsu Ikeda and Akira Shimizu in Japan were the first to report dual-wavelength laser emission from an AMQW device and provided some of the first theory and modeling of the unique behavior of these devices [57], [58]. In their work, Ikeda and Shimizu use two compositionally and dimensionally asymmetric quantum wells with the barrier between them larger and thicker than in conventional MQW structures. The larger shorter-wavelength well is located nearest the *p*-doped region of the *p*-*i*-*n* junction, and the width of the well is wider than the mean-free path of the energy relaxation processes of holes. Injected holes from the *p*-region are then captured in the shorter-wavelength well and must be

thermally activated to transfer over the barrier and into the longer-wavelength well. By making the barrier high and/or thick, Ikeda and Shimizu suggest the rate of hole transport from the shorter- to the longer-wavelength well can be slowed to the same order as the overall recombination rate, disrupting the quasi thermal equilibration. In their theory they assume an adequate supply of electrons is injected into both wells with injection into the shorter-wavelength well near the p-side of the junction achieved by a combination of: 1) making the conduction band edge of the separate confinement layer on the *n*-side higher than the edge of the barrier layer; 2) making the longer-wavelength well narrower than the mean-free path of the energy relaxation processes of electrons; and 3) doping the barrier layer n^+. The transport of holes over the barrier is then the determining factor in the final behavior of the AMQW laser [58].

Experimentally, Ikeda and Shimizu reported dual-wavelength laser emission from an AMQW device with an 8 nm GaAs quantum well and a shorter-wavelength $Al_{0.08}Ga_{0.92}As$ well that is 16 nm wide. The barrier between the wells is a 15 nm $Al_{0.3}Ga_{0.7}As$ barrier [57]. For devices with cavity lengths greater than 300 μm, simultaneous dual-wavelength laser output was observed at 831 nm and 818 nm with the longer wavelength reaching threshold first. In their devices, the barrier height is not too high so that sufficient carriers are still injected into the longer-wavelength well and it reaches threshold first. However, since the two asymmetric wells have separate quasi-Fermi distributions, the carrier density and gain in the shorter-wavelength well keep increasing with continued increase in the

applied current. Eventually threshold is reached at the shorter wavelength, and simultaneous laser output from the two quantum wells is observed.

To date, dual-wavelength laser output from AMQW laser diodes has been limited only to certain ranges of current and cavity lengths [57], [59]. Experimentally in AMQW lasers, as the current to the device is increased above the thresholds of both laser wavelengths, the output power of the longer-wavelength laser starts to decrease while the output power of the shorter wavelength continues to increase. Eventually, the longer wavelength ceases lasing entirely and a complete switch of the laser output from the longer wavelength to the shorter wavelength is observed.

One explanation for the wavelength switching in AMQW lasers suggested by Wang *et al.* is changing threshold conditions with increasing current lead to the output reduction and eventual cessation of the longer-wavelength laser [59]. By measuring the electroluminescence from the bottom side of devices, they monitored the spontaneous emission from the active regions as a function of current and noticed increases in the spontaneous emission spectra of both regions even beyond the laser thresholds, indicating incomplete pinning of the carrier concentrations. Despite the reduction in the longer-wavelength laser output, the spectrum from both laser active regions continues increasing as the current is increased. This suggests the gain is not reduced but rather continues to increase for both active regions. Wang *et al.* therefore suggest the laser threshold conditions are not constant but continue to increase due to thermal effects and increased internal optical loss. Operating an AMQW laser diode continuous-

wave, the measured thresholds were approximately 80 mA, 150 mA, and 180 mA for the longer wavelength, shorter wavelength, and cessation of the longer wavelength respectively, but under pulsed operation, the same thresholds were 70 mA, 260 mA, and 330 mA [59]. If the threshold conditions are increasing due to thermal effects in the continuous-wave scenario, the carrier concentrations, spontaneous emission, and gain will continue to increase rather than pin. The authors note the increase in gain is larger at the shorter wavelength than the longer wavelength with further injection, and eventually only the shorter-wavelength gain is able to match the increasing threshold requirements. In comparison, under pulsed-operation the threshold conditions do not change as rapidly due to fewer thermal effects and the laser switching phenomenon instead occurs at higher currents.

These experimental results indicate the dual-wavelength output is sensitive to the internal losses and dependent on the gain spectrum at threshold. The cavity length and mirror loss are then variables in enabling dual-wavelength laser output. Multiple groups have observed that for short-cavity-length AMQW lasers, laser output occurs only at the shorter wavelength and never at the longer wavelengths [57], [60]. This is due to the higher loss which prevents laser output from the longer-wavelength quantum well. With continued injection and band filling, the modal gain eventually becomes large enough at the shorter wavelength, and only the shorter-wavelength laser reaches threshold. For long-cavity-length AMQW lasers, threshold is reached with a much smaller material gain due to the lower loss, and only laser output from the longer-wavelength laser is observed.

Therefore to realize dual-wavelength laser emission from an AMQW device, the gain spectrum near the thresholds needs to be broad and flat with nearly equal gain at both the shorter and longer wavelengths [60]. From band filling such a gain spectrum is realized only near a specific cavity length dependent on the other losses, and Hamp and Cassidy define this cavity length as the transition cavity length (TCL), [55]. The other modulator is the mirror loss, and for higher output power from an AMQW device, Jiang *et al.* showed that facet coatings can be used to increase the TCL and still ensure the needed level of loss and threshold conditions [60].

IV. OPTICALLY-PUMPED DUAL-WAVELENGTH LASERS

In the previous section it was noted AMQW lasers can demonstrate dual-wavelength laser output; however, the two-color output is only observed for certain ranges of current and is dependent on the internal losses, mirror loss, and cavity length. Also in the AMQW laser diode designs, carrier injection of both the longer- and shorter-wavelength quantum wells is achieved directly through the *p-i-n* junction and the applied current. The novel internal-optically-pumped dual-wavelength laser diode design proposed here is unique wherein the asymmetric wells and barrier are designed so current injection into the longer-wavelength quantum well is blocked entirely and an innovative internal optical pumping scheme generates carriers within the longer-wavelength quantum well. Dual-wavelength laser output using this unique approach should not be constrained to a narrow range of total loss, cavity length, or applied current.

The shorter-wavelength active region, labeled the master active region, is placed within the *p-n* junction of the diode and carriers are injected with applied current as in typical laser diodes. Then the longer-wavelength active region, termed the slave active region, is placed outside of the junction but still within the guided optical field of the cavity waveguide as illustrated in Fig. 2.1. Contrary to previous AMQW devices, by positioning longer-wavelength slave quantum well outside the junction, very few minority carriers are generated in the slave quantum well directly due to the applied current. Instead as current is applied to the device, the shorter-wavelength master laser should reach threshold first in the novel dual-wavelength laser design, again contrary to previous AMQW devices. This master laser then internally optically pumps the longer-wavelength slave quantum well until it reaches threshold as well and simultaneous dual-wavelength laser output is achieved. The asymmetric wells in the previous AMQW devices are considered as a single active region within the junction. However, in the novel internal-optically-pumped design, the asymmetric master and slave quantum wells are considered separate active regions due to the unconventional placement of the slave active region outside the junction and the two different methods of carrier injection.

The unique approach of using the internal optical field of the shorter-wavelength master laser to optically pump the second slave laser, in theory should enable continued dual-wavelength laser output with continued current injection far beyond the thresholds of both lasers contrary to the previous AMQW dual-wavelength lasers. Continued increase in the output powers of both lasers can be

realized since continued injection of the master laser will also result in stronger optical pumping of the slave laser. With the internal optical pumping scheme, dual-wavelength functionality should therefore not be limited to a narrow range of cavity lengths or threshold conditions. One other difference compared to the previous AMQW devices is much larger spectral difference in the wavelengths of the two lasers can be achieved due to the nature of the optical pumping.

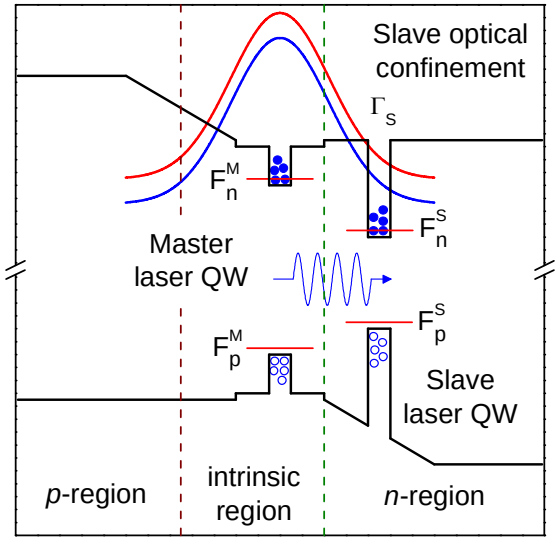

Novel internal-optically-pumped DWLD band diagram

Fig. 2.1. Diagram illustrating the design and optical pumping of the novel internal-optically-pumped dual-wavelength laser diode.

The internal optical pumping scheme arises from a similar idea developed in vertical cavity surface-emitting lasers (VCSEL), although not explored for in-plane laser diodes. In 1998, Jayaraman *et al.* reported a device consisting of an 850 nm VCSEL vertically wafer-fused to a 1300 nm VCSEL [61]. A conventional *p-i-n* junction provides carrier injection for the 850 nm VCSEL, and the mirrors

and active region of the 1300 nm VCSEL are undoped. The 850 nm VCSEL is then used to optically pump the 1300 nm VCSEL. The design overcame many of the technical challenges of VCSELs at that wavelength, and in their paper Jayaraman *et al.* claimed these VCSELs to be the first 1300 nm VCSELs to meet the required performance for commercial telecommunication.

Carlin *et al.* refer to this cascaded optical pumping scheme in VCSELs as "hybrid electrical optical pumping," and they reported dual wavelength laser output at 927 nm and 955 nm from two vertically stacked InGaAs VCSELs [62]. They address issues related to mode competition and coupling of the two cavities that arise when the wavelength separation of the two VCSELs is much closer than the 850 nm and 1300 nm reported by Jayaraman *et al.* [61]. Whereas the dual-wavelength laser beams of the VCSELs from these two research groups are coaxial, the two different active regions are within separate cavities, and the cascaded dual-cavity VCSELs are referred to as BiVCSELs in the literature [62], [63]. To the best of our knowledge, no one has studied the case where the two active regions are within the same cavity or where the optical pumping scheme is incorporated in an in-plane laser structure as it is proposed here with the novel dual-wavelength laser diode design.

The design of the novel dual-wavelength laser diode design is also similar in some aspects to the optically-pumped dual-wavelength lasers studied by Ron Kaspi's group [64]-[66]. The main difference of the two different device designs is whereas the novel design uses the hybrid approach of electrical injection and internal optical pumping, the devices of Kaspi's group use only optical pumping

from an external source to generate carriers in two separate active regions within a single waveguide. The wavelength range of the devices is in the midinfrared using type-II InGaSb/InAs quantum well active regions, and the two different active regions with different target wavelengths are placed within the same waveguide core comprised of GaSb. An AlGaAsSb barrier layer that is transparent to the optical pumping source is used to separate the two active regions and partition the waveguide. This barrier layer prevents scattering and redistribution of the carriers from the shorter-wavelength active region to the longer-wavelength region. With this design and at liquid nitrogen temperatures, they observed laser output as far apart as ~4.0 μm and ~5.4 μm. To demonstrate the importance of the barrier layer, they grew the same structure without the barrier layer, which when tested produced laser output only near ~4.1 μm since the carriers were able to scatter and redistribute to the lower energy quantum wells.

One interesting aspect Kaspi's group noticed was the impact of the modal overlap of the shorter-wavelength mode with longer-wavelength active region [66]. They noticed the relative intensity of the two lasers depends on the modal overlap of the shorter-wavelength waveguide mode with the longer-wavelength active region. The group carefully designed a set of samples so the absorption layers and carrier generation were equal across the set, and the modal overlap was varied by increasing the thickness of the transparent barrier layer between the two active regions. From the measurements, they noticed when the overlap is large, lasing only occurs at the longer wavelength, but as the overlap is reduced, laser

output is observed from both wavelengths with the larger intensity at the longer wavelength. At even lower modal overlap, they observed a switch in the relative intensities with the shorter-wavelength laser producing the higher output. Kaspi's group cites re-absorption of the shorter-wavelength photons in the longer-wavelength active region as an additional modal loss that influences the threshold and intensity of the shorter-wavelength laser.

The critical design elements are the same for the novel dual-wavelength laser diode and the optically-pumped midinfrared devices by Kaspi's group. First a barrier or means of disrupting scattering and quasi thermal equilibration of carriers from the shorter-wavelength active region to the longer-wavelength region is necessary. Second, the modal overlap of the absorbing longer-wavelength active region requires careful consideration in the design process. In the next chapter, a model is developed of the internal optical pumping scheme of the novel dual-wavelength laser diode, and the impact of the modal overlap or optical confinement is investigated.

3 Internal Optical Pumping Theory

To better understand the internal optical pumping of the slave active region by the master laser in the novel dual-wavelength laser diode design, a model is developed starting from the standard rate equations for conventional laser diodes. The equations are modified to include absorption of the slave region and pumping by the master laser, and logarithmic gain-current density relations for the quantum well (QW), active regions are included to model the material gain. Complete inhibition of quasi thermal equilibration and decoupling of the quasi-Fermi levels between the two active regions are assumed. To study the internal optical pumping, it is also assumed that zero carriers are injected from the junction into the slave region so the slave region relies completely on the internal optical pumping for carrier generation. In the next chapter it will be shown these are valid assumptions for the studied designs. From the modeling in this chapter, the influence of the optical confinement of the slave active region on the laser thresholds and the device performance is illustrated.

I. RATE EQUATIONS, PHOTON DENSITY, AND LASER THRESHOLD

From the continuity equations, the rate equation for the carrier concentration inside the active region of a laser diode is

$$\frac{\partial n}{\partial t} = D\nabla^2 n + \eta_i \frac{J}{qd} - R(n) - R_{st}S \,. \tag{3.1}$$

The first term on the right-hand side accounts for carrier diffusion which occurs mainly in the lateral direction in double-heterostructure devices due to the

confinement in the transverse or growth direction provided by the heterostructure barriers. For index-guided structures such as ridge lasers, the lateral carrier diffusion effect is also often assumed to be negligible [67], and it assumed such herein. The second term in (3.1) is the injection of carriers due to the applied current and the *p-n* junction into the active region of thickness d where η_i is the injection efficiency. The third term $R(n)$ accounts for both nonradiative and spontaneous radiative recombination

$$R(n) = An + Bn^2 + Cn^3 \tag{3.2}$$

where *A*, *B*, and *C* are the respective coefficients of Shockley-Read-Hall (SRH), spontaneous, and Auger recombination. The final term in (3.1) accounts for carrier recombination due to stimulated emission where S is the photon density of the laser mode, and the stimulated emission coefficient is

$$R_{st} = v_g g(n) = \frac{c}{n_g} g(n) \tag{3.3}$$

where v_g and n_g are the group velocity and group refractive index and $g(n)$ is the local or material gain. At steady-state and assuming zero diffusion, the rate equation simplifies to

$$\eta_i \frac{J}{qd} = An + Bn^2 + Cn^3 + v_g g(n) S \,. \tag{3.4}$$

In semiconductor quantum well lasers, only a small fraction of the guided optical field, defined as the confinement factor, overlaps the quantum well active region. The confinement factor Γ is written as

$$\Gamma = \frac{\int_{-d/2}^{d/2} |u(x,y)|^2 \, dxdy}{\int_{-\infty}^{\infty} |u(x,y)|^2 \, dxdy} \tag{3.5}$$

where $u(x,y)$ is the optical field. The normalized magnitude square of the optical field serves as a probability density for photons inside the cavity, and the photon density inside the active region is then

$$S = \frac{\Gamma \cdot (\text{total \# of photons})}{V_a} \tag{3.6}$$

where V_a is the volume of the active region. Rearranging the terms leads to

$$S \cdot \frac{V_a}{\Gamma} = S \cdot V_c = \text{total \# of photons}. \tag{3.7}$$

where V_c is an effective cavity volume

$$V_c = \frac{V_a}{\Gamma}. \tag{3.8}$$

The photon density S of the active region is then the photon density throughout the effective cavity volume.

Equation (3.4) is the rate equation at steady-state for carriers in the active region of a laser diode, assuming negligible diffusion. The rate equation for the photon density S of a laser mode is

$$\frac{dS}{dt} = \left(\Gamma v_g g(n) - \frac{1}{\tau_{ph}} \right) S + \beta R_{sp} \tag{3.9}$$

where the first term on the right-hand side accounts for the gain or generation of photons in a mode due to stimulated emission, and the second term is the loss of photons represented by a photon lifetime. The photon lifetime

$$\tau_{ph} = \frac{1}{v_g(\alpha_m + \alpha_i)} \tag{3.10}$$

depends on the mirror loss

$$\alpha_m = \frac{1}{2L}\ln\left(\frac{1}{R_1 R_2}\right) \tag{3.11}$$

representing the transmission of photons at the facets with reflectivities R_1 and R_2, and cavity length L. The intrinsic loss α_i includes losses due to reabsorption of photons (bulk and free-carrier) and scattering of photons out of the cavity. The final term in (3.9) accounts for photons from spontaneous emission where β is the fraction of the total spontaneous emission which couples into the mode. This is negligible compared to the generation of photons due to stimulated emission and is generally ignored at threshold.

To sustain a laser mode, the modal gain must equal the total loss of one round-trip through the resonator cavity. From (3.9)-(3.11) the threshold gain of a laser diode is then

$$\Gamma g_{th} = \alpha_m + \alpha_i = \frac{1}{2L}\ln\left(\frac{1}{R_1 R_2}\right) + \alpha_i . \tag{3.12}$$

Since the recombination rate of stimulated emission is significantly greater than the other recombination mechanisms, the carrier concentration in the active region pins at its threshold level n_{th}, and the material gain and quasi-Fermi levels which are both dependent on the carrier concentration also pin. With a negligible photon density below threshold, the threshold current density is then

$$\eta_i \frac{J_{th}}{qd} = An_{th} + Bn_{th}^2 + Cn_{th}^3 \tag{3.13}$$

and above threshold the rate equation is

$$\eta_i \frac{J}{qd} = An_{th} + Bn_{th}^2 + Cn_{th}^3 + v_g g_{th} S \tag{3.14}$$

due to pinning of the carrier concentration at threshold. Subtracting (3.13) from (3.14) and rearranging terms, the photon density of the laser mode above threshold is then

$$S = \frac{\eta_i}{qdv_g g_{th}} (J - J_{th}) . \tag{3.15}$$

Different methods for calculating the material gain spectrum exist, and these models range in complexity based on the different phenomenon included [67], [68]. Whereas the models become increasingly accurate as strain, valence-band intermixing, quantum effects, wave-function overlap, and broadening effects are considered, the complexity of these models also increases, and the closest match between calculated and real gain spectrums is only realized when many-body effects are considered. The laser mode of a laser diode corresponds to the cavity mode that closest overlaps the peak of the gain spectrum and knowledge of the peak gain is sufficient and simplifies the modeling if spectral properties are not needed. For modeling the internal-optically-pumped dual-wavelength laser diode, a simple logarithmic gain-current density relation can be used.

For bulk double-heterostructure lasers, the peak gain versus current density is considered a linear relationship. However, McIlroy *et al.* suggested a logarithmic peak gain-current density relation is more appropriate for quantum

well lasers based on their simulations of GaAs quantum wells [69]. In one form the peak gain g is

$$g = g_0\left(\ln\left(\frac{\eta_i J}{J_0}\right)+1\right) \tag{3.16}$$

where g_0 and J_0 are the gain and current density at the point on the curve where the ratio g/J is maximum. Whereas another form of the logarithmic fit is

$$g = g_0 \ln\left(\frac{\eta_i J}{J_{tr}}\right) \tag{3.17}$$

where the current density is normalized by the transparency current density [70]. The current normalization factors of the current in the two forms are related by

$$J_0 = J_{tr} \cdot e \tag{3.18}$$

and the gain coefficient g_0 is the same for both equations.

II. INTERNAL OPTICAL PUMPING THEORY

In building a model of the internal-optically-pumped dual-wavelength laser diode, the analytical equations reviewed in the previous section are modified for the master and slave laser active regions with super(sub)scripts M and S added to many of the parameters. To describe the internal optical pumping, a critical relationship is derived in the following analysis with a few general assumptions. The mirror and intrinsic losses of both the master and slave lasers are assumed to be nearly equal in the analysis. Also the master and slave regions are both considered as single quantum wells initially for simplicity, and in a later

section the model is adjusted to account for multiple quantum wells in the master active region.

For the master laser active region, the photon rate equation is adjusted to include an additional absorption loss by the slave region α_S where Γ_S is the confinement of the slave region determined by the overlap of the master laser optical mode.

$$\frac{dS_M}{dt} = \left(\Gamma_M v_g g_M(n_M) - \frac{1}{\tau_{ph}} - \Gamma_S v_g \alpha_S \right) S_M + \beta R_{sp}^M \tag{3.19}$$

The master laser threshold gain is then

$$\Gamma_M g_{th}^M = \alpha_m + \alpha_i + \Gamma_S \alpha_S \tag{3.20}$$

and from the logarithmic gain-current density relation, the threshold current density is

$$J_{th}^M = \frac{J_{tr}^M}{\eta_i^M} e^{g_{th}^M / g_0^M} = \frac{J_{tr}^M}{\eta_i^M} \exp\left(\frac{\alpha_m + \alpha_i + \Gamma_S \alpha_S}{\Gamma_M g_0^M} \right). \tag{3.21}$$

The photon density of the master laser mode is then

$$S_M = \frac{\eta_i^M}{q d_M v_g g_{th}^M} (J_M - J_{th}^M). \tag{3.22}$$

To model the internal optical pumping of the slave by the guided optical field of the master laser, the carrier generation rate inside the slave region due to the photon density of the master laser is derived. Starting from the photon rate equation of the master laser (3.19), the change in the photon density due to absorption by the slave region is

$$\frac{dS_M}{dt} = -\Gamma_S v_g \alpha_S S_M \qquad [\mathrm{cm}^{-3} \cdot \mathrm{s}^{-1}] \tag{3.23}$$

and the rate of total number of photons lost is then

$$V_c^M \left(\frac{dS_M}{dt} = -\Gamma_S v_g \alpha_S S_M \right) \qquad [\mathrm{s}^{-1}] \tag{3.24}$$

where V_c^M is the cavity volume of the master laser mode. By particle conservation, this rate of photon loss must equal the rate of the total number of carriers generated in the slave region, which is then divided by the actual volume of the slave region to get the generation rate per unit volume in the slave region

$$G_S = \frac{V_c^M}{V_S} \Gamma_S v_g \alpha_S S_M \,. \qquad [\mathrm{cm}^{-3} \cdot \mathrm{s}^{-1}] \tag{3.25}$$

From the definition for the cavity volume

$$V_c^M = \frac{V_M}{\Gamma_M} \tag{3.26}$$

and assuming the width and cavity length of the master and slave regions are equal, the generation rate becomes

$$G_S = \frac{V_M}{V_S} \frac{\Gamma_S}{\Gamma_M} v_g \alpha_S S_M = \frac{d_M}{d_S} \frac{\Gamma_S}{\Gamma_M} v_g \alpha_S S_M \,. \tag{3.27}$$

This is the carrier generation rate due to internal optical pumping by the master laser rather than electrical injection of carriers into the slave laser active region. From this generation rate an effective internal-optical-pumping current density is defined

$$\frac{J_S^{opt}}{q d_S} = G_S \tag{3.28}$$

which then allows use of the logarithmic gain-current density relation to predict the gain of the slave. Substituting (3.27), this optical-pumping current density becomes

$$J_S^{opt} = \frac{\Gamma_S}{\Gamma_M} q d_M v_g \alpha_S S_M \tag{3.29}$$

For the slave laser, a separate photon rate equation and threshold gain condition exist and are identical to a conventional laser diode.

$$\frac{dS_S}{dt} = \left(\Gamma_S^{\lambda_S} v_g g_S(n_S) - \frac{1}{\tau_{ph}} \right) S_S + \beta R_{sp}^S \tag{3.30}$$

$$\Gamma_S^{\lambda_S} g_{th}^S = \alpha_m + \alpha_i \tag{3.31}$$

Since the wavelengths and thus optical modes and confinement factors of the master and slave lasers differ slightly, $\Gamma_S^{\lambda_S}$ is used here to distinguish the confinement factor for the modal gain of the slave laser from Γ_S the confinement for the modal absorption loss to the master laser. In the analysis in this chapter they will be considered as equal, but in predicting the performance of actual designs in later chapters they will be treated not equal. From the threshold gain, an optical-pumping current density threshold and carrier generation rate threshold are found using the logarithmic gain-current density relation

$$J_{S,th}^{opt} = J_{tr}^S e^{g_{th}^S / g_0^S} = J_{tr}^S \exp\left(\frac{\alpha_m + \alpha_i}{\Gamma_S^{\lambda_S} g_0^S} \right) \tag{3.32}$$

$$G_S^{th} = \frac{J_{tr}^S}{q d_s} \exp\left(\frac{\alpha_m + \alpha_i}{\Gamma_S^{\lambda_S} g_0^S} \right) \tag{3.33}$$

and from the threshold carrier generation rate, a threshold photon density of the master laser mode is found using the relationship in (3.27)

$$S_M^{th-S} = G_S^{th} \frac{d_S}{d_M} \frac{\Gamma_M}{\Gamma_S} \frac{1}{v_g \alpha_S}. \tag{3.34}$$

This is the photon density of the master laser needed to optically pump the slave region and generate enough carriers to reach its laser threshold. From this photon density and from (3.22), a second threshold current is found

$$J_{th}^S = S_M^{th-S} \cdot \frac{q d_M v_g g_{th}^M}{\eta_i^M} + J_{th}^M \tag{3.35}$$

that is the applied current necessary for the master laser to produce the photon density required to optically pump the slave region to its threshold and realize laser output at the master and slave wavelengths simultaneously. Combing (3.20) and (3.33)-(3.35) this threshold of the slave laser becomes the sum of two exponential terms

$$J_{th}^S = \frac{(\alpha_m + \alpha_i + \Gamma_S \alpha_S)}{\Gamma_S \alpha_S \eta_i^M} \cdot J_{tr}^S \exp\left(\frac{\alpha_m + \alpha_i}{\Gamma_S^{\lambda_S} g_0^S}\right) + \frac{J_{tr}^M}{\eta_i^M} \exp\left(\frac{\alpha_m + \alpha_i + \Gamma_S \alpha_S}{\Gamma_M g_0^M}\right) \tag{3.36}$$

where the second exponential increases with the optical confinement of the slave active region. This second term is the threshold current of the master laser, and as expected the modal absorption loss and threshold increase with greater overlap of the optical mode with the slave region. In the first term on the right-hand side of (3.36), the exponential term decreases with greater optical confinement of the slave region, representing a reduction in material gain of the slave laser region

and optical pumping by the master laser needed to reach threshold. Additionally an inverse relation of the optical confinement factor of the slave region reduces this term even further. From these increasing and decreasing terms with slave optical confinement, an optimum optical confinement factor then exists at which the slave laser threshold is minimized.

III. RESULTS OF INTERNAL OPTICAL PUMPING MODEL

In the initial modeling, a simple implementation of the previous equations is made to better understand the device physics and identify the critical design considerations of the novel internal-optically-pumped dual-wavelength laser. The calculations are done using self-generated code in MATLAB, and assumptions about the active material and cavity losses are discussed next. For the remainder of this chapter, the reasonable assumption is made that the optical confinement factor of the slave for both the master and slave laser modes are equal.

For the logarithmic gain-current density relation, gain parameters are chosen from the literature that best match the quantum well widths and materials of the actual samples to be grown. The master laser active region consists of multiple 10 nm wide GaAs quantum wells, and the slave laser active region is a single 10 nm wide $In_{0.24}Ga_{0.76}As$ quantum well slave region. The closest matching gain-current density data found were for a 10 nm GaAs quantum well and a 7 nm $In_{0.25}Ga_{0.75}As$ quantum well, and the gain coefficients and transparency current densities are listed in Table III.I [70].

TABLE III.I
LOGARITHMIC GAIN-CURRENT DENSITY PARAMETERS

Composition	QW width – d (nm)	Gain coeff. – g_0 (cm^{-1})	Transp. Current density – J_{tr} (A/cm^2)
GaAs[a]	10	1200	90
$In_{0.25}Ga_{0.75}As$[b]	7	1396	48

[a] values from [70], [71]
[b] values from [70], [72]

For the master region GaAs quantum wells, the composition and well width are exactly the same as those in the sample to be grown. However for the slave region, the In composition in the published data is 25% instead of 24%, and the well width is 7 nm instead of 10 nm. Since the difference in composition is small, the difference in key parameters such as effective mass, matrix element, and index of refraction should be minimal, and it is reasonable to expect only a small difference in the gain coefficient g_0. The small variation in the width of the quantum wells results in changes to the quantized energy levels and corresponding shifts in the gain spectrum and laser wavelength. It also results in a smaller density of states (per unit volume) for the wider well and a smaller transparency carrier concentration. In terms of current density however, the smaller concentration is partially compensated by the larger volume, and therefore the change in transparency current density between the two wells is minimal. Coldren and Corzine showed for $In_{0.20}Ga_{0.80}As$/GaAs quantum wells with widths between 5-10 nm, there is little change in the transparency current density of the quantum well [68]. The values in Table III.I are thus considered sufficient for

modeling the gain of the GaAs quantum wells in the master laser active region and the gain of the 10 nm wide $In_{0.24}Ga_{0.76}As$ quantum well of the slave laser active region. Initially, both the master and slave active regions are assumed to be single quantum wells, and in the next section the model will be adjusted to account for multiple quantum wells within the master active region.

The threshold gains of the master and slave lasers are determined by summing the different losses listed in Table III.II. The mirror and intrinsic losses are assumed the same for both the master and slave laser active regions. The mirror loss is calculated for a cavity length of 1000 μm with facet reflectivities of 30%. For the intrinsic loss, a moderate value of 10 cm^{-1} is chosen which includes free-carrier absorption. In determining the absorption of the slave material at the master laser wavelength, the bulk absorption is chosen. Using the bulk rather than a quantum well absorption is justified since the barriers of the $In_{0.24}Ga_{0.76}As$ quantum well are GaAs as required by the growth and the pumping energy of master laser is slightly larger than the GaAs barrier band gap. At this point for generality, absorption in the GaAs barrier layer is neglected; however, it will be considered later. The absorption coefficient is then determined from published $n-\kappa$ tables using

$$\alpha_S(\lambda_M) = \frac{4\pi}{\lambda_M}\kappa(\lambda_M). \tag{3.37}$$

The material or local absorption of the slave quantum well is 24,768 cm^{-1} which leads to a modal loss of 247.7 cm^{-1} if the confinement factor is only 1%. Since its

active region is the lowest band gap in the structure, the slave laser has no other inter-band absorption losses to consider.

TABLE III.II
ASSUMED MODAL LOSSES OF MASTER AND SLAVE LASERS

Laser	Mirror loss – α_m (cm^{-1})	Intrinsic loss – α_i (cm^{-1})	Slave abs. – $\Gamma_S \alpha_S$ (cm^{-1})
Master	12.04[a]	10	247.7[b]
Slave	12.04[a]	10	-

[a] $L = 1000$ μm, $R_1 = R_2 = 0.3$
[b] $\Gamma_S = 1\%$

From these assumptions for the material gain and cavity losses, the modal gain of the slave active region as a function of the applied current is calculated for different optical confinements of the slave, and the results are plotted in Fig. 3.1. Increasing the optical confinement of the slave results in higher modal gains for the slave as expected, but the applied current density at which the slave region reaches transparency also increases due to the greater modal absorption loss to the master region and the resulting increase in the threshold current density of the master laser. In Fig. 3.1 the slave laser threshold is not achieved at a reasonable current for an optical confinement factor of 0.2%. The threshold is reduced when the factor is increased to 0.4% and 0.6% due to the increased modal gain; however, the threshold is lowest for the factor of 0.4% since the transparency current density is lower.

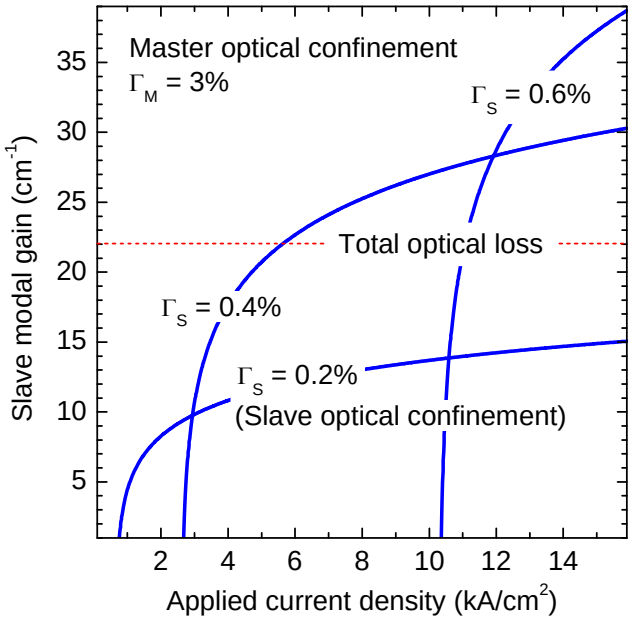

Fig. 3.1. Modal gain of the slave laser versus applied terminal current for different slave optical confinement factors.

To better visualize the impact of the slave optical confinement factor, the two terms of the slave laser threshold in (3.36) are calculated versus the optical confinement factor of the slave in Fig. 3.2. The threshold of the master laser or the second term in (3.36) is plotted for different master optical confinements, and the exponential increase in the threshold with increased slave optical confinement is seen. The first term or the optical pumping term in (3.36) is labeled ζ and is the decaying curve in Fig. 3.2. The optical pumping term ζ is independent of the optical confinement or modal gain of the master, and graphically the threshold of the slave is then the sum of the decaying curve and one of the master laser threshold curves. The threshold current density of the slave laser is calculated and shown versus the slave optical confinement in Fig. 3.3 for the same master optical confinements used in Fig. 3.2.

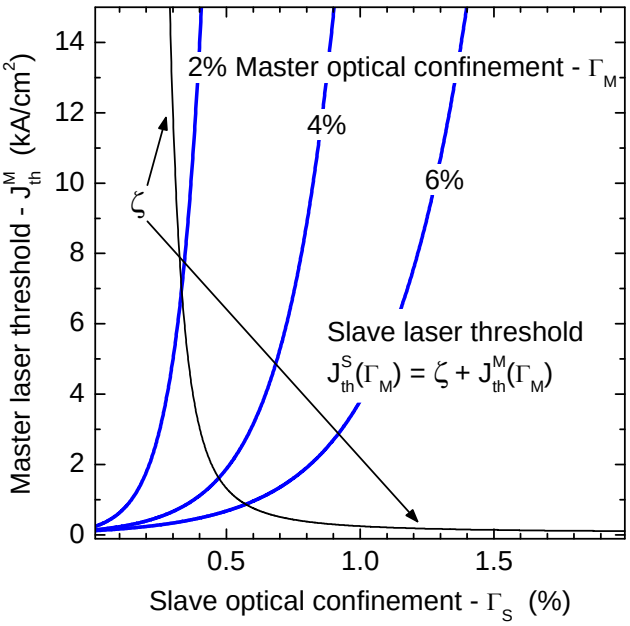

Fig. 3.2. Calculated threshold current densities of a single GaAs QW master laser versus optical confinement of the slave active region.

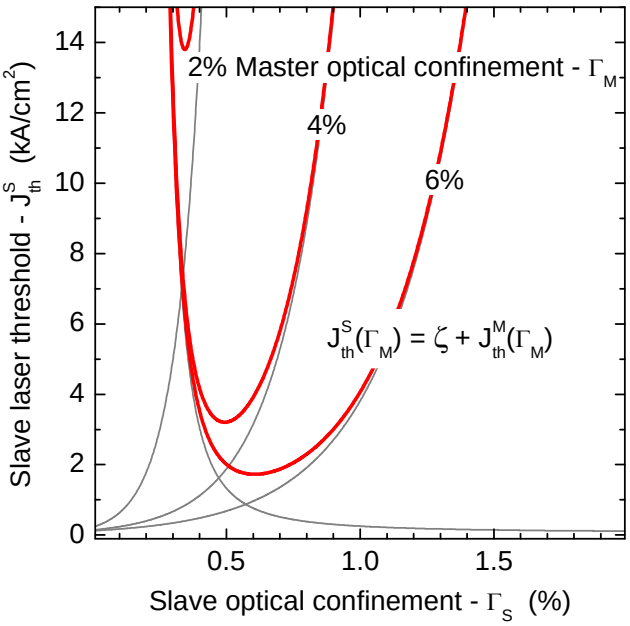

Fig. 3.3. Calculated threshold current densities of the slave laser versus optical confinement of the slave laser.

At zero optical confinement of the slave laser active region in Fig. 3.3, the threshold current densities of the master laser are 123 A/cm^2 and 226 A/cm^2 for 6% and 2% master optical confinement respectively and are reasonable thresholds for conventional GaAs quantum well lasers. This is expected since it is assumed there is no current injection into the slave region. As noted, at small optical confinements the threshold of the slave laser is very large due to the small modal gain. Increasing the slave confinement factor reduces the threshold of the slave laser; however, the resulting increase in modal absorption loss to the master laser leads to greater thresholds for the master laser and thus eventually the slave laser as well. The slaver laser thresholds are thus minimized at the optimum slave optical confinements in Fig. 3.3. This minimum slave laser threshold and the corresponding optimum optical slave confinement factor must be found numerically since differentiating (3.36) to find an analytical expression results in needing to solve a transcendental equation. The optimum optical slave confinements and the thresholds of the master and slave lasers at this confinement from the modeling are listed in Table III.III.

TABLE III.III
OPTIMUM OPTICAL CONFINEMENT AND THRESHOLDS WITH SINGLE QUANTUM WELL MASTER LASER ACTIVE REGION

Master laser optical confinement (%)	Minimum slave laser threshold (A/cm^2)	Optimum slave laser optical confinement (%)	Master laser threshold at optimum slave confinement (A/cm^2)
2	13,796	0.35	7931
3	5473	0.43	3112
4	3207	0.49	1823
5	2242	0.55	1274
6	1728	0.61	979.5

Increasing the optical confinement factor of the master laser active region leads to reduced thresholds of the novel internal-optically-pumped dual-wavelength laser diodes due to the increased modal gain of the master active region. The larger modal gain results in lower material gain required for threshold, and from the logarithmic gain-current relation, small reductions in the material gain can result in large reductions in the threshold current. An interesting trend is seen in the data in Table III.III where the optimum optical confinement of the slave laser increases with increased optical confinement of the master laser. The modal absorption loss is then larger for the master laser, but the thresholds of both the master and slave lasers at the optimum slave confinement are still lowered. Both thresholds are lowered since the increase in the modal gain of the slave laser is less than the increase in modal absorption loss to the master. This is seen in Fig. 3.4 where the optimum slave optical confinement is calculated versus

the optical confinement factor of the master and the increase in optimum slave confinement is sub-linear. The threshold currents of the novel internal-optically-pumped laser diodes can thus be reduced by: 1) optimizing the optical confinement factor of the slave laser active region and 2) increasing the optical confinement and modal gain of the master laser active region.

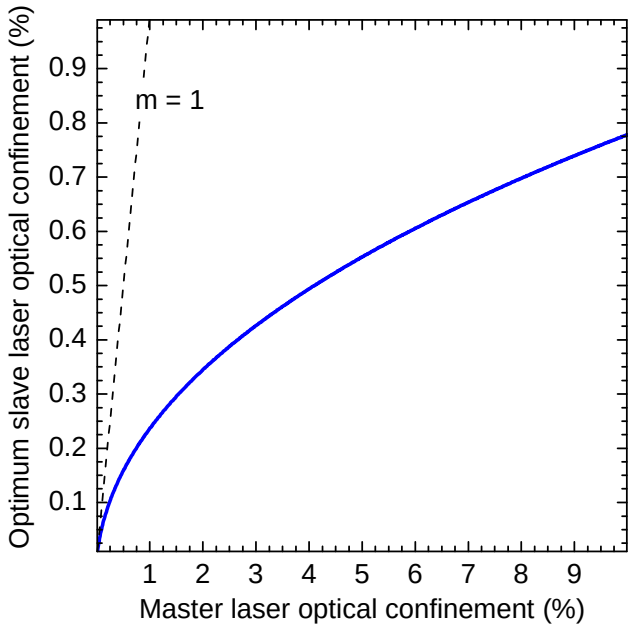

Fig. 3.4. Optimum slave laser optical confinement versus confinement factor of master laser active region. The master laser active region is a single GaAs quantum well.

IV. MULTIPLE-QUANTUM-WELL MASTER LASER ACTIVE REGION

In the modeling in the previous section, the master laser active region consisted of a single GaAs quantum well only, and the optical confinement of the master laser was increased to achieve higher modal gains that resulted in reduced thresholds for both master and slave lasers. In reality, the optical confinement of a quantum well active region can only be increased to a certain degree depending

on the waveguide design and the core and cladding material compositions. A simpler approach to increase the modal gain of a semiconductor laser is to use multiple quantum wells in the active region rather than a single well. The theory and modeling of the novel internal-optically-pumped dual-wavelength laser diodes developed in the previous section is modified to include a multi-quantum-well (MQW) active region for the master laser.

McIlroy *et al*. suggested the optical confinement factor is nearly proportional to the number of wells if: the total active region width is less than 100 nm, and a separate confinement heterostructure is used [69]. Thus the total confinement can be considered as

$$\Gamma = n_W \Gamma_W = \frac{V_a}{V_c} = n_W \frac{V_W}{V_c} \tag{3.38}$$

where n_W is the number of quantum wells, Γ_W is the confinement of an individual well, and V_W is the volume of the well. It is assumed each quantum well in the structure is exactly the same. If the injection into the wells is uniform, the total current is

$$J = \frac{n_W}{\eta_i} J_W \tag{3.39}$$

where J_W is the current injected into each well and η_i is the injection efficiency of the terminal current into the entire active region. From the logarithmic gain-current relation, the total modal gain for a multi-quantum-well structure is

$$n_W \Gamma_W g_W = n_W \Gamma_W g_0 \ln\left(\frac{n_W J_W}{n_W J_{tr}}\right) = n_W \Gamma_W g_0 \ln\left(\frac{\eta_i J}{n_W J_{tr}}\right) \tag{3.40}$$

In Fig. 3.5 the modal gain curves are shown for different GaAs multi-quantum-well active regions with increasing number of wells. Comparing the curves in Fig. 3.5 and inspection of (3.40) shows the gain produced by a MQW structure is simply the gain-current relation of a single well with both the horizontal current axis and the vertical gain axis scaled by a factor n_W .

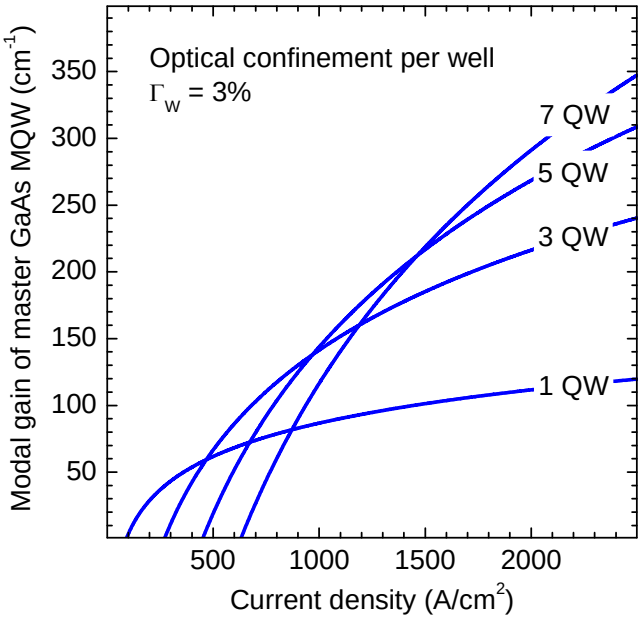

Fig. 3.5. The increase in modal gain of the master GaAs MQW laser active region with added QW. Each quantum well is 10 nm wide with 3% optical confinement per well.

If the total cavity loss is low, increasing the number of quantum wells may not result in lower current thresholds. For example in Fig. 3.5, if the cavity loss is less than 30 cm^{-1}, the current threshold is lowest for one quantum well in the active region, whereas if the loss is 60-130 cm^{-1}, the optimum number of quantum wells is three. To determine the optimum number of wells for a laser diode, McIlroy *et al.* derived the following equation [69].

$$n_W^{opt} = \left(\frac{1}{\Gamma_W g_0}\right)\left(\frac{1}{2L}\ln\left(\frac{1}{R_1 R_2}\right) + \alpha_i\right) \tag{3.41}$$

They also show that for a fixed number of quantum wells, an optimum cavity length can also be found for minimizing the total current threshold.

$$L_{opt} = \frac{1}{2n_W \Gamma_W g_0}\ln\left(\frac{1}{R_1 R_2}\right) \tag{3.42}$$

They are careful to point out the two optimizations cannot be repeated iteratively since this would result in an infinitely short cavity with an infinite number of wells. By extending the model of the novel internal-optically-pumped dual-wavelength laser diodes to include a MQW active region for the master laser, an optimum number of quantum wells can also be determined for the novel dual-wavelength laser.

The rate equation for a MQW active region remains unchanged if uniform injection is assumed for the wells. It is however, important to distinguish between the total current injection and the total volume of the active region versus the injection and volume of the individual quantum wells. For a MQW active region the rate equation is

$$\eta_i \frac{J}{qd} = \eta_i \frac{n_W J_W}{q n_W d_W} = An + Bn^2 + Cn^3 + v_g g(n) S \tag{3.43}$$

where d is the total active layer thickness and d_W is the thickness of an individual quantum well. The thicknesses of all of the wells in the MQW active region are assumed equal. It can be shown that the gain in the term for the stimulated recombination remains the material or local gain of only one of the

wells. From the pinning of the carrier density and gain at threshold, the photon density is

$$S = \frac{\eta_i}{q n_W d_W v_g g_{th}} (J - J_{th}) \tag{3.44}$$

In modifying the internal optical pumping model to include a MQW master laser active region, the threshold gain and current density of the master laser are

$$n_W \Gamma_W g_{th}^M = n_W \Gamma_W g_0^M \ln\left(\frac{\eta_i^M J_{th}^M}{n_W J_{tr}^M}\right) = \alpha_m + \alpha_i + \Gamma_S \alpha_S \tag{3.45}$$

and

$$J_{th}^M = \frac{n_W}{\eta_i^M} J_{tr}^M \exp\left(\frac{\alpha_m + \alpha_i + \Gamma_S \alpha_S}{n_W \Gamma_W g_0^M}\right) \tag{3.46}$$

respectively, for n_W quantum wells. For a photon density S_M produced by the master active region, the carrier generation in the slave active region is

$$G_S = \frac{V_c^M}{V_S} \Gamma_S v_g \alpha_S S_M . \qquad [\text{cm}^{-3} \cdot \text{s}^{-1}] \tag{3.47}$$

From (3.38), for a multi-quantum-well active region, the cavity volume is

$$V_c^M = \frac{V_W}{\Gamma_W} \tag{3.48}$$

and by substitution, the generation rate in the slave is then

$$G_S = \frac{V_W}{V_S} \frac{\Gamma_S}{\Gamma_W} v_g \alpha_S S_M . \tag{3.49}$$

Since the cavity length and lateral width are the same for both the master and slave laser active regions, the ratio of the volumes is simply the ratio of the quantum well widths

$$G_S = \frac{d_W}{d_S}\frac{\Gamma_S}{\Gamma_W} v_g \alpha_S S_M \tag{3.50}$$

where d_W is the width of only one of the quantum wells in the master region.

As noted earlier, an effective current generation can be defined from (3.50) so the logarithmic gain-current relation can be used to predict the gain in the slave active region. From the modal losses, the threshold gain and threshold optical current density of the slave are found, and the threshold generation rate in the slave laser active region is then

$$G_S^{th} = \frac{J_{tr}^S}{qd_s}\exp\left(\frac{\alpha_m + \alpha_i}{\Gamma_S g_0^S}\right). \tag{3.51}$$

The photon density which sufficiently pumps the slave to achieve this generation rate is the threshold photon density

$$S_M^{th-S} = G_S^{th}\frac{d_S}{d_W}\frac{\Gamma_W}{\Gamma_S}\frac{1}{v_g \alpha_S} \tag{3.52}$$

and the threshold current density for the slave laser is

$$J_{th}^S = S_M^{th-S} \cdot \frac{qn_W d_W v_g g_{th}^M}{\eta_i^M} + J_{th}^M \ . \tag{3.53}$$

As noted earlier, this threshold is the applied current to the diode needed so the master laser pumps the slave laser to its threshold.

Substitution of (3.51) and (3.52) into (3.53) leads to the following expression for the current threshold of the slave laser.

$$J_{th}^{S} = \frac{(\alpha_m + \alpha_i + \Gamma_S \alpha_S)}{\Gamma_S \alpha_S \eta_i^M} \cdot J_{tr}^{S} \exp\left(\frac{\alpha_m + \alpha_i}{\Gamma_S^{\lambda_S} g_0^S}\right) + \frac{n_W}{\eta_i^M} J_{tr}^{M} \exp\left(\frac{\alpha_m + \alpha_i + \Gamma_S \alpha_S}{n_W \Gamma_W g_0^M}\right) \tag{3.54}$$

Comparing to expression (3.36) for a single quantum well master laser active region, the first term or optical pumping term is unchanged and decays with increasing optical confinement of the slave laser. The second term is still the threshold current of the master laser, and the only difference compared to (3.36) is the adjustment for multiple quantum wells in the master active region. If the number of wells is one, (3.54) simply reduces to (3.36) as expected.

As in the previous section, the optical confinement of the slave laser active region is varied in the modeling to illustrate its impact on the current thresholds of both the master and slave lasers. Rather than increasing the optical confinement of the quantum wells in the master laser active region, the confinement is held constant in the modeling at 3% per quantum well, and the number of quantum wells in the master MQW laser active region is then increased. In Fig. 3.6 the two terms on the right-hand side of (3.54) are calculated versus the optical confinement factor of the slave laser. The first term or internal optical pumping term, labeled ζ, is the decaying curve in Fig. 3.6 and is independent of the number of quantum wells in the master laser active region. As before the threshold of the slave is graphically the sum of the ζ curve with the one of the increasing curves depending on the number of wells in the master active region.

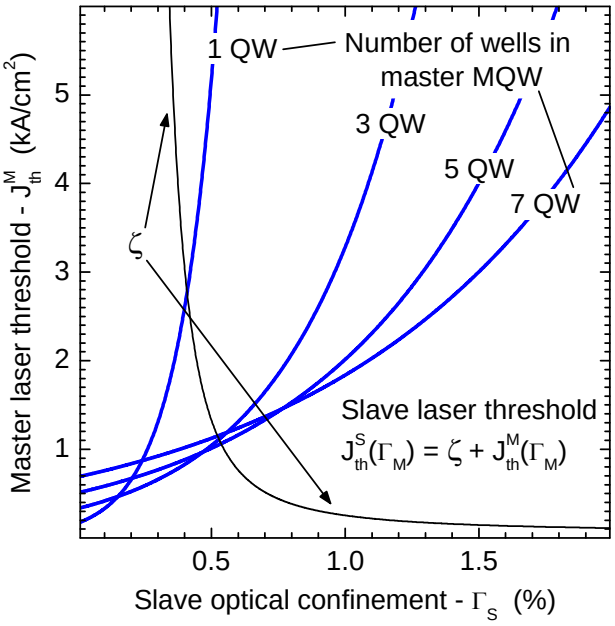

Fig. 3.6. Threshold current density of the master MQW laser versus the slave optical confinement for increasing number of wells in the MQW active region.

From Fig. 3.6, a significant reduction in the threshold of the slave laser is expected when the number of wells in the master MQW active region is increased from a single quantum well. This is evident in Fig. 3.7 where the calculated threshold curves of the slave laser are plotted versus the optical confinement of the slave laser active region for increasing numbers of wells in the master MQW laser active region. As in the single quantum well case, a minimum in the threshold current of the slave is observed at an optimum optical confinement of the slave laser due to the combined effects of the increasing modal gain of the slave laser and the increasing modal absorption loss to the master laser with increased optical confinement of the slave region.

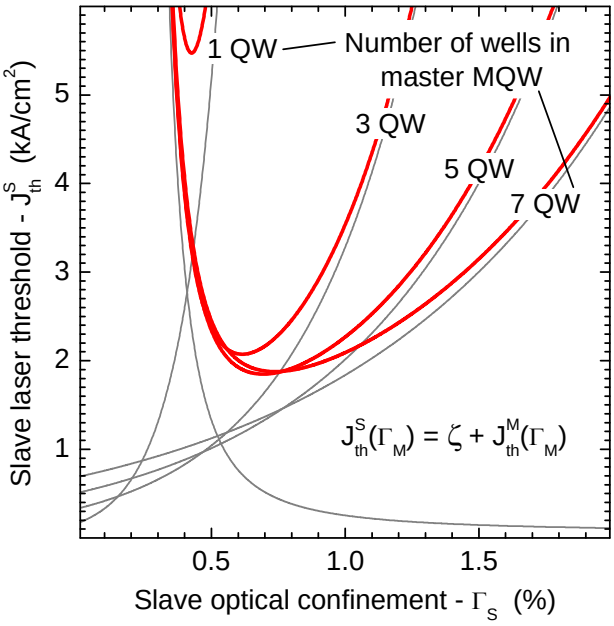

Fig. 3.7. Threshold current density of the slave laser for 1, 3, 5, and 7 quantum wells in the master MQW laser active region. The minimum in the threshold current corresponds to the optimum optical confinement of the slave.

Some interesting observations are made from the results in Fig. 3.7 that are the basis of important design considerations for the novel internal-optically-pumped dual-wavelength laser diode. As expected the threshold of the slave laser first decreases sharply from that of a single master quantum well with the addition of one or two wells in the master laser active region. The decrease in threshold is less for further additional quantum wells, and slight increases in the threshold are predicted by the modeling for each additional well beyond five wells in the active region of the master laser. This increase in threshold with further addition of quantum wells is just as in conventional MQW lasers, and an optimum number of quantum wells exists for the master laser active region in the novel dual-wavelength device.

In Table III.IV, the minimum thresholds of the slave laser and the corresponding optimum optical confinement of the slave are listed for increasing number of master quantum wells. The master laser thresholds are also listed for this optimum optical confinement of the slave laser at which the slave laser threshold is lowest. The data is plotted in Fig. 3.8, and in addition to an optimum number of master quantum wells at which the threshold of the slave laser is the lowest, an optimum number of wells also exists at which the master laser threshold is minimum. For the slave laser, the optimum number of master quantum wells is five, and the threshold current density is 1848 A/cm^2. However for the master laser, the optimum number of wells is four, and the master threshold is 1308 A/cm^2. If the number of wells is increased to five to match the optimum number for the slave laser, the threshold of the master laser increases only to 1322 A/cm^2, and thus five quantum wells in the master laser active region is considered ideal for the novel dual-wavelength device.

TABLE III.IV
OPTIMUM OPTICAL CONFINEMENT AND THRESHOLDS FOR MULTI-QUANTUM-WELL MASTER LASER ACTIVE REGION

Number of wells in master MQW laser active region	Minimum slave laser threshold (A/cm^2)	Optimum slave laser optical confinement (%)	Master laser threshold at optimum slave confinement (A/cm^2)
1	5473	0.43	3112
2	2605	0.55	1605
3	2073	0.62	1360
4	1901	0.66	1308
5	1848	0.69	1322
6	1849	0.72	1362
7	1877	0.74	1419
8	1922	0.75	1485

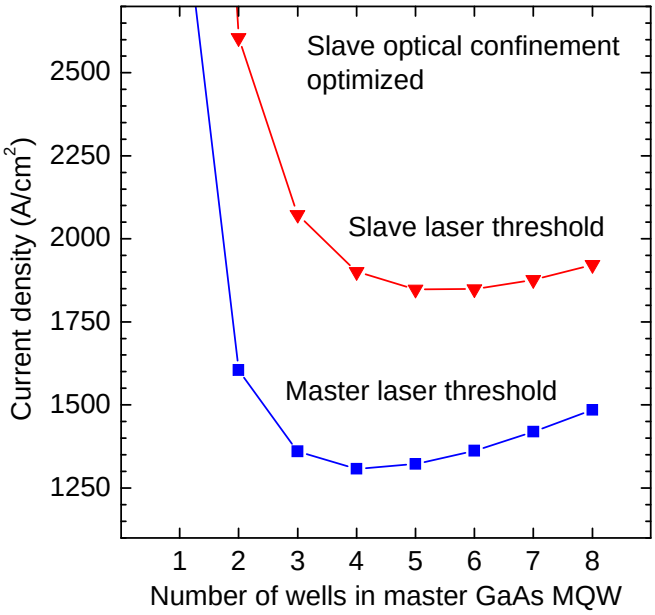

(a)

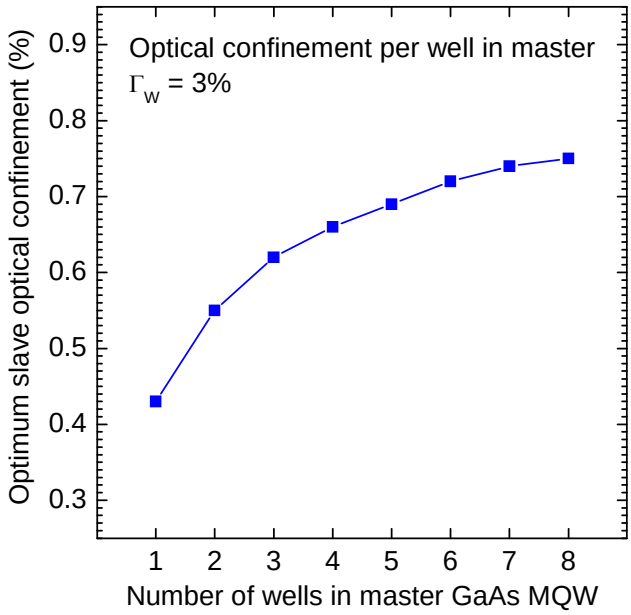

(b)

Fig. 3.8. (a) Optimum threshold current densities of the master and slave regions. (b) Optimum slave confinement versus number of QW included in the master active region. L= 1000 μm.

The second observation from Fig. 3.6 and Fig. 3.7 that is useful in considering the design of the novel internal-optically-pumped dual-wavelength laser is the change in thresholds of the master and slave lasers with the optical confinement of the slave for the different number of wells in the master MQW active region. In Fig. 3.7, on the left-hand side of the graph, the slave laser threshold increases sharply with reducing optical confinement of the slave regardless of the number of wells in the master MQW active region. The internal optical pumping term which is independent of the number of wells is the dominant term on this side of the curve in the equation for the slave laser threshold, and the slave threshold increases sharply due to the reduction in the modal gain of the slave laser. On the right-hand side of the graph, the thresholds of both the master and slave lasers increase; however, the rate of increase with optical confinement of the slave decreases with additional quantum wells in the master laser active region. This behavior results in larger tolerance of variations in the optical confinement factor of the slave with additional quantum wells in the master active region and is valuable in the actual design and growth of the novel internal-optically-pumped dual-wavelength laser diode.

An increase in the modal gain of the master by the addition of active quantum wells helps to offset the absorption loss introduced by the slave laser active region and results in a lower threshold of the master laser. The data in Table III.IV also confirms an increase in the optimum optical confinement of the slave with additional quantum wells in the master laser active region and a resulting decrease in the slave laser threshold. Whereas this increase results in a

higher modal absorption loss to the master, the threshold of the master laser is still reduced as the increase in the modal gain is greater than the increase in the modal absorption loss.

V. CAVITY LENGTH VARIATION

Finally, the impact of the cavity length in the novel internal-optically-pumped dual-wavelength laser diode is investigated by varying it in the modeling. As in conventional laser diodes, the thresholds of the master and slave lasers are both reduced for longer cavity lengths due to the reduced mirror loss. However, additional effects are observed in the predicted performance of the dual-wavelength laser and the threshold current of the slave laser. In considering the optimum optical confinement and threshold of the slave laser (3.54), variation of the cavity length results in a greater change of the internal optical pumping term than in the master threshold since the mirror loss is much less than the modal absorption loss of the slave in determining the master threshold. This is seen in Fig. 3.9 where the thresholds of the master and slave lasers are calculated versus the optical confinement of the slave for a 500 μm cavity and a 1000 μm cavity. A significant reduction in the internal optical pumping term ζ is observed when the cavity length is increased which results in a further reduction of the minimum and optimum slave laser threshold.

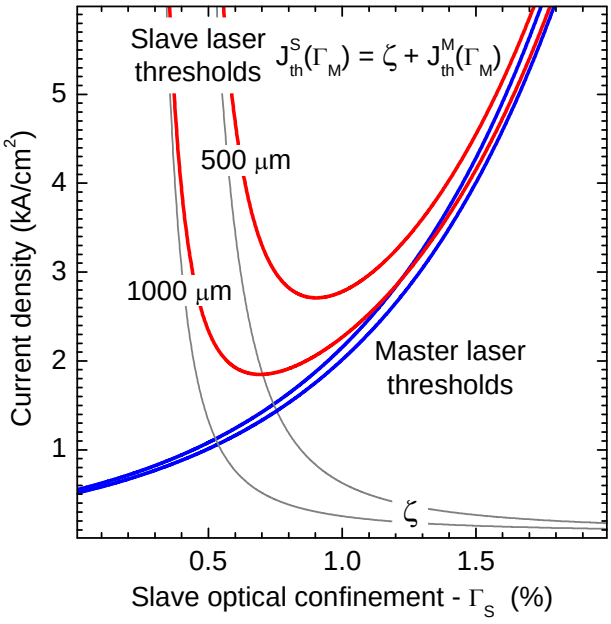

Fig. 3.9. The thresholds of the master and slave lasers as a function of the optical confinement of the slave and the cavity length.

The reduction in the internal optical pumping term ζ with cavity length not only results in a reduction of the minimum slave laser threshold but also results in a reduction of the corresponding optimum optical confinement of the slave as observed in Fig. 3.9. From the modeling, the optimum optical confinement of the slave laser is calculated as a function of the cavity length, and the result is shown in Fig. 3.10. Since the optimum optical confinement of the slave laser varies with cavity length, the theoretical optimum thresholds of the master and slave lasers are therefore also dependent on the cavity length.

If the cavity length is predetermined, the dual-wavelength laser can be designed and grown with the optimum slave optical confinement for the lowest slave threshold. However, if the cavity length is varied and the optical confinement of the slave is held constant, the thresholds of the master and slave

lasers will deviate from the theoretical optimum thresholds. In the modeling, the thresholds of the master and slave lasers are calculated versus cavity length for a constant slave optical confinement of 0.69% which is the optimum confinement for a cavity length of 1000 μm. These thresholds are then compared to the optimum thresholds where the optimum slave optical confinement is used in the calculations at each cavity length. The results are in Fig. 3.11 and reveal the cavity length can be reduced to 606 μm and increased to 1437 μm for a constant slave optical confinement of 0.69% before either the threshold of the master or slave laser is greater than 10% of the optimum thresholds.

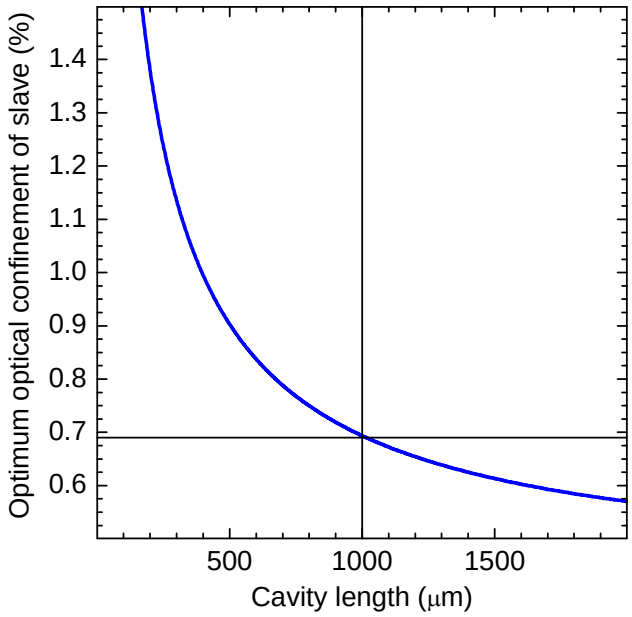

Fig. 3.10. The optimum optical confinement of the slave laser at which the threshold of the slave laser is minimized as a function of the cavity length.

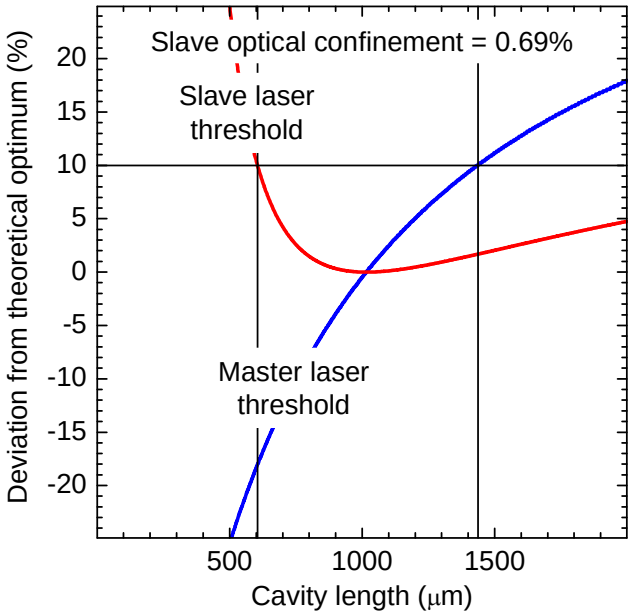

Fig. 3.11. Deviation of the master and slave lasers from the optimum thresholds where the slave optical confinement is optimized. The slave optical confinement is held constant at 0.69% which is the optimum optical confinement for a cavity length of 1000 μm.

VI. SUMMARY

In this chapter the theory and a corresponding model of the internal optical pumping scheme for the dual-wavelength laser diode has been developed, and the modeling reveals optimization of the optical confinement of the slave laser active region is critical to lowering the threshold of the slave laser and enabling dual-wavelength output. In addition, the thresholds of the two lasers can be further reduced by increasing the optical confinement of the master laser active region and increasing the cavity length. The modeling predicts an optimum number of 5 quantum wells in the master laser active region with 3% optical confinement per well, and the optimum optical confinement of the slave is then 0.69% for a cavity length of 1000 μm. These results will serve as useful guidelines in designing

specific device structures to implement the internal optical pumping scheme and experimentally realize the novel dual-wavelength laser diodes.

4 Device Modeling Methods

To develop real laser diodes with dual-wavelength behavior using the internal optical pumping scheme, it is critical to design devices that have decoupled active regions in terms of the quasi-Fermi distributions and second have optimized optical confinement factors as was demonstrated in chapter three. In order to better understand the different device designs it is important to be able to model and predict their performance, and methods to model the different aspects of the device are outlined in this chapter. An appropriate level of detail is incorporated in the models to make the results as predictive as possible to the actual device performance, and yet, some general assumptions and simplifications are made to keep the modeling simple and efficient. First, the method of calculating the optical mode profiles and optical confinement factors of the laser structures is presented. A few adjustments to the internal optical pumping model are required to include effects such as free-carrier absorption and to better match the model to actual device designs, and these considerations are covered second. Third, the methods for modeling the carrier transport and quasi-Fermi distributions in the device structures are introduced in this chapter.

I. CALCULATION OF CAVITY OPTICAL MODES

Different methods exist for calculating the optical modes and confinement factors of laser diodes. These methods include analytical, various finite-difference, and transfer matrix methods among others to calculate the optical modes of a waveguide. Here a finite-difference approach as outlined by Coldren

and Corzine is chosen to form a matrix eigenvalue equation from the wave equation for the electric field of a supported optical mode [68]. For the novel internal-optically-pumped dual-wavelength laser structures, a graded-index separate-confinement-heterostructure (GRINSCH), is chosen as a starting point for the designs, and a significant advantage to the finite-difference method is the ability to solve for the field in regions with graded refractive index whereas the transfer matrix method cannot solve the profile in these regions due to the inherit dependence on discrete boundaries.

The finite-difference method for calculating the optical modes is outlined starting from Maxwell's equations and derivation of the wave equation. Maxwell's equations for a dielectric medium that is linear, nondispersive, homogeneous, isotropic, and source-free are as follows:

$$\nabla \times \mathbf{H} = \varepsilon \frac{\partial \mathbf{E}}{\partial t} \tag{4.1}$$

$$\nabla \times \mathbf{E} = -\mu \frac{\partial \mathbf{H}}{\partial t} \tag{4.2}$$

$$\nabla \cdot \mathbf{E} = 0 \tag{4.3}$$

$$\nabla \cdot \mathbf{H} = 0 . \tag{4.4}$$

Applying the curl operation $\nabla \times$ to 4.2

$$\nabla \times (\nabla \times \mathbf{E}) = -\mu \nabla \times \frac{\partial \mathbf{H}}{\partial t} \tag{4.5}$$

using the identity

$$\nabla \times (\nabla \times \mathbf{E}) = \nabla (\nabla \cdot \mathbf{E}) - \nabla^2 \mathbf{E} \tag{4.6}$$

and substituting 4.3 leads to

$$\nabla^2 \mathbf{E} = \mu \frac{\partial}{\partial t}(\nabla \times \mathbf{H}) . \tag{4.7}$$

The wave equation for the electric field of a propagating electromagnetic wave is then found using 4.1

$$\nabla^2 \mathbf{E} = \mu\varepsilon \frac{\partial^2 \mathbf{E}}{\partial t^2} . \tag{4.8}$$

As a coordinate system, $\hat{z}$ is chosen as the longitudinal or propagating direction, $\hat{x}$ the growth or transverse direction, and $\hat{y}$ as the lateral direction, and for transverse electric or TE polarized waves, the electric field takes the form

$$\mathbf{E}(x, y, z, t) = \hat{y} E_0 U(x, y) e^{j(\omega t - \beta z)} \tag{4.9}$$

where $U(x, y)$ is the transverse field profile and is normalized so

$$\int_{-\infty}^{\infty} \left| U(x, y) \right|^2 dxdy = 1 . \tag{4.10}$$

By substituting 4.9 into the wave equation 4.8 and factoring out common terms, the Helmholtz equation is found which is an eigenvalue equation for the field profile.

$$\nabla^2 U(x, y) + [\omega^2 \mu\varepsilon - \beta] U(x, y) = 0 \tag{4.11}$$

$$\nabla^2 U(x, y) + k_0^2 [n^2 - n_{eff}^2] U(x, y) = 0 \tag{4.12}$$

The field profile for the mode of a waveguide can be calculated from the Helmholtz equation where the refractive index term varies spatially with the geometry of the waveguide $n(x, y)$.

For broad-area lasers, the overall confinement factor is determined largely by the confinement in the transverse or growth direction, so a 1-D case is assumed

to simplify the modeling where $U(x)$ is the profile of the electric field of the optical mode in the transverse direction. To calculate the profile, the finite difference method outlined by Coldren and Corzine [68] is used with a second-order Taylor series expansion, so

$$U(x+\Delta x) = U(x) + \Delta x \frac{dU(x)}{dx} + \frac{(\Delta x)^2}{2}\frac{d^2U(x)}{dx^2} \tag{4.13}$$

$$U(x-\Delta x) = U(x) - \Delta x \frac{dU(x)}{dx} + \frac{(\Delta x)^2}{2}\frac{d^2U(x)}{dx^2} \tag{4.14}$$

$$\frac{d^2U(x)}{dx^2} = \frac{U(x+\Delta x) - 2U(x) + U(x-\Delta x)}{(\Delta x)^2}. \tag{4.15}$$

The space in the transverse direction is discretized

$$x = i\Delta x \quad \text{where} \quad i = 0, 1, 2 \ldots I+1 \tag{4.16}$$

and the second order differential becomes

$$\frac{d^2U(x)}{dx^2} = \frac{U_{i+1} + 2U_i + U_{i-1}}{(\Delta x)^2}. \tag{4.17}$$

The finite-difference discrete form of the Helmholtz equation for the field profile is then

$$\frac{U_{i+1} + 2U_i + U_{i-1}}{(\Delta x)^2} + k_0^2(n_i^2 - n_{eff}^2)U_i = 0. \tag{4.18}$$

Next, by defining the term

$$\Delta X^2 = k_0^2 \Delta x^2 \tag{4.19}$$

and rearranging the terms, the Helmholtz equation for the field profile can now be written as a matrix eigenvalue equation

$$\frac{U_{i-1}}{\Delta X^2} - \left(\frac{2}{\Delta X^2} - n_i^2 \right) U_i + \frac{U_{i+1}}{\Delta X^2} = n_{eff}^2 U_i \tag{4.20}$$

where the refractive index n_i can vary spatially with each discrete element to calculate the profile of the field of a guided optical mode. In order to solve for the field profile, boundary conditions must be specified. A simple choice is to make the computational window large enough, so that the boundary is far enough away from the guiding layer of the waveguide so the field is effectively zero at the boundary so

$$U_0 = U_{I+1} = 0 . \tag{4.21}$$

With these boundary conditions, the matrix eigenvalue equation then takes the form

$$\begin{bmatrix} \left(n_1^2 - \frac{2}{\Delta X^2} \right) & \frac{1}{\Delta X^2} & 0 & 0 \\ \frac{1}{\Delta X^2} & \left(n_2^2 - \frac{2}{\Delta X^2} \right) & \frac{1}{\Delta X^2} & 0 \\ 0 & & \mathrm{O} & \\ 0 & 0 & \frac{1}{\Delta X^2} & \left(n_I^2 - \frac{2}{\Delta X^2} \right) \end{bmatrix} \begin{bmatrix} U_1 \\ U_2 \\ \mathrm{M} \\ U_I \end{bmatrix} = n_{eff}^2 \begin{bmatrix} U_1 \\ U_2 \\ \mathrm{M} \\ U_I \end{bmatrix} \tag{4.22}$$

where the eigenvalue n_{eff}^2 is the square of the effective index of the traveling optical mode, and the eigenvector $\mathbf{U}$ is the field profile. These values can be solved quickly and with relative ease by employing built-in matrix-solving functions found in most numerical software packages such as MATLAB.

For the TE modes of a laser diode cavity, it can be shown that the optical confinement factor is [67]

$$\Gamma = \frac{\int\int_{\text{active}} \left|E_y(x,y)\right|^2 dxdy}{\int_{-\infty}^{\infty}\int_{-\infty}^{\infty} \left|E_y(x,y)\right|^2 dxdy}. \tag{4.23}$$

In the 1-D case, substituting 4.9 and factoring out the common terms, the optical confinement factor becomes

$$\Gamma = \frac{\int_{\text{active}} \left|U(x)\right|^2 dx}{\int_{-\infty}^{\infty} \left|U(x)\right|^2 dx} \approx \frac{\sum_{\text{active}} \left|U_i\right|^2}{\sum_{i=1}^{i=I} \left|U_i\right|^2}. \tag{4.24}$$

Thus the optical confinement factor can be computed by summing the squares of the individual elements of the field profile corresponding spatially to the active region and dividing this by the sum of the squares of all of the elements. The refractive indexes of the different materials used in the dual-wavelength heterostructures are listed in Table IV.I. For the graded regions, linear interpolation of the refractive indexes is used in the modeling.

TABLE IV.I
REFRACTIVE INDICES IN MODELING OPTICAL MODES
OF DUAL-WAVELENGTH LASER DESIGNS

Material	n (λ=850 nm)	n (λ=1020 nm)
$In_{0.24}Ga_{0.76}As$	3.68302	3.61904
GaAs	3.6442	3.4995
$Al_{0.2}Ga_{0.8}As$	3.4634	3.3979
$Al_{0.3}Ga_{0.7}As$	3.3889	3.3390
$Al_{0.7}Ga_{0.3}As$	3.1377	3.0944
$Al_{0.75}Ga_{0.25}As$	3.1262	3.0795

II. ADJUSTMENTS FOR FREE-CARRIER AND BARRIER ABSORPTION

In the novel internal-optically-pumped dual-wavelength laser diode design the slave laser active region is placed within the quasi-neutral doped region and not within the intrinsic region of the *p*-*i*-*n* junction, and free-carrier absorption and its impact on the threshold of the dual lasers are important considerations. In considering different detailed designs implementing the internal optical pumping scheme, the free-carrier absorption is evaluated by comparing the optical field profile with the doping profile. Casey and Panish note the free-carrier absorption near the GaAs band edge at room temperature is

$$\alpha_{fc} \approx 3\times10^{-18} n + 7\times10^{-18} p \qquad [\text{cm}^{-1}] \tag{4.25}$$

where n and p are the electron and hole concentrations respectively [73]. For the device structures examined here, this relation is considered to also be a reasonable approximation for free-carrier absorption in the $Al_xGa_{1-x}As$ layers. It is also assumed the electron or hole concentration in a doped region of the device is equal to the doping concentration.

The free-carrier absorption loss introduced by a doped region depends on the optical mode and the overlap of the mode with the region or the confinement factor. The optical mode of the overall structure is calculated using the matrix eigenvalue method outlined previously. The contribution of a region within the heterostructure laser device to the total free-carrier absorption loss can be calculated from the doping level and optical confinement factor of that specified region. The total free-carrier absorption loss is then simply the sum of the contributions from the different *n* and *p* regions

$$\alpha_{fc} = \sum_k \Gamma_k \cdot 3\times10^{-18} \cdot n_k + \sum_l \Gamma_l \cdot 7\times10^{-18} \cdot p_l \qquad (4.26)$$

where each region has a different doping or carrier concentration. It will be shown that for the different designs considered here, the highest total free-carrier absorption loss of any of the devices is 4.7 cm^{-1}, which is insignificant compared to the modal absorption loss introduced with the addition of the slave laser active region.

Material growth issues arise in growing InGaAs directly on $Al_xGa_{1-x}As$, and InGaAs quantum wells are grown with GaAs barrier layers. In the novel internal-optically-pumped dual-wavelength laser structures, the $Al_xGa_{1-x}As$ layers are transparent to the 850 nm light generated by the master laser GaAs MQW. However, the GaAs barrier layers of the $In_{0.24}Ga_{0.76}As$ slave laser quantum well are not transparent and introduce an additional absorption into the equations and model of the novel dual-wavelength device. In developing the model and the theory in the chapter three, this detail was omitted, but the model is adjusted to include it in evaluating specific structures and growth designs.

The additional absorption of the barrier layers adds to the total modal absorption loss the slave laser active region introduces to the master laser, so the total loss is

$$\Gamma_S \alpha_S + \Gamma_b \alpha_b \,. \qquad (4.27)$$

The assumption is made that the photo-generated carriers in the barriers layers scatter to the slave quantum well, and from the modal absorption loss the carrier generation rate inside the slave laser quantum well is

$$G_S = \frac{V_c^M}{V_S} v_g (\Gamma_S \alpha_S + \Gamma_b \alpha_b) S_M \tag{4.28}$$

where V_c^M is the master laser cavity volume and S_M is the photon density. Assuming the carriers in the barrier scatter to the quantum well, the volume V_S is the volume of the InGaAs quantum well only and does not include the volume of the GaAs barrier layers. The barrier absorption effectively increases the absorption coefficient of the slave quantum well as V_c^M and V_S in 4.28 are unchanged with or without the barrier layers. From the ratio of the optical confinement factor of the barrier layers to that of the slave quantum well

$$X = \frac{\Gamma_b}{\Gamma_S} \tag{4.29}$$

an effective slave absorption coefficient α_S' can be defined

$$\alpha_S' = \alpha_S + X\alpha_b \,. \tag{4.30}$$

With this definition, the modal absorption loss to the master laser and the carrier generation within the slave laser active region simplify to

$$\Gamma_S \alpha_S' \tag{4.31}$$

$$G_S = \frac{V_c^M}{V_S} v_g \Gamma_S \alpha_S' S_M \tag{4.32}$$

which resemble the equations of the model without barrier absorption. The model developed previously can then easily be adjusted to include absorption in the barrier layers of the slave laser quantum well by substituting in the effective absorption α_S for the actual slave absorption coefficient α_S. For the dual-

wavelength structures developed in this chapter, the absorption in the GaAs barrier layers at λ = 850 nm is 9,048 cm^{-1} compared to 24,768 cm^{-1} at the same wavelength in the $In_{0.24}Ga_{0.76}As$ slave quantum well.

III. MODELING SUB-THRESHOLD CARRIER DYNAMICS

In the internal-optically-pumped dual-wavelength laser diode design, it is critical that the master and slave laser active regions are electrically decoupled so the quasi-Fermi levels/distributions are distinct for each region. Further, the internal optical pumping model developed in the previous chapter assumes negligible injection of carriers into the slave active region due to current leakage from the junction, meaning the current injection efficiency for the slave laser active region should be near zero. To validate this assumption and better understand the decoupling of the quasi-Fermi levels between the two active regions, the carrier transport and electrical behavior of various implementations of the novel dual-wavelength device are modeled under applied biases and currents below the laser thresholds. The devices are simulated using Silvaco's ATLAS device simulation software. ATLAS is described as a physically-based device simulator in that a set of differential equations derived from Maxwell's equations is applied to a discrete two or three dimensional grid representative of the physical device structure to simulate its behavior, providing valuable insight and visualization of the theoretical equations [74].

To better understand the functionality and results produced by Silvaco's ATLAS, the physical equations and models used in the simulations of the novel

dual-wavelength designs are described here briefly. The software relies on solving Poisson's equation which relates the electric field $\mathbf{E}$ to the charge density ρ

$$\nabla \cdot \mathbf{E} = \frac{\rho(x, y, z)}{\varepsilon} \tag{4.33}$$

where the charge density is made up of free electrons and holes and ionized donors and acceptors. The electrostatic potential ϕ can then be found from the electric field using

$$\nabla \phi = -\mathbf{E} . \tag{4.34}$$

The continuity equations equate the time rate of change of the carrier concentration *n* or *p* to the generation rate G_n, recombination rate R_n, and current density J

$$\frac{\delta n}{\delta t} = G_n - R_n + \frac{1}{q} \nabla \cdot \mathbf{J}_n \tag{4.35}$$

$$\frac{\delta p}{\delta t} = G_p - R_p - \frac{1}{q} \nabla \cdot \mathbf{J}_p . \tag{4.36}$$

The current density equations consist of drift and diffusion components

$$\mathbf{J}_n = q\mu_n n\mathbf{E} + qD_n \nabla n \tag{4.37}$$

$$\mathbf{J}_p = q\mu_p p\mathbf{E} - qD_p \nabla p \tag{4.38}$$

where $\mu_{n,p}$ and $D_{n,p}$ are the mobility and diffusion parameters respectively. The current density equations can be inserted into the continuity equations, and the continuity equations and Poisson's equation then form a set of three equations with three unknowns: the electron concentration n, hole concentration p, and

electrostatic potential ϕ. The ATLAS simulator solves discrete forms of these equations and up to six coupled equations may then need to be solved [74].

Boundary conditions are required to solve Poisson's equation and the continuity equations, and it is assumed on the surface of an ideal ohmic contact that space-charge neutrality is met and the electrostatic potential is equal to the applied voltage plus a reference potential ϕ_0

$$\phi = \phi_0 + V_{\text{applied}} . \tag{4.39}$$

Additionally the carrier concentrations at the contact are equal to their equilibrium values

$$n = n_0 \tag{4.40}$$

$$p = p_0 \tag{4.41}$$

and the quasi-Fermi potentials satisfy

$$\phi_n = \phi_p = V_{\text{applied}} \tag{4.42}$$

with the quasi-Fermi potentials related to the quasi-Fermi levels F_n and F_p by

$$\phi_{n,p} = -\frac{1}{q} F_{n,p} . \tag{4.43}$$

To evaluate the generation and recombination terms in the continuity equations, Shockley-Read-Hall (SRH), radiative, and Auger mechanisms are considered in ATLAS. The simplest form describing SRH used by ATLAS and in simulations of the novel dual-wavelength structures is

$$R_n - G_n = R_p - G_p = \frac{np - n_i^2}{\tau_n\left[n + n_i \exp\left(\frac{E_t - E_i}{kT}\right)\right] + \tau_p\left[p + p_i \exp\left(\frac{E_i - E_t}{kT}\right)\right]}. \quad (4.44)$$

In the simulations of the dual-wavelength laser devices, it is assumed the trap energy levels are equal to the intrinsic energy level, $E_t = E_i$, which simplifies the expression further. The SRH lifetimes τ_n and τ_p can be specified in ATLAS for specific semiconductor materials, and the values used in simulating the dual-wavelength designs are listed in Table IV.II. Under high injection where $np >> n_i^2$ and assuming $n \approx p$, it can be shown that the SRH recombination reduces to the familiar form

$$R_{\text{SRH}} = \frac{n}{\tau_n + \tau_p} = An. \quad (4.45)$$

For optical generation/radiative recombination the band to band rate is

$$R_n - G_n = R_p - G_p = B(np - n_i^2) \quad (4.46)$$

and for Auger processes the rates are

$$R_n - G_n = C_n(n^2 p - nn_i^2) \quad (4.47)$$

$$R_p - G_p = C_p(np^2 - pn_i^2) \quad (4.48)$$

where B and $C_{n,p}$ are the respective radiative and Auger coefficients. These values can also be specified in ATLAS for a given material, and the values used in simulating the novel dual-wavelength structures are listed in Table IV.II. The values were collected from the built-in tables in ATLAS [74], Ioffe's [75], Properties of AlGaAs [76], Adachi [77], and Coldren [68].

TABLE IV.II
RECOMBINATION PARAMETERS IN MODELING DWLD DESIGNS

Material	SRH lifetime τ_n (s)	SRH lifetime τ_p (s)	Radiative coeff. – B (cm^3/s)	Auger coeff. C_n (cm^6/s)	Auger coeff. C_p (cm^6/s)
$In_{0.24}Ga_{0.76}As$	2.5×10^{-7}	3×10^{-6}	7×10^{-11}	1×10^{-30}	7×10^{-29}
GaAs (QW)	2.5×10^{-7}	3×10^{-6}	8×10^{-11}	1×10^{-30}	1×10^{-30}
GaAs (bulk)	2.5×10^{-7}	3×10^{-6}	7.2×10^{-10}	1×10^{-30}	1×10^{-30}
$Al_{0.2}Ga_{0.8}As$	4×10^{-9}	2×10^{-9}	1.5×10^{-10}	7×10^{-32}	6.1×10^{-31}
$Al_{0.3}Ga_{0.7}As$	1.5×10^{-8}	1×10^{-9}	1.5×10^{-10}	5×10^{-30}	1×10^{-31}
$Al_{0.5}Ga_{0.5}As$	3×10^{-8}	1×10^{-9}	1.5×10^{-10}	5×10^{-30}	1×10^{-31}
$Al_{0.7}Ga_{0.3}As$	3×10^{-8}	1×10^{-9}	1.5×10^{-10}	5×10^{-30}	1×10^{-31}
$Al_{0.75}Ga_{0.25}As$	3×10^{-8}	1×10^{-9}	1.5×10^{-10}	5×10^{-30}	1×10^{-31}

In calculating the current density, the carrier mobilities listed in Table IV.III for the different materials were used in the simulations. Additionally, in a high electric field, the drift velocity begins to saturate. ATLAS accounts for this by reducing the effective mobility since the drift velocity is the product of the mobility and the electric field component parallel to the current flow. A parallel electric field dependent mobility model in ATLAS adjusts the mobility and provides a smooth transition from low to high electric field behavior. The model uses the following equations relating the mobility and the electric field component parallel to the current flow $E_{\parallel}$,

$$\mu_n(E_{\parallel}) = \mu_{n0}\left[\frac{1}{1+\left(\frac{\mu_{n0}E_{\parallel}}{v_{\text{sat},n}}\right)^{\beta_n}}\right]^{\frac{1}{\beta_n}} \tag{4.49}$$

$$\mu_p(E_{\parallel}) = \mu_{p0}\left[\frac{1}{1+\left(\frac{\mu_{p0}E_{\parallel}}{v_{\text{sat},p}}\right)^{\beta_p}}\right]^{\frac{1}{\beta_p}} . \tag{4.50}$$

In the simulations $\beta_n = 2$ and $\beta_p = 1$, and for all compositions of $Al_xGa_{1-x}As$, including GaAs, the saturation velocity v_{sat} is 7.7×10^6 cm/s for both electrons and holes.

TABLE IV.III
CARRIER DRIFT MOBILITY IN MODELING DWLD DESIGNS, [74] and [75]

Material	Electron mobility – μ_n (cm^2/V-s)	Hole mobility – μ_p (cm^2/V-s)
$In_{0.24}Ga_{0.76}As$	7086	300
GaAs	8000	400
$Al_{0.2}Ga_{0.8}As$	4000	206
$Al_{0.3}Ga_{0.7}As$	2300	146
$Al_{0.5}Ga_{0.5}As$	145	70
$Al_{0.7}Ga_{0.3}As$	204	54
$Al_{0.75}Ga_{0.25}As$	204	54

To model heterojunctions, ATLAS is equipped with a simulator referred to as BLAZE which accounts for position dependent band structures by

modifying the current density equations slightly [74]. Poisson's equation remains the same as for a homogeneous structure except the dielectric constant is position dependent. The continuity equations also remain the same, but the current equations are altered and take the form

$$\mathbf{J}_n = -\mu_n n \nabla \phi_n \tag{4.51}$$

$$\mathbf{J}_p = -\mu_p p \nabla \phi_p \tag{4.52}$$

To determine the quasi-Fermi potentials, the conduction and valence band edges in BLAZE are determined from the electrostatic potential by

$$E_c = -q(\phi - \phi_0) - \chi \tag{4.53}$$

$$E_v = -q(\phi - \phi_0) - \chi - E_g \tag{4.54}$$

where the electron affinity χ and the band gap E_g are position dependent based on the heterostructure. In the BLAZE simulator, the band offsets of a heterojunction can be specified, and the electron affinity of the material is then modified by the simulator to produce the specified offsets in the position-dependent structure. For the AlGaAs/GaAs/InGaAs junctions in the novel dual-wavelength structures, the following band offsets were selected for all heterojunctions within the structure:

$$\Delta E_c = 0.65 \cdot \Delta E_g \tag{4.55}$$

$$\Delta E_v = 0.35 \cdot \Delta E_g . \tag{4.56}$$

The quasi-Fermi levels and potentials can be calculated from the band edges and the carrier concentrations using Fermi-Dirac statistics with the electron and hole density-of-state functions $\rho_e(E)$ and $\rho_h(E)$:

$$n = \int_{-\infty}^{\infty} f_n(E)\rho_e(E)dE \tag{4.57}$$

$$p = \int_{-\infty}^{\infty} f_p(E)\rho_h(E)dE \tag{4.58}$$

$$f_n(E) = \frac{1}{1+\exp\left(\frac{E-F_n}{k_B T}\right)} \tag{4.59}$$

$$f_p(E) = \frac{1}{1+\exp\left(\frac{F_p-E}{k_B T}\right)} \tag{4.60}$$

A detailed description of how ATLAS handles Fermi-Dirac statistics is considered unnecessary here since the goal of reviewing these basic equations is to conceptually understand the physics considered in the software to better interpret the calculated results. However, further details regarding the computation of the quasi-Fermi levels using the Fermi-Dirac statistics are available in the ATLAS user's manual and involve expressions relying on the effective density of state values and the Fermi integral of order 1/2 [74]. These expressions ultimately relate the quasi-Fermi potentials to the carrier concentrations and are inserted into the current density equations (4.51) and (4.52) and into the continuity equations.

The continuity equations and Poisson's equation are solved by ATLAS applying the different recombination, mobility, and heterojunction models just outlined, and up to six coupled equations may need to be solved for the carrier concentrations and electrostatic potential. ATLAS has three basic solution techniques for solving these equations [74]. The first method is the Gummel

method that solves for each unknown while keeping the other variables constant and repeating the process until a stable solution is reached. The second method is the Newton method which solves the overall system of unknowns together, and finally the Block method solves some equations fully coupled and others decoupled. The default method is the Newton method, and it is the method used to solve the novel dual-wavelength laser structures. In solving the equations, ATLAS uses an initial guess of the variables from previous solutions and iterates to a converged solution at the new bias conditions, and small steps in the bias conditions converge easier in simulating a device. For the initial solution, the initial guesses are made from the doping profile, and the structure is solved for the zero bias or thermal equilibrium case.

To run ATLAS an input file is created which is then run in the ATLAS interface. In the first portion of the input file the device structure is specified which includes specifying the mesh size and density, defining regions and electrodes, and setting the doping levels of the defined regions. Next the materials of each region are selected and material parameters different than the default values can be set. The physical models to be applied in the simulation are then noted, and the numerical method can be set to one of the other two types if the default Newton method is not desired. Finally specifications for the solution files are made which include the bias conditions. The input file is then ran in ATLAS, and for each bias point, a structure file is generated which contains the solved variables at each node of the mesh. Parameters such as the band gap, band edges, carrier concentrations, electrostatic potential, electric field, current, quasi-Fermi

levels, recombination rates, *etc.* can be viewed for the different nodes of the mesh, and the values are extracted to generate figures such as the band diagrams shown in later chapters. Additionally log files can be specified which record these parameters at specific locations within the device/mesh as a function of the bias conditions. Besides current versus voltage curves, other curves such as recombination rate versus voltage or current can be generated for given points within the device. For example the quasi-Fermi levels of the different active regions are plotted as a function of the applied bias.

Additional parameters can be found using the resulting data from the ATLAS simulations, and an important parameter in evaluating the dual-wavelength structures is the injection efficiency of the different active regions or the fraction of the terminal current that generates carriers within an active region. The injection efficiency is easily found using the recombination rates within the active regions and with the following definition

$$\eta_i = \frac{qd_{\text{active}}(R_{\text{SRH, active}} + R_{\text{rad, active}} + R_{\text{Auger, active}})}{J_{\text{total}}}. \tag{4.61}$$

The injection efficiency of the different active regions can then be evaluated as a function of the applied bias or current.

A brief explanation of the band gaps and effective masses used in the ATLAS simulations is given as slight adjustments were made to these values to best represent the behavior of the quantum well active regions while preserving the relative simplicity of the modeling. Various quantum models are available in ATLAS, but these models are complex and limited in their scope and

documentation [74]. In these models detailed optimization procedures are required to determine proper values for several of the models' parameters to obtain useful simulation results. In simulating the novel dual-wavelength laser diodes, the most desired effect is a change in the density of states and the Fermi-Dirac statistics to reflect the quantum nature of the wells in the active regions. However to the best of our knowledge a simple method of achieving this without the additional complexity and limitations of the available quantum models is not available. To preserve the simplicity of the modeling, the quantum well active regions are thus considered as bulk materials in the ATLAS simulations in determining the density of states.

A few modifications are made however so these regions more closely resemble the effects of the quantum wells. The effective band gap value of the GaAs quantum well remains that of a bulk GaAs, and the band gap of the $In_{0.24}Ga_{0.76}As$ quantum well is set to the value of strained bulk $In_{0.24}Ga_{0.76}As$ on GaAs. These values are listed in Table IV.IV. Further, the values for the effective masses are set to those used in parabolic band models of quantum wells described in the literature and determined by the Luttinger parameters [67] and [68]. In the limit of a wide quantum well, the density of states approaches that of a bulk semiconductor, so this is considered as the best approximation to realizing the effects of the quantum well without relying on the full complex quantum models.

In parabolic models of the bands, the electron effective mass in a quantum well remains that of the bulk semiconductor, but the hole effective masses of the quantum well active regions are calculated using the Luttinger parameters of the

material. For an unstrained quantum well, the hole effective masses in the perpendicular and in-plane directions are equal and are calculated using the following relationships [67] and [78]:

$$m_{hh} = \frac{1}{\gamma_1 - 2\gamma_2} \tag{4.62}$$

$$m_{lh} = \frac{1}{\gamma_1 + 2\gamma_2}. \tag{4.63}$$

For a strained quantum well the perpendicular effective masses are unchanged from 4.62 and 4.63, but the in-plane effective masses are equal to

$$m_{hh} = \frac{1}{\gamma_1 + \gamma_2} \tag{4.64}$$

$$m_{lh} = \frac{1}{\gamma_1 - \gamma_2}. \tag{4.65}$$

For $In_xGa_{1-x}As$, the Luttinger parameters can be found by linear interpolating those of InAs and GaAs. The Luttinger parameters, calculated effective masses, and the band gaps used for the active regions in the ATLAS simulations are listed in Table IV.IV. In contrast, for the bulk GaAs regions the default values in ATLAS were used, and these values are also listed in the table for comparison. For the quantum well active regions, the in-plane heavy hole effective masses are used to determine the density of states since the degeneracy of the heavy and light hole bands is split inside the quantum well. For the bulk GaAs and $Al_xGa_{1-x}As$ regions the hole density of states effective mass is found from both the heavy and light

hole masses according to

$$m_h = (m_{lh}^{3/2} + m_{hh}^{3/2})^{2/3} \tag{4.66}$$

which is based on a three-dimensional density of states.

TABLE IV.IV
BAND PARAMETERS IN MODELING DWLD DESIGNS [74], [75], [78]

Parameter		GaAs QW	$In_{0.24}Ga_{0.76}As$ QW (strained)	GaAs bulk
Band gap	E_g (eV)	1.42	1.1742	1.42
Effective masses	m_e	0.063	0.0574	0.067
	m_{hh}	0.37	0.07	0.49
	m_{lh}	0.091	0.158	0.16
Luttinger parameters	γ_1	6.85	9.93	-
	γ_2	2.1	3.60	-

To complete this summary of the models and parameters used in the Silvaco ATLAS simulations the material parameters for $Al_xGa_{1-x}As$ are noted. For the graded $Al_xGa_{1-x}As$ regions within the dual-wavelength structures the band gap, effective masses, and dielectric constant are graded as follows and are default in ATLAS [74]:

$$E_g^{\Gamma} = 1.59 + 1.155x + 0.37x^2 \tag{4.67}$$

$$E_g^{X} = 1.911 + 0.005x + 0.245x^2 \tag{4.68}$$

$$\begin{aligned} m_e &= 0.067 + 0.083x \quad 0 < x < 0.45 \\ &= 0.85 - 0.14x \qquad x > 0.45 \end{aligned} \tag{4.69}$$

$$m_{lh} = 0.087 + 0.063x \tag{4.70}$$

$$m_{hh} = 0.62 + 0.14x \tag{4.71}$$

$$\varepsilon = 13.18 - 2.9x\,. \tag{4.72}$$

The mobility and recombination parameters are not graded in these regions, and instead the parameters of the intermediate composition x = 0.5 are used for the layers which are graded from x = 0.2-0.3 to x = 0.7-0.75.

IV. SUMMARY

With the modeling adjustments and methods covered in this chapter, different dual-wavelength device designs implementing the internal optical pumping scheme can be modeled and evaluated prior to the actual epitaxial growth. The balance of the low-level details with the general assumptions and simplifications was carefully monitored to allow the models to be as predictive as possible while maintaining simplicity and efficiency in the calculations and device development. Three different dual-wavelength designs are modeled in chapters six and seven using these modeling methods to calculate the optical modes and confinement factors, to apply the internal optical pumping model, and to evaluate the quasi-Fermi distributions and carrier dynamics.

5 Experimental Methods

To experimentally demonstrate dual-wavelength laser operation from the novel design, three generation of designs are studied in the next chapters, and this chapter covers the experimental techniques used in fabricating and testing actual devices based the on the internal optical pumping design. The epitaxial growth of the layers is done using molecular beam epitaxy (MBE). Standard broad-contact-area ridge-waveguide laser diodes are processed from the grown wafers using conventional semiconductor processing techniques. Laser bars are then cleaved at various cavity lengths, and to test the laser devices, a new testing station is designed and built with the flexibility to complete a variety of standard laser diode measurements. This chapter covers each of these areas, epitaxy growth, device processing, and device testing, in brief detail.

I. EPITAXY GROWTH

Epitaxial growth of the laser diode structures enables mono-layer growth of the dual-wavelength structures studied. The first generation of dual-wavelength laser diodes are grown at Arizona State University (ASU), using a VG V80H solid source MBE machine. The machine at ASU is capable of growing on 2” and 3” substrates, and the machine is equipped with Ga, Al, In, As, Sb, P, Be, Si, and Te sources. The second and third generation designs of the dual-wavelength laser diode are grown at the University of California, Los Angeles (UCLA). The MBE machine at UCLA is equipped with In, Ga, and Al effusion cells for the group III elements and As and Sb valved cracker cells for the group V elements. The

available dopant sources are Be, Si, and Te. The machines at both universities are equipped with reflection high energy electron diffraction systems for in-situ monitoring of the growth.

The complete details of the device structure are not given at this point but some specifics regarding the growths of the active regions and cladding materials are mentioned. The dual-wavelength laser structures are based on a graded index separate confinement heterostructure (GRINSCH), design using the GaAs/InGaAs/AlGaAs material system. In all the designs, a thick *n*-doped GaAs buffer layer is grown first on a 3" GaAs *n*-doped ($n \sim 1\times10^{18}$ cm^{-3}), substrate. Following the buffer layer, the *n*-doped region of the diode is grown which includes a high-Al-composition AlGaAs cladding layer with linear grades in the Al composition as the structure growth transitions from the GaAs buffer layer to the cladding and from the cladding to the core of the waveguide structure. The core of the waveguide is undoped in the region of the master active region, and after the growth of the core, a cladding *p*-doped region symmetric to the other cladding layers is grown. A highly doped *p*++ GaAs contact layer is the final epitaxial layer in all of the samples grown.

The growth temperature of the *n*-doped GaAs buffer layer in all samples is 580 °C, but the growth temperature of the AlGaAs cladding layers is different between the first generation samples grown at ASU and the later generation designs grown at UCLA. For the first generation design, the $Al_{0.75}Ga_{0.25}As$ cladding layers were grown at 670 °C using Sb surfactant. In the second and third generation designs, the $Al_{0.7}Ga_{0.3}As$ cladding layers are grown at 580 °C without

Sb surfactant. The change is based both on the need to grow the lower-temperature InGaAs slave active layer within the waveguide cladding in the later generation designs and UCLA's inexperience in using Sb as a surfactant in AlGaAs growth.

The active regions of the master and slave lasers as noted in chapter three are a GaAs multiple-quantum-well (MQW), region and an InGaAs single quantum well respectively. In all of the designs, the quantum well widths of the master active region are 10 nm. The composition of the well barriers is $Al_{0.2}Ga_{0.8}As$, and the barrier widths are 10 nm in the first design and 3 nm in the second and third designs of the dual-wavelength laser with the reduction expected to result in slightly lower thresholds. The calculated energy levels of the GaAs MQW are listed in Table V.I, and the transition wavelength at 300 K is 851 nm. The growth conditions of the GaAs MQW are the same as the AlGaAs cladding layers for the different designs, 670 °C with Sb surfactant for the first generation and 580 °C without surfactant for the later designs.

The slave laser active layer in the first generation design and in the modeling of all the designs is a 10 nm $In_{0.24}Ga_{0.76}As$ quantum well. The composition and well width in the grown second and third generation designs were adjusted to $In_{0.2}Ga_{0.8}As$ and 8 nm to improve the growth quality with UCLA's MBE. The energy levels and target wavelengths of these two quantum wells are listed in Table V.I. The last-minute change in the slave laser active layer should not result in a large deviation from the predicted modeling results with the wavelength difference being the most drastic. The growth temperature of the

InGaAs quantum wells is between 500-510 °C for all of three designs of the dual-wavelength laser diode. A complete list of all of the epitaxial layers in the designs is found in the next chapters with their specific modeling and experimental results.

TABLE V.I
QUANTIZED ENERGY LEVELS AND TRANSITION WAVELENGTHS OF ACTIVE REGION QUANTUM WELLS IN DWLD

Parameter		Master laser active layer	Slave laser active layer 1st gen. design	Slave laser active layer 2nd & 3rd gen. designs
Well material		GaAs	$In_{0.24}Ga_{0.76}As$	$In_{0.2}Ga_{0.8}As$
Well width		10 nm	10 nm	8 nm
Barrier		$Al_{0.2}Ga_{0.8}As$	GaAs	GaAs
E_g	(eV)	1.4240	1.1776	1.2179
E_{e2}	(eV)	0.1038	0.1017	-
E_{e1}	(eV)	0.0273	0.0286	0.0338
E_{hh1}	(eV)	-0.0053	-0.0059	-0.0083
E_{hh2}	(eV)	-0.0211	-0.0233	-0.0326
E_{lh1}	(eV)	-0.0201	-0.0102	-0.0116
Transition energy ($E_g + E_{e1} + \|E_{hh1}\|$)	(eV)	1.4566	1.2121	1.2600
λ	(nm)	851 nm	1023 nm	984 nm

II. DEVICE PROCESSING

Broad-contact-area ridge-waveguide laser diodes were fabricated from the grown material using standard processing techniques. The first generation designs were fabricated at ASU in the Center for Solid State Electronics Research, and the

second and third generation designs were fabricated at the University of Arkansas. The process flows of the two different process runs are mostly the same with the only significant difference being wet etching instead of dry etching of the mesa that forms the ridge-waveguide.

The most important steps of the fabrication of the dual-wavelength semiconductor laser diodes are illustrated in Fig. 5.1, and more detail is provided in the text that follows. The first step in the fabrication is the photolithography step to define the pattern for etching the mesa that forms the *p*-contact area and the ridge-waveguide. The mesa widths range from 30 μm to 150 μm, and AZ4620 and AZ3312 positive photoresists are used in the first generation's and later generations' device fabrication respectively. The difference between the two resists is the thickness of the resists, but given the wide feature size of the mesas and the relative etch depth, the difference is irrelevant. Following the developer step, the samples and resist are hard baked at 100 – 110 °C.

The second critical step in the fabrication process is the etch-step of the mesa. This etch is necessary to remove the highly-doped *p*++ contact layer in the non-device regions and confine the current flow to the device region. This etch can either be done using an inductively coupled plasma dry etch with BlC_3 and Cl_2 or using a 1:8:40, H_2SO_4:H_2O_2:H_2O wet etch with an etch rate of ~0.9-1.0 μm/s. Fabrication of the first generation devices used the dry etch method, whereas the later generation designs used the wet etch. The method of etching is not critical since the ratio of the etch depth is small compared to the mesa widths.

Following cleaning and removal of the first layer photoresist, a second lithography step forms the pattern for the top metal contacts of the laser diodes. Instead of positive photoresist, AZ5214 image reversal resist is used in this step. The same photomask from the first lithography step is used again in this step, but the mask and features are shifted one period so the 30 μm stripe width is over the 50 μm mesa, etc. After the photoresist layer is developed and baked, an Au/Ti metal stack is deposited on the samples using e-beam metal evaporation. Just prior to putting the samples in the e-beam evaporator, any native oxide is removed using a brief 10 second 1:20, $NH_4OH:H_2O$ wet etch. The Au and Ti target metal layer thicknesses are 2000-3000 Å and 200 Å respectively, and the samples are afterwards immersed in acetone to remove the photoresist and lift-off the metal. The result is the neatly patterned metal contacts on top of the mesas as seen in Fig. 5.1.

At this point the processing on the top-side or epi-side of the wafers is nearly complete, and the next step is thinning of the back-side GaAs substrate. Thinner samples will produce cleaner cleaves and higher quality mirror facets when laser bars are cleaved from the finished samples. The samples are lapped using mechanical abrasion from a starting thickness of ~360 μm to a final target thickness of ~100 μm. The samples are mounted on a rotatable chuck and held in position against a large grooved plate that is rotating while slurry of micrometer-sized Al_2O_3 particles is fed to the plate.

The samples are cleaned thoroughly after the lapping, and the next step is a blanket Au/Ni/AuGe metal deposition covering the back-side of the wafers to

form the *n*-contact of the devices. Any native oxide is removed prior to loading the samples in the evaporator using again the 1:20, $NH_4OH:H_2O$ wet etch. The target layer thicknesses are slightly different between the samples fabricated at ASU and the University of Arkansas, but the difference is expected to have little impact on the end performance of the devices. The total target thickness of the *n*-contact metal stack is 3655 Å and 4250 Å for the different processing runs.

The final step before cleaving the samples into laser bars is rapid thermal annealing (RTA), of the samples. The RTA step helps form better ohmic contacts to the device and the rapid temperature ramp and short duration of the anneal portion are necessary to limit diffusion of the dopants within the device. The temperature ramp is ~30 seconds to 400 °C, and then the samples are annealed at 400 °C for another 30 seconds.

Finally, individual laser bars are cleaved from the samples using a cleaving station designed and assembled at ASU. The station consists of a vacuum chuck mounted on rotational and translational stages. Above the chuck is a diamond-tipped scribe on a lever that is in a fixed position. Using the stages and the scribe, small marks to define the cleave planes can be scribed into the edge of a sample at selected intervals. The resolution of one of the micrometer-driven translational stages is on the order of a single micron, enabling great accuracy in cleaving laser bars with specific cavity lengths. The individual laser diodes on a laser bar are then ready for testing.

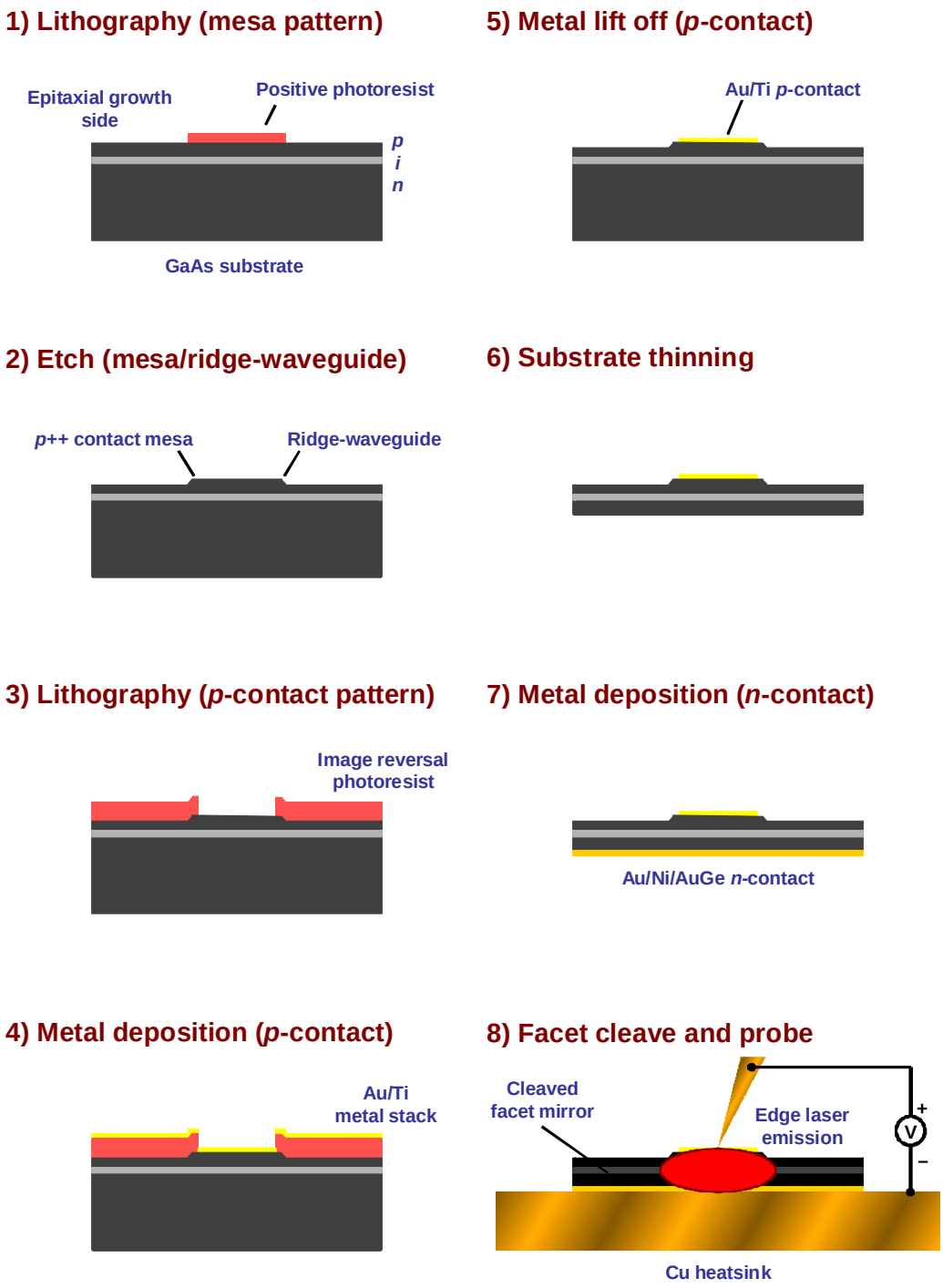

Fig. 5.1. Process flow diagram showing the critical steps in fabrication of the dual-wavelength laser diodes.

III. DEVICE TESTING

To test the dual-wavelength laser diodes, a new experimental setup was designed and built to perform standard spectrum and power vs. current (L-I), measurements. The setup was assembled in the high-speed lab of the ASU MBE Optoelectronics Group, and Fig. 5.2 is a photograph of the setup showing all the major components which include a probe station with a microscope and television monitor to probe individual devices, a pulsed current-source, an oscilloscope to monitor the current waveform, a thermal-electric cooler with a feedback system for controlling the temperature of the heatsink, optics and fibers to collect and direct the light output, an optical spectrum analyzer, and an optical multimeter for power and wavelength measurements. The testing setup was designed to allow flexibility in rearranging the components to do different types of measurements. The different setup configurations and the components of the system with their relevant specifications are outlined here.

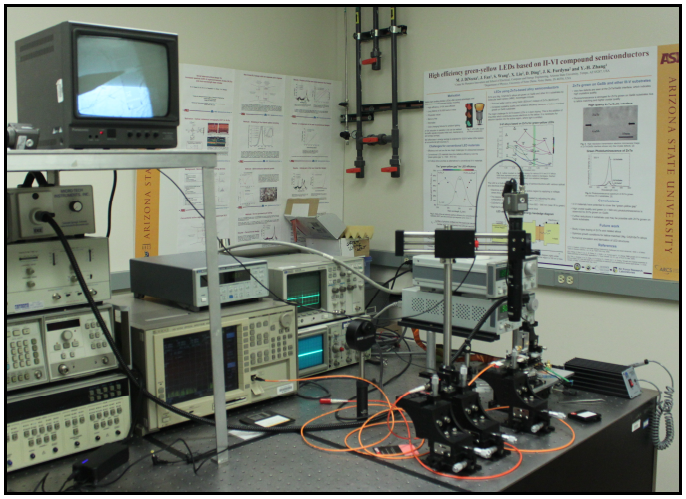

Fig. 5.2. Photograph of the equipment and setup built to test laser diodes at Arizona State University.

To probe the individual devices on a cleaved laser bar, the laser bar is placed on a Cu heatsink which is temperature controlled using a thermal electric cooler and an ILX Temperature Controller. The heatsink also functions as the negative terminal since it contacts the back-side metal and cathode of the diode. The top-side anode of the diode is contacted using a three-axis micrometer stage to position a probe tip on the metal contact as in Fig. 5.3. Initially W-probe tips were selected, but were replaced with BeCu-probe tips to lower the contact resistance with the Au contacts of the devices. The probe tips are shortened and soldered to a ceramic blade with a metal microstrip line leading to a SMA coaxial connector at the opposite end. The stage and probe tip are shown in the photograph of Fig. 5.4. A short coaxial cable connects the blade to a PCB board provided by ILX with an impedance-matching circuit to match the 50 ohm impedance cable ribbon from the current pulse driver to the laser diode device.

The design seeks to achieve impedance matching to maintain the bandwidth and current waveform from the current source to the PCB-matching board to the probed device. One output from the matching board enables monitoring of the waveform using an oscilloscope. The current source used is an ILX LDP-3840 precision pulsed current source with an output range of 20-3000 mA and 1 mA resolution. The source can produce current pulse widths from 0.1 μs to 10 μs with 0.1 μs resolution, and the range of pulse repetition intervals (PRI), is 0.001 ms to 6.5 ms.

The assembly of the heatsink and 3-axis stage with the BeCu probe is mounted to translational and rotational stages (seen in Fig. 5.4), for alignment of the probed laser diode with an optics system to collect and direct the emission from the facet of the device to the optical test equipment. The optics system is built on a series of three-axis stages directly in line with the probe assembly. On these stages different optical configurations can be assembled relatively quick based on the desired measurement, allowing multiple types of measurements to be conducted within a relative short time for a single probed device. Three of the possible configurations are shown in the diagram of Fig. 5.5.

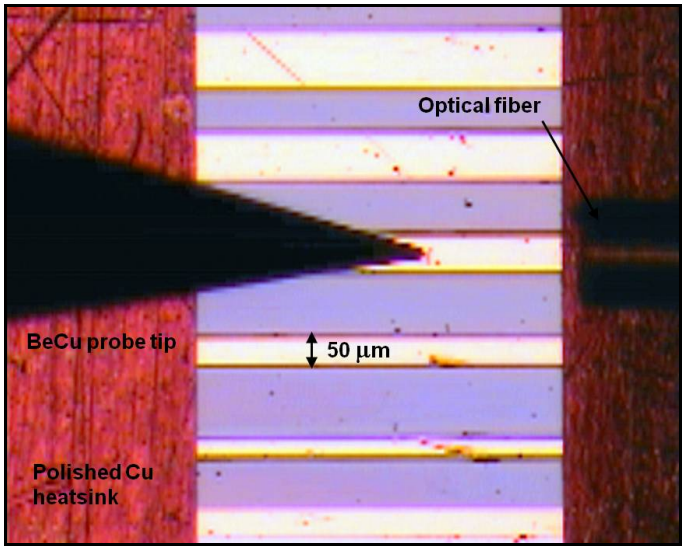

Fig. 5.3. Microscope view of the BeCu probe tip contacting the p-contact of the diode and the optical fiber butt-coupled to the facet of the laser diode. The laser bar sits on a polished Cu heatsink that also serves as the n-terminal.

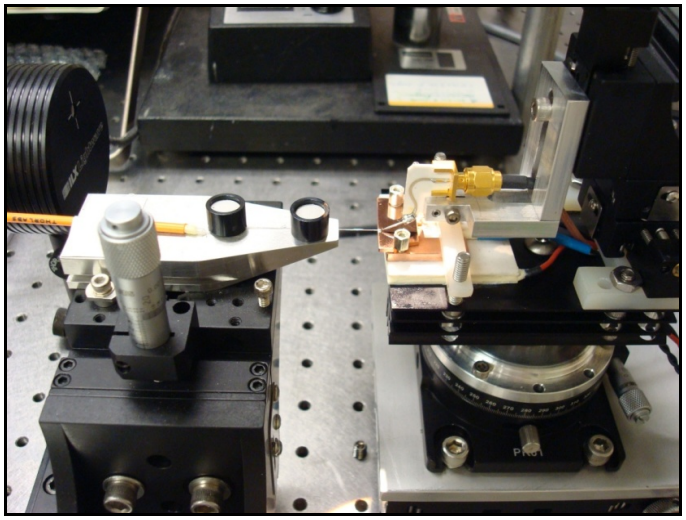

Fig. 5.4. Photograph of the laser diode testing setup in a butt-coupling fiber configuration. The micrometer stage on the left positions the fiber next to the facet of laser diode. The stage-on-stage assembly on the left positions the current probe tip on device while allowing alignment of the device with the optics.

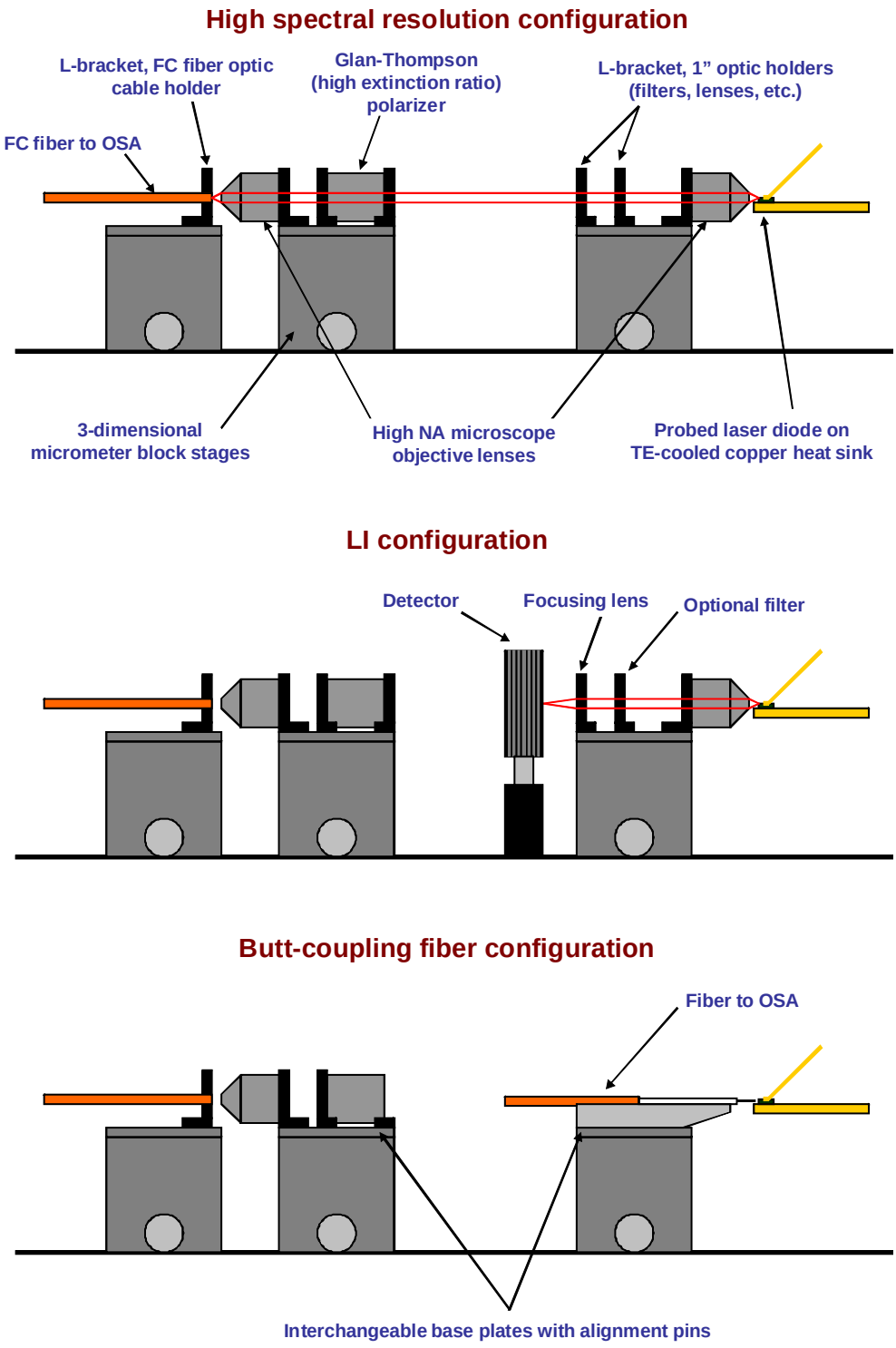

Fig. 5.5. Three of the different configurations of the interchangeable laser diode testing station designed and assembled for testing the DWLD.

Spectrum measurements of the edge emission from the probed device can be done in two ways. The first method is a butt-coupling method where an optical fiber is positioned using the micrometer controls of one of the three-axis stages until it is nearly adjoining the laser diode at the facet edge as seen in Fig. 5.3 and Fig. 5.5. The opposite end of the fiber is connected to an Ando optical spectrum analyzer, and nearly all of the spectrum measurements reported in this study are performed using this technique because of its ease of alignment with good collection efficiency. Another configuration of the setup is to first collimate the laser light with a large numerical aperture lens, and then the beam can pass through any desired optical components before focusing and coupling the beam into the fiber using another lens. This is the configuration used in the high spectral resolution configuration shown in Fig. 5.5. In this setup the beam passes through a Glan-Thompson polarizer with a high extinction coefficient to separate the polarized amplified spontaneous emission and laser modes from the spontaneous emission. The high resolution spectrum of a conventional InGaAs quantum well laser diode shown in Fig. 5.6 and Fig. 5.7 are collected using this configuration and were done as part of qualifying the test setup.

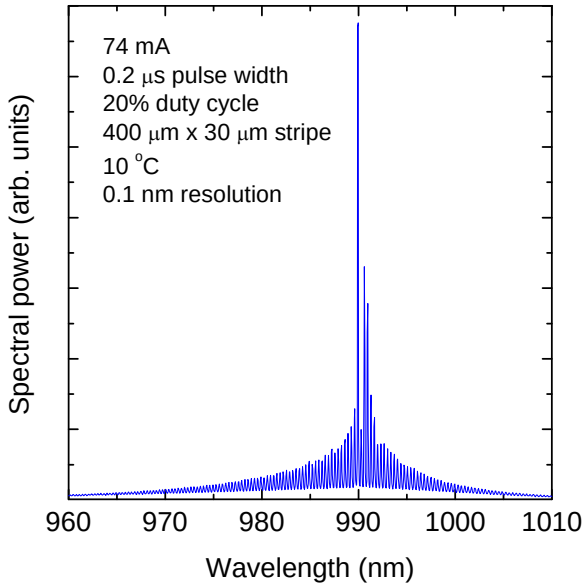

Fig. 5.6. High-resolution spectrum of a conventional InGaAs quantum well laser diode just above laser threshold measured by the assembled testing setup.

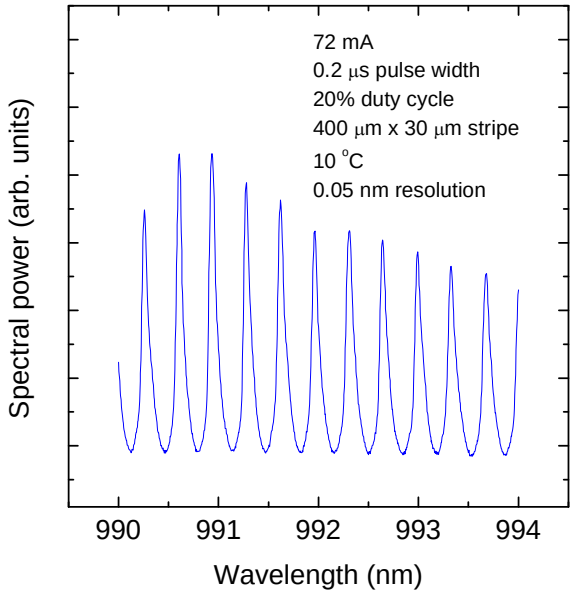

Fig. 5.7. High-resolution spectrum of a conventional InGaAs quantum well laser diode just below laser threshold showing amplified spontaneous emission modes.

Power versus current measurements are done using an ILX OMM-6810B Optical Multimeter with either a OMH-6722B Silicon Power/WaveHead or OMH-6727B InGaAs Power/WaveHead to measure the output power and wavelength of the laser emission. Both detectors are a type of integrating sphere, and the input power range of both detectors is 100 nW to 1 W. The silicon-detector power/wavelength meter has a specified wavelength range 400 nm to 1100 nm, and InGaAs-detector range is 950 nm to 1650 nm. The detector can be placed immediately in front of the laser diode for maximum power coupling. To generate L-I curves of the master and slave lasers of the dual-wavelength laser diode, a high numerical aperture lens is used to collimate the laser emission, and then a 900 nm short or long pass filters is used to select only the 850 nm or 1020 nm laser wavelengths before a final lens focuses the beam back into the detector as in the L-I configuration in Fig. 5.5.

6 First Generation Device Design

A first generation design of the dual-wavelength laser diode structure was developed and grown using the MBE machine at Arizona State University prior to the full development of the internal optical pumping theory discussed in chapter three. The goal of the design was to decouple the quasi-Fermi levels and carrier distributions between the master and slave active regions and implement the internal optical pumping scheme; however, due to a limited window of time to do the epitaxial growth, the first generation design had to be designed quickly as a gross reality check without a extensive modeling or understanding of the internal optical pumping theory. In this chapter, the experimental results of the first generation devices are presented along with an analysis of the design using the modeling methods covered in chapter four.

I. DESIGN

To study the first generation design, two different structures were designed for comparative study. One design, referred to as the "control" design, consists of two sets of asymmetric wells both within the intrinsic region of the *p-i-n* junction and the core of the heterostructure waveguide. The design is illustrated in Fig. 6.1, which also shows the profile of the calculated optical mode of the inherent waveguide. The first set of quantum wells is three 10 nm GaAs wells with 10 nm $Al_{0.2}Ga_{0.8}As$ barriers, and the second set is a single 10 nm $In_{0.24}Ga_{0.76}As$ quantum well with GaAs buffer barriers. The different layers with their thickness, composition, and applicable dopings are listed in Table VI.I.

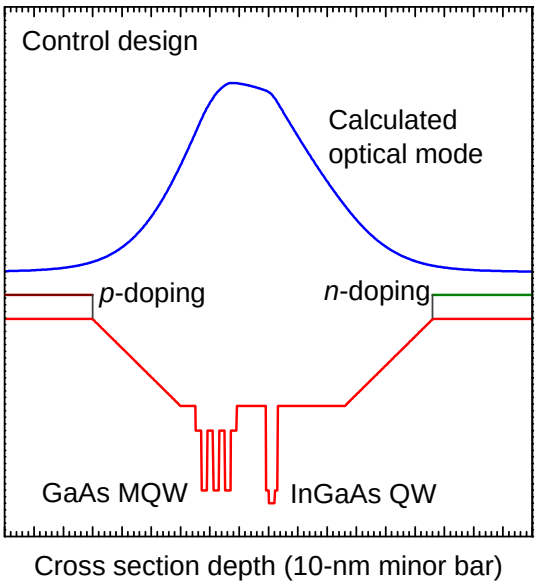

Fig. 6.1. Control design of a laser diode with asymmetric quantum wells showing the active and doped regions and the calculated optical mode profile.

TABLE VI.I
CONTROL LASER DIODE EPITAXIAL LAYERS / DESIGN

Description	Material	Layer thickness (nm)	Dopant concentration (cm^{-3})
p++ contact	GaAs	100	Be – Graded: 3×10^{19} to 1×10^{18}
Cladding	Graded: $Al_{0.06}Ga_{0.94}As$ to $Al_{0.75}Ga_{0.25}As$	200	Be – 1×10^{18}
Cladding	$Al_{0.75}Ga_{0.25}As$	1200	Be – 1×10^{18}
Cladding	Graded: $Al_{0.75}Ga_{0.25}As$ to $Al_{0.3}Ga_{0.7}As$	150	
	$Al_{0.3}Ga_{0.7}As$	25	
	$Al_{0.2}Ga_{0.8}As$	10	
Active QW	GaAs	10	
	$Al_{0.2}Ga_{0.8}As$	10	
Active QW	GaAs	10	
	$Al_{0.2}Ga_{0.8}As$	10	
Active QW	GaAs	10	
	$Al_{0.2}Ga_{0.8}As$	10	
	$Al_{0.3}Ga_{0.7}As$	50	
	GaAs	5	
Active QW	$In_{0.24}Ga_{0.76}As$	10	
	GaAs	5	
	$Al_{0.3}Ga_{0.7}As$	115	
Cladding	Graded: $Al_{0.3}Ga_{0.7}As$ to $Al_{0.75}Ga_{0.25}As$	150	
Cladding	$Al_{0.75}Ga_{0.25}As$	1200	Si – 1×10^{18}
Cladding	Graded: $Al_{0.75}Ga_{0.25}As$ to $Al_{0.06}Ga_{0.94}As$	200	Si – Graded: 1×10^{18} to 5×10^{17}
Buffer	GaAs	400	Si – 5×10^{17}

The other design is the first generation dual-wavelength laser design and utilizes the same sets of quantum wells as the conventional design. However, the center-to-center pitch of the active regions is increased from 95 nm in the control design to 170 nm in the first generation dual-wavelength design. Additionally, the silicon *n*-type doping is extended into the core of the waveguide 105 nm beyond the slave $In_{0.24}Ga_{0.76}As$ quantum well so it is within the *n*-doped region of the junction. The first generation design is shown in Fig 6.2 with its calculated optical mode, and the details of the epitaxial layers are listed in Table V.II.

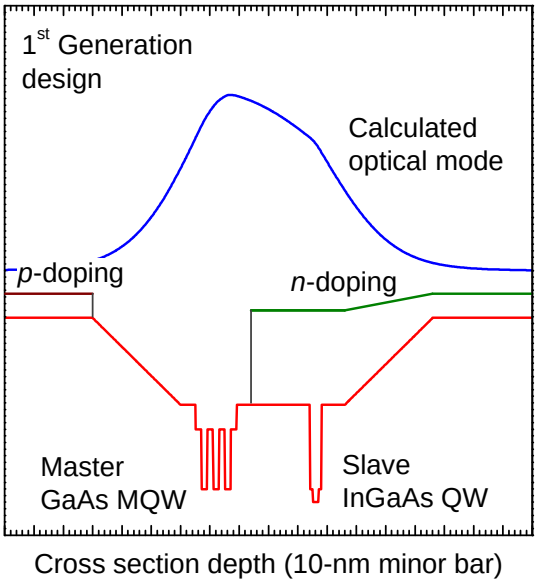

Fig. 6.2. First generation design of the dual-wavelength laser design with its active and doped regions and optical mode profile.

TABLE VI.II
FIRST GENERATION DWLD EPITAXIAL LAYERS / DESIGN

Description	Material	Layer thickness (nm)	Dopant concentration (cm^{-3})
p++ contact	GaAs	100	Be – Graded: 3×10^{19} to 1×10^{18}
Cladding	Graded: $Al_{0.06}Ga_{0.94}As$ to $Al_{0.75}Ga_{0.25}As$	200	Be – 1×10^{18}
Cladding	$Al_{0.75}Ga_{0.25}As$	1200	Be – 1×10^{18}
Cladding	Graded: $Al_{0.75}Ga_{0.25}As$ to $Al_{0.3}Ga_{0.7}As$	150	
	$Al_{0.3}Ga_{0.7}As$	25	
	$Al_{0.2}Ga_{0.8}As$	10	
Master QW	GaAs	10	
	$Al_{0.2}Ga_{0.8}As$	10	
Master QW	GaAs	10	
	$Al_{0.2}Ga_{0.8}As$	10	
Master QW	GaAs	10	
	$Al_{0.2}Ga_{0.8}As$	10	
	$Al_{0.3}Ga_{0.7}As$	25	
	$Al_{0.3}Ga_{0.7}As$	100	Si – 5×10^{17}
	GaAs	5	Si – 5×10^{17}
Slave QW	$In_{0.24}Ga_{0.76}As$	10	Si – 5×10^{17}
	GaAs	5	Si – 5×10^{17}
	$Al_{0.3}Ga_{0.7}As$	40	Si – 5×10^{17}
Cladding	Graded: $Al_{0.3}Ga_{0.7}As$ to $Al_{0.75}Ga_{0.25}As$	150	Si – Graded: 5×10^{17} to 1×10^{18}
Cladding	$Al_{0.75}Ga_{0.25}As$	1200	Si – 1×10^{18}
Cladding	Graded: $Al_{0.75}Ga_{0.25}As$ to $Al_{0.06}Ga_{0.94}As$	200	Si – Graded: 1×10^{18} to 5×10^{17}
Buffer	GaAs	400	Si – 5×10^{17}

In the control design, the two sets of asymmetric quantum wells are expected to share common quasi-Fermi levels and carrier distributions due to carrier scattering and thermal equilibration between the wells as illustrated in Fig. 6.3 (reproduced from earlier). In this structure, much larger carrier densities should exist within the longer wavelength $In_{0.24}Ga_{0.76}As$ quantum well which in turn would result in the threshold gain being reached before the GaAs quantum well transitions and laser emission would occur solely at 1020 nm.

Different behavior was predicted from the first generation design of the dual-wavelength laser as it was expected the extension of the doping and the larger spatial separation between the wells would in effect position the longer wavelength slave quantum well outside the junction and produce the necessary decoupling of the quasi-Fermi distributions. The device was then expected to function according to the theory presented in the earlier chapters and illustrated in Fig. 6.4 where the master GaAs multiple-quantum-well laser would reach threshold first at 850 nm and optically-pump the $In_{0.24}Ga_{0.76}As$ quantum well to its laser threshold. Simultaneous laser emission at 850 nm and 1020 nm was the predicted experimental result.

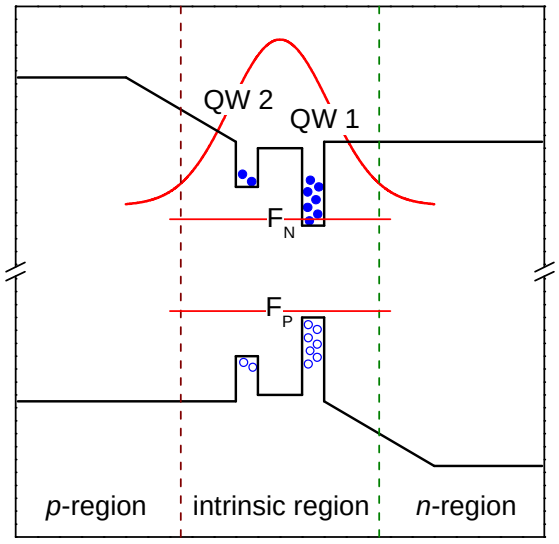

Conventional MQW laser diode band diagram

Fig. 6.3. Conventional or control laser diode design with asymmetric quantum wells that share quasi-Fermi levels and distributions, resulting in larger carrier populations in the longer wavelength well.

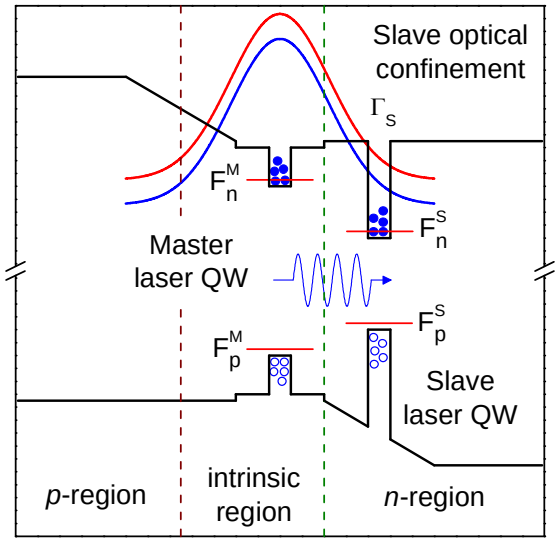

Novel internal-optically-pumped DWLD band diagram

Fig. 6.4. The concept of the novel internal-optically-pumped dual-wavelength laser diode with separate quasi-Fermi levels and distributions for the two active regions and reliance on the internal optical pumping.

II. EXPERIMENTAL RESULTS

The control and first generation dual-wavelength designs were grown using MBE, and broad area contact laser devices were processed according to the methods discussed in chapter five. Individual devices were probed, and spectra measurements and power-current (L-I) curves were measured at the cleaved facets of the device according to the methods discussed earlier. All of the control and first generation devices tested and reported here have 30 μm contact widths.

In observing the spectra of the control laser devices, the predicted behavior of single-wavelength laser output is confirmed, and Fig. 6.5 shows the spectra of a 430 μm long device at increasing currents above threshold. The laser threshold of the 1020 nm $In_{0.24}Ga_{0.76}As$ quantum well is much larger than the best single quantum well lasers due to poorer injection efficiency of the terminal current in generating carriers inside the quantum well. This is due to the addition of the multiple GaAs quantum wells as well as non-optimized doping of the graded cladding layers and the short cavity of the device. The device exhibits single-wavelength behavior as no emission is observed from the 850 nm GaAs quantum wells until over five times the current threshold of the 1020 nm quantum well. With large injection, minimal spontaneous emission is observed at 850 nm; however, it is rather insignificant in comparison to the stimulated emission from the $In_{0.24}Ga_{0.76}As$ quantum well, and the overall results are very indicative of shared quasi-Fermi levels and distributions for the two active regions.

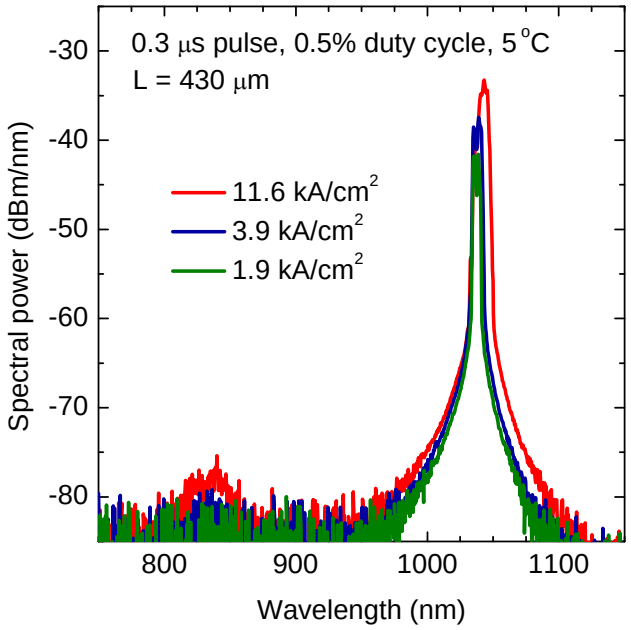

Fig. 6.5. Electroluminesence spectra of the control laser diode showing single-wavelength behavior as expected at the longer wavelength.

Much different behavior was observed from the first generation dual-wavelength design devices, although not the behavior predicted in the early design stage. The spectra of a first generation dual-wavelength device at different levels of current injection are shown in Fig. 6.6. In contrast to the conventional devices, greater emission is observed from the GaAs multi-quantum well active region. However, the emission of the longer wavelength 1020 nm $In_{0.24}Ga_{0.76}As$ quantum well is still stronger, and the slave laser reaches threshold first contrary to the predicted performance. The threshold for the longer wavelength slave laser is even larger than the control design since the active region is no longer in the intrinsic junction region of the diode.

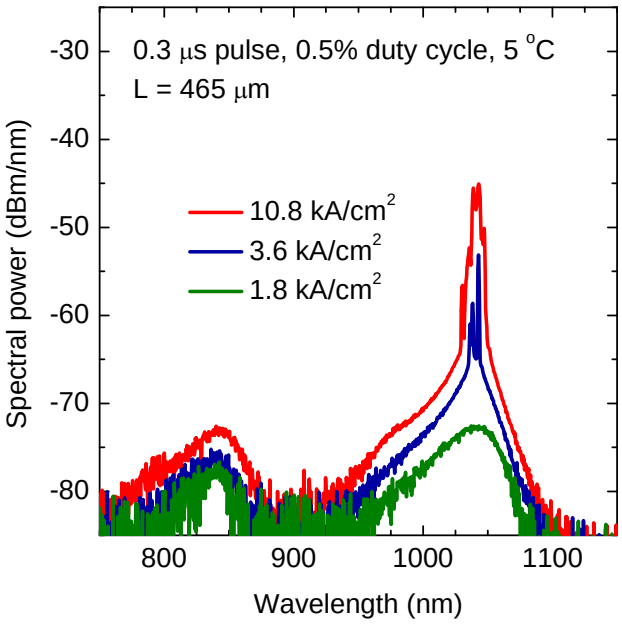

Fig. 6.6. Electroluminesence spectra of the first generation dual-wavelength laser diode where the longer wavelength quantum well reaches threshold first.

Even though the master shorter wavelength active region does not reach threshold first to optically pump the longer wavelength slave region in the first generation design, at extremely high injection levels, multi-wavelength laser emission is still observed with the on-set of laser emission from the master GaAs quantum wells as the terminal current is increased. The multi-wavelength output shown in Fig. 6.7 and Fig. 6.8 is only observed in short cavity devices and at high injection levels. Interestingly at such high injection and a certain cavity length, laser output is observed from multiple transitions within the $In_{0.24}Ga_{0.76}As$ quantum well due to thermal effects. Time-resolved measurements are necessary to determine if the transitions are lasing simultaneously or if they are pulsating such that the spectrum analyzer cannot resolve it temporally. However, one possibility is the high injection introduces thermal effects which increase the

threshold condition and introduce an incomplete pinning of the quasi-Fermi levels and carrier distributions in the $In_{0.24}Ga_{0.76}As$ quantum well. Eventually the gain would be large enough to support laser output at both the e1-hh1 transition and the e2-hh2 transition which are 1023 nm and 948 nm respectively at 300 K. The laser peaks are then red-shifted in Fig. 6.7 and Fig 6.8. due to the thermal effects at the high injection-levels. If the cavity length is made shorter so that the mirror loss and threshold are higher, laser emission from the $In_{0.24}Ga_{0.76}As$ quantum well is only observed from the higher energy e2-hh2 transition due to band-filling and satisfying the increased gain threshold conditions. To confirm the multi-wavlength laser output, L-I measurements were done on a 200 μm cavity device using 900 nm short- and long-pass filters, and the curves shown in Fig. 6.9 indicate laser output from the two active regions but only at extremely high thresholds.

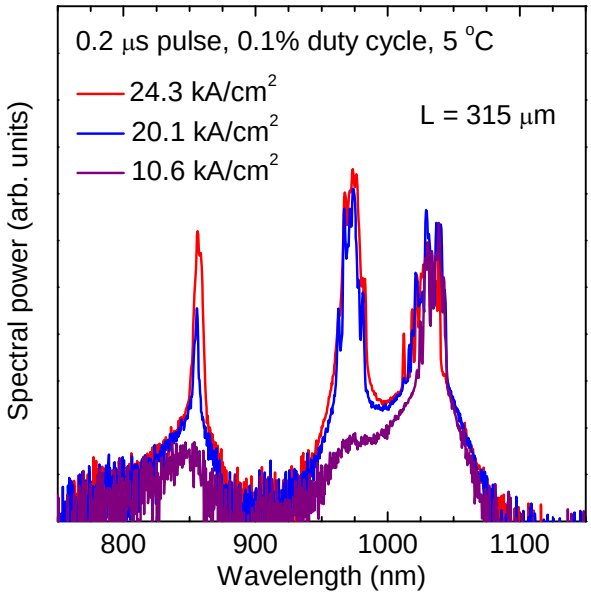

Fig. 6.7. Electroluminesence spectra of a short-cavity first generation dual-wavelength laser diode at extremely high injection showing multi-wavelength laser output.

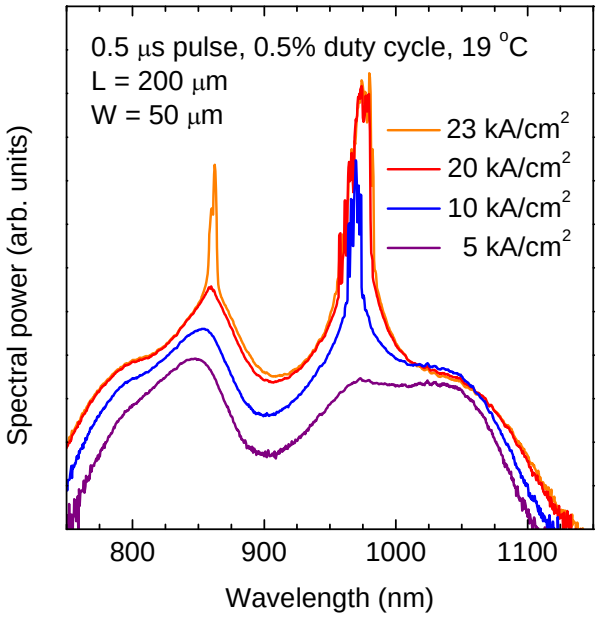

Fig. 6.8. Electroluminesence spectra of a short-cavity first generation dual-wavelength laser diode at extremely high injection showing dual-wavelength laser output.

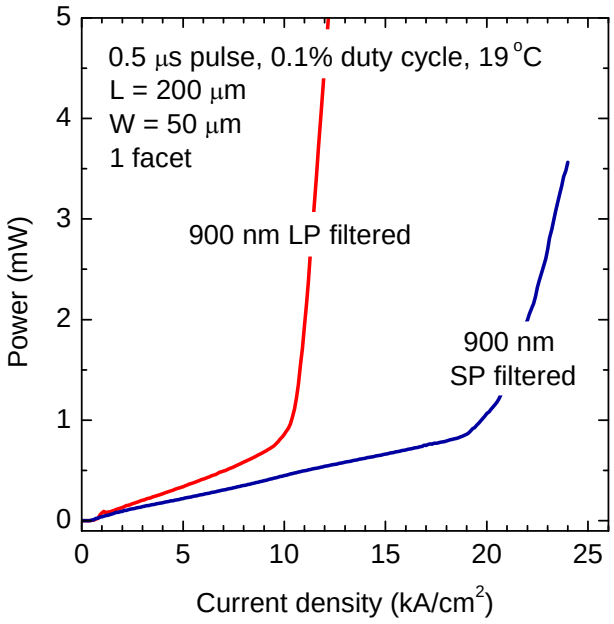

Fig. 6.9. Power vs. current density of a short-cavity first generation dual-wavelength laser diode at extremely high injection showing dual-wavelength laser output.

Despite the multi-wavelength laser output from the first generation design, the design is not considered a successful dual-wavelength design due to the extremely high-thresholds, the need for short-cavity devices, and that the slave laser reached threshold first. Given the slave laser reached threshold first, it is assumed very little of the carrier generation in the slave $In_{0.24}Ga_{0.76}As$ quantum well is due to optical pumping from the master GaAs quantum wells. The course of the research at this point transitioned to developing the internal optical pumping theory in chapter three, and developing device models to better understand and trouble-shoot the first generation design, the results of which will be covered next.

III. MODELING RESULTS

In order to better understand the surprising experimental results and performance of the first generation dual-wavelength laser design, predictive modeling of the design is performed using the Silvaco software and the parameters outlined in chapter four. The first generation design was modeled to understand the carrier dynamics within the device sub-laser-threshold and without any internal optical pumping. From the modeling, the calculated band diagram of the device under a voltage bias of 1.45 V is shown in Fig. 6.10. The voltage bias was chosen to match the quasi-Fermi level separation necessary to reach transparency in the master active region. The band diagram shows the quasi-Fermi level separation in the master multi-quantum well region and the slave single quantum well region are not equal, supporting the design's original specification to decouple the quasi-Fermi levels. To understand the degree to which the master and slave active regions are isolated from each other electronically, the quasi-Fermi level separation in the regions as a function of the terminal voltage bias is calculated and plotted in Fig. 6.11. According to these results, the slave region reaches the necessary quasi-Fermi level separation indicative of transparency at a lower voltage bias than the master region. These results suggest a decent portion of the terminal current is still generating carriers in the slave active region quantum well since the model does not include optical pumping, a valid simplification of the model since the master laser still has not met laser threshold conditions.

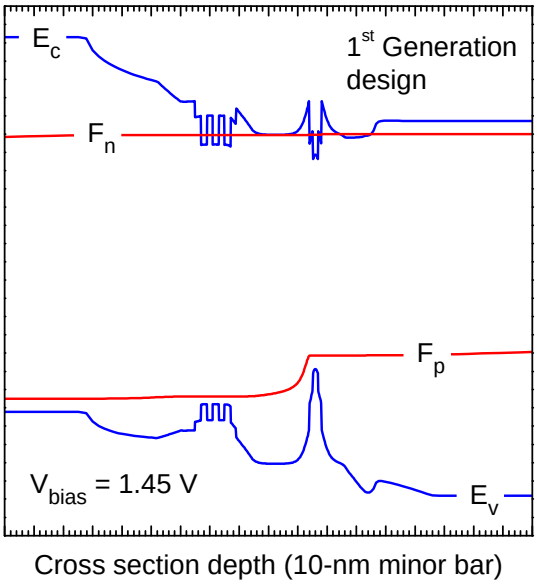

Fig. 6.10. Calculated band diagram of the first generation dual-wavelength laser design with an applied voltage bias of 1.45 V.

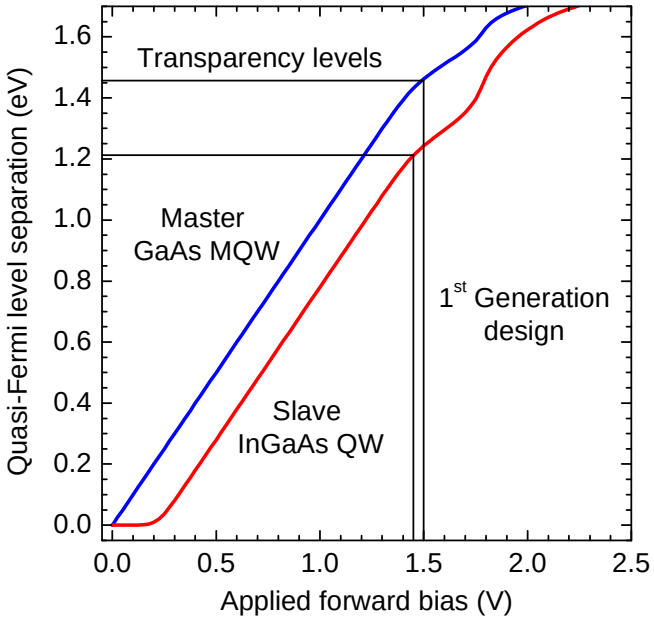

Fig. 6.11. Calculated quasi-Fermi level separation in the active regions as a function of applied bias for the first generation dual-wavelength laser design.

Since the modeling suggests a portion of the current is generating carriers in the slave active region, intermediate results of the Silvaco modeling are used to determine the exact portion of the current going to the slave region compared to the portion going to the master active region. Among the different computed parameters of the modeling are the SRH, radiative, and Auger recombination rates in the quantum well active regions. The sum of these rates or the total recombination rate in a quantum well leads to the amount of current generating carriers and recombining within the quantum well as was shown in chapter four. With this active region current, the injection efficiency η_i or portion of the terminal current that generates carriers in the active region can be determined.

The sub-threshold injection efficiencies of the master and slave laser active regions in the first generation design, determined by the model, are plotted as a function of the terminal current density in Fig. 6.12. Initially at a few hundred A/cm^2, approximately 85% of the current is recombining in the master active region, and only about 5% is leaking into the slave region. However, as the current density is increased to 2000 A/cm^2, the injection efficiency or amount of current leaking to the slave region increases to 20% and the master region drops to near 60%. Since the master region consists of three quantum wells and the slave only one, the portion of the current recombining in each of the wells is nearly equal. The current leakage into the slave active region becomes quite significant beyond a few hundred A/cm^2.

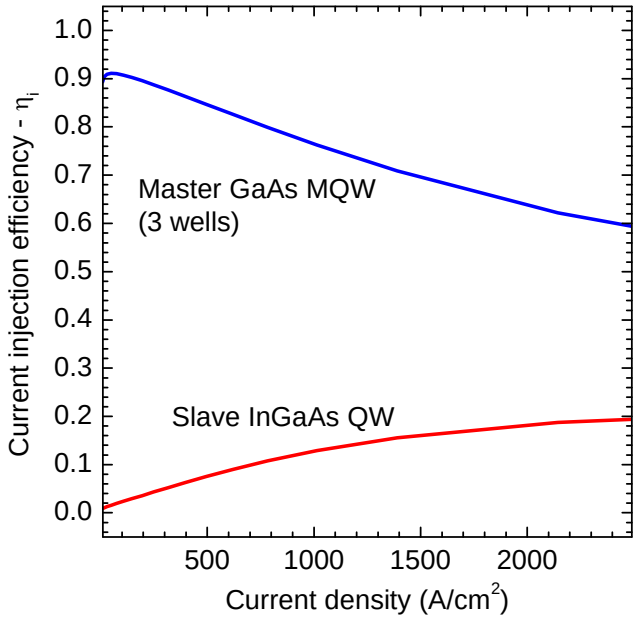

Fig. 6.12. Calculated current injection efficiency vs. applied current density for the master and slave laser active regions in the first generation dual-wavelength laser design.

Good quantum well laser diodes have threshold current densities in the low hundreds of A/cm^2. From the modeling, at this current level most of the current is recombining in the master region with only a small amout leaking to the slave, so other losses must be preventing the master laser from reaching threshold in the first generation design. After developing and applying the internal optical pumping model from chapter three, it was identified that the modal absorption loss introduced by the slave active region is too large in the first generation design and prevents the master laser from reaching threshold.

From the calculated optical mode, the optical confinement factors of the first generation design were determined and then used in the internal optical pumping model. With this design the optical confinement factor of the slave

quantum well with its GaAs buffer layers is 4.81%, which leads to a modal absorption loss contribution to the master laser threshold equation of 814 cm^{-1}. Even under the ideal assumption of 100% injection efficiency to the master active region, the threshold current density of the master laser according the logarithmic gain-current relation would be a hypothetical 500 kA/cm^2. Table VI.III lists some of the key parameters and results of the internal optical pumping model when applied to the first generation dual-wavelength laser diode design.

Combining the results from the Silvaco modeling and the internal optical pumping model, the current understanding of the first generation design is the master laser will never reach threshold first and produce the internal optical field to pump the slave laser active region because the modal absorption loss of the slave region is too large. Instead at a large enough current injection, the inefficient current leakage generates enough carriers in the slave active region to reach laser threshold, and with short cavity devices and extremely high injection levels, dual-wavelength laser output is observed but not due to internal optical pumping.

TABLE VI.III
PARAMETERS AND RESULTS OF INTERNAL OPTICAL PUMPING MODEL APPLIED TO FIRST GENERATION DWLD DESIGN

Component	Parameter	1st Gen. DWLD design
GaAs MQW master gain	Current injection eff. – η_i	1.0
	Number of wells – n_w	3
	Optical conf. – $\Gamma_{w,\,avg.}$ (%)	3.09
InGaAs slave absorption	Optical conf. – Γ_S (%)	2.41
	Modal absorption in QW (cm^{-1})	596.9
	Optical conf. – Γ_b (%)	2.40
	Modal absorption in GaAs barrier (cm^{-1})	217.1
	Total abs. loss (cm^{-1})	814.1
Cavity losses (850 nm)	Free carrier abs. (cm^{-1})	0.86
	Assumed intrinsic loss (cm^{-1})	10
	Mirror loss (cm^{-1})	12.04
Master laser threshold (A/cm^2)		500,120
InGaAs slave gain	Current injection eff. – η_i	0.0
	Optical conf. – Γ_S (%)	2.36
Cavity losses (1020 nm)	Free carrier abs. (cm^{-1})	0.99
	Assumed intrinsic loss (cm^{-1})	10
	Mirror loss (cm^{-1})	12.04
Slave laser threshold (A/cm^2)		500,220

IV. SUMMARY OF FIRST GENERATION DESIGN

The first generation design despite being designed prior to a complete development of the models was valuable as the experimental results helped direct development of the models outlined in chapter four. The design confirmed the

possibility of decoupling the quasi-Fermi levels and distributions of the master and slave laser active regions but that further improvements in the design are needed to limit the current leakage to the slave region. In addition, the results validated the critical conclusion from chapter three that the optical confinement factor of the slave active region and its buffer layers needs to be optimized to balance the modal absorption loss presented to the master laser with the modal gain needed by the slave laser. Based on these observations and using the developed models, additional new generations of dual-wavelength laser diode designs are explored in the next chapter.

7 Second and Third Generation Device Designs

The first generation dual-wavelength laser diode (DWLD), design did not produce the desired dual-wavelength laser output at reasonable thresholds, and whereas multi-wavelength laser output was observed, it was due to thermal effects at high injection rather than the sought internal optical pumping. It was determined from the modeling that the device's performance was due to carrier leakage into the slave active region and large modal absorption loss to the master laser due to the slave. Hence, second and third generation designs are developed that aim to lower the current leakage into the slave active region and optimize the optical confinement factor of the slave active region.

I. MODELING AND DESIGN OF THE SECOND GENERATION DESIGN

Heterostructures in conventional semiconductor laser diodes confine carriers to the active region of the device and thereby limit the current leakage. In the first generation dual-wavelength design an $Al_{0.3}Ga_{0.7}As$ barrier layer is positioned between the master GaAs multi-quantum well active region and the slave $In_{0.24}Ga_{0.76}As$ single quantum well active region to decouple the quasi-Fermi distributions. It was noted previously that the modeling reveals for a current density of a few hundred A/cm^2, approximately 5% of the terminal current leaks into the slave active region, and that by 2000 A/cm^2, the current injection into the slave quantum well is nearly equal the injection into any one of the master quantum wells. One possibility to reduce the current leakage overall into the slave region is to use a larger Al composition to increase the band gap and the

heterobarrier. Reducing the carrier leakage is therefore not considered difficult in implementing the dual-wavelength laser concept, and the challenge thus shifts to optimizing the optical confinement factors of the master and slave laser modes.

From the internal optical pumping theory, the optical confinement factor of the slave laser must be optimized. To review, if it is too large, the modal absorption loss the slave active region introduces prevents the master laser from reaching threshold, and if it is too small, the slave laser will not have enough modal gain to reach its threshold. For the active materials selected in this study, it was shown in chapter three that a multiple-quantum-well master region consisting of five quantum wells and a slave optical confinement factor of 0.69% result in the lowest thresholds for the master and slave lasers.

The optical confinement factors for different dual-wavelength designs are determined by calculating the optical modes of different GRINSCH waveguides using the calculation methods in chapter four. The Al composition, spatial dimensions, and location of the slave active region are varied in the different designs to determine a design that meets the criteria defined by the internal optical pumping model. Ideally the core of the waveguide should be thin to maintain adequate optical confinement of the master active region. Therefore, from the modeling, it is determined that to reach an optical confinement factor near 0.69%, the slave active region needs to be positioned outside the waveguide core but still within the tail of the guided optical mode. A second generation design of the dual-wavelength laser is developed with the required number of wells and optical confinement factors, and the design is shown in Fig. 7.1 with the calculated

optical mode. The specific composition, thickness, and doping of the different epitaxial layers of the second generation design are listed in Table VII.I.

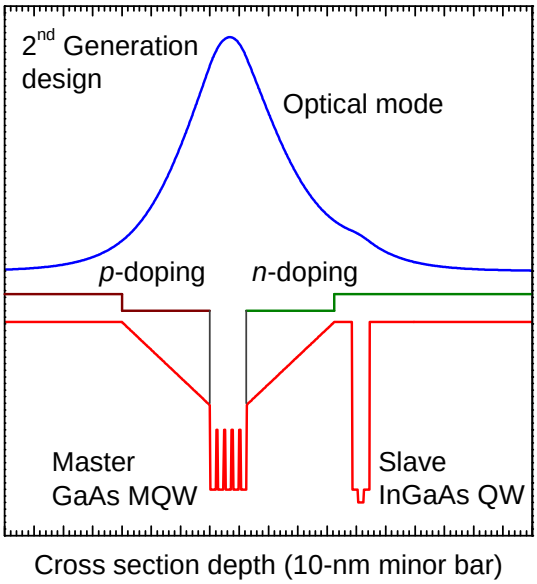

Fig. 7.1. Second generation design of the dual-wavelength laser with its doped and active regions where the slave active region is positioned outside the core of the waveguide to optimize the optical confinement.

TABLE VII.I
SECOND GENERATION DWLD EPITAXIAL LAYERS / DESIGN

Description	Material	Layer thickness (nm)	Dopant concentration (cm^{-3})
p++ contact	GaAs	125	Be – Graded: 1×10^{19} to 2×10^{18}
Cladding	Graded: $Al_{0.1}Ga_{0.9}As$ to $Al_{0.7}Ga_{0.3}As$	200	Be – 2×10^{18}
Cladding	$Al_{0.7}Ga_{0.3}As$	1500	Be – 2×10^{18}
Cladding	Graded: $Al_{0.7}Ga_{0.3}As$ to $Al_{0.3}Ga_{0.7}As$	150	Be – 1×10^{18}
Active QW	GaAs	10	
	$Al_{0.2}Ga_{0.8}As$	3	
Active QW	GaAs	10	
	$Al_{0.2}Ga_{0.8}As$	3	
Active QW	GaAs	10	
	$Al_{0.2}Ga_{0.8}As$	3	
Active QW	GaAs	10	
	$Al_{0.2}Ga_{0.8}As$	3	
Active QW	GaAs	10	
Cladding	Graded: $Al_{0.3}Ga_{0.7}As$ to $Al_{0.7}Ga_{0.3}As$	150	Si – 1×10^{18}
Cladding	$Al_{0.7}Ga_{0.3}As$	30	Si – 2×10^{18}
	GaAs	10	Si – 2×10^{18}
Active QW	$In_{0.2}Ga_{0.8}As$	8	Si – 2×10^{18}
	GaAs	10	Si – 2×10^{18}
Cladding	$Al_{0.7}Ga_{0.3}As$	1500	Si – 2×10^{18}
Cladding	Graded: $Al_{0.7}Ga_{0.3}As$ to $Al_{0.1}Ga_{0.9}As$	200	Si – 2×10^{18}
Buffer	GaAs	400	Si – 2×10^{18}

The sub-threshold carrier dynamics of the second generation dual-wavelength laser design are modeled in Silvaco similar to the first design, and the band diagram of the device under a voltage bias of 1.45 V is plotted in Fig. 7.2. One inherent advantage to placing the slave active region outside the core of the GRINSCH waveguide is the much larger heterobarrier that prevents holes from leaking from the master active region into the slave region and reduces the current leakage. The calculated current injection efficiency is plotted in Fig. 7.3, and indeed the injection efficiency is near zero for the slave laser active region and approximately 95% for the master beyond a terminal current density of 2000 A/cm^2. Further, the quasi-Fermi level separation in the two active regions as a function of the applied bias is shown in Fig. 7.4, and in contrast to the first generation design, the master active region reaches transparency at an applied bias 0.5 V less than the slave active region would when considering only electrical injection of carriers.

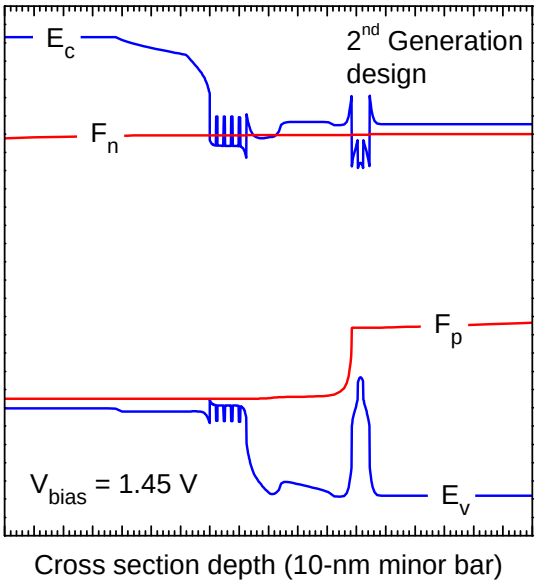

Fig. 7.2. Calculated band diagram of the second generation dual-wavelength laser design at an applied voltage bias of 1.45 V.

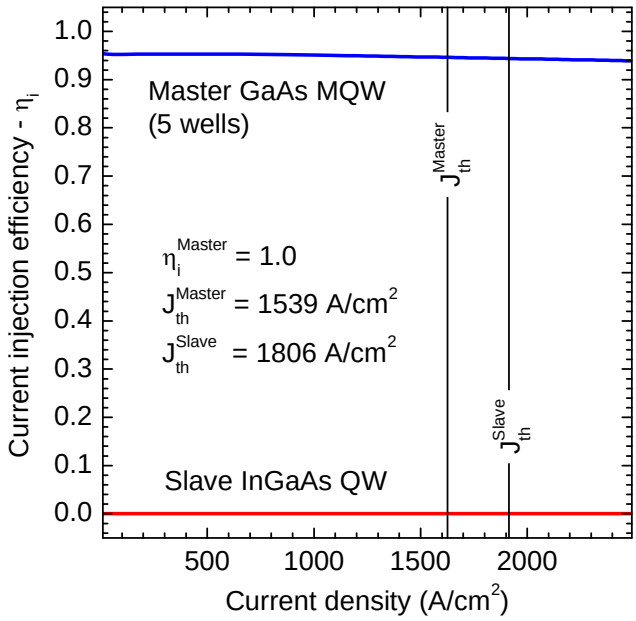

Fig. 7.3. Calculated current injection efficiency vs. applied current density for the master and slave laser active regions in the second generation dual-wavelength laser design. The theoretical thresholds assuming 100% injection efficiency for the master active region are listed, whereas the vertical threshold lines are corrected for the non-unity efficiency.

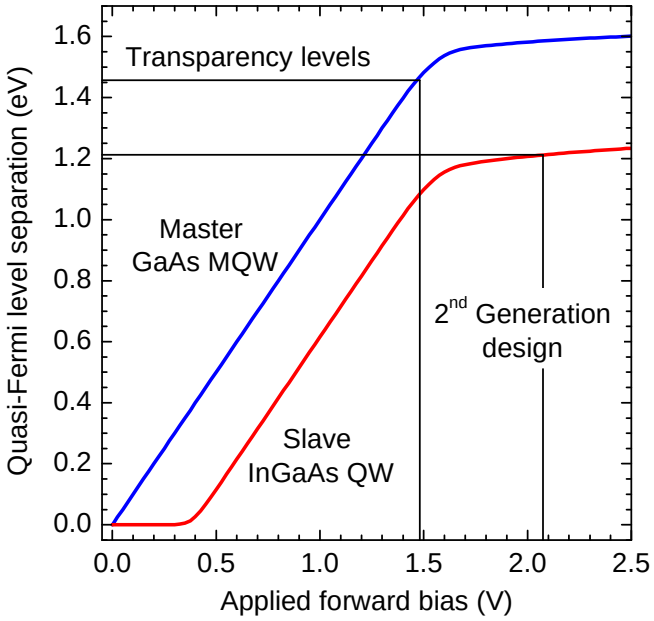

Fig. 7.4. Calculated quasi-Fermi level separation in the active regions as a function of applied bias for the second generation dual-wavelength laser design.

The theoretical thresholds of the master and slave lasers of the second generation dual-wavelength laser diode design are calculated using the internal optical pumping model and the calculated optical confinement factors. One of the assumptions used in the model is that 100% of the terminal current recombines within the master active region, and whereas it is not a good assumption for the first generation design, based on the sub-threshold injection efficiencies shown in Fig. 7.3, it is a decent assumption for the second generation design. The assumption is especially true in the aspect that negligible current leakage flows into the slave active region. With these assumptions, the calculated thresholds of the second generation design are 1539 A/cm^2 and 1806 A/cm^2 for the master and slave lasers respectively. The vertical lines in Fig. 7.3 representing the thresholds

of the master and slave laser are adjusted upward to account for the predicted 95% injection efficiency rather than the ideal 100%. A list of the parameters and results of the internal optical pumping model applied to the second generation design are listed in Table VII.III which compares the results of all the different dual-wavelength designs studied.

II. MODELING AND DESIGN OF THE THIRD GENERATION DESIGN

In the first and second generation dual-wavelength designs, the one-dimensional optical mode of the master and slave lasers in the transverse or growth dimension is the first order mode. This is the mode profile calculated and displayed in the figures of the different designs thus far. The optical confinement factor of the slave active region is slightly different for the master and slave lasers since the modes are not exactly the same due to differences in the wavelength and indices of refraction. The general profile of the two first order modes is the same in the first and second generation designs, and the waveguide is engineered in the second design to optimize the optical confinement factors to lower the modal absorption loss to the master laser while maintaining enough modal gain for the slave.

The performance and design of the dual-wavelength laser diode can be improved further by creatively broadening the waveguide and using the second order optical mode as the sustaining mode of the slave laser. This is the concept used in the design of the third generation dual-wavelength laser shown in Fig. 7.5. With the second order optical mode, the optical confinement factor is larger for

the slave active region than it is for the first order mode, enabling larger modal gain. The master laser still lases in the first order mode, and the optical confinement factor for the master laser with the slave active region can then be made small to reduce the modal absorption loss. However, it still must be large enough to optically pump the slave region. By using the first and second order modes for the master and slave lasers respectively, it is therefore possible to have a both larger and smaller optical confinement factors for the slave active region. The details of the layers of the third generation design are listed in Table VII.II, and from the calculated optical modes, the slave confinement factor in determining the master laser threshold or the modal absorption loss is 0.17% (0.68% for the second generation DWLD). For the slave laser, the optical confinement is 2.66% (0.96% for the second generation DWLD), and a larger modal gain is then obtained. The results of the theoretical internal optical pumping model suggest a possible 50% reduction in the thresholds of the master and slave lasers compared to the second generation design, and the results of the internal pumping model for the third generation design are listed in Table VII.III with the results of the other designs.

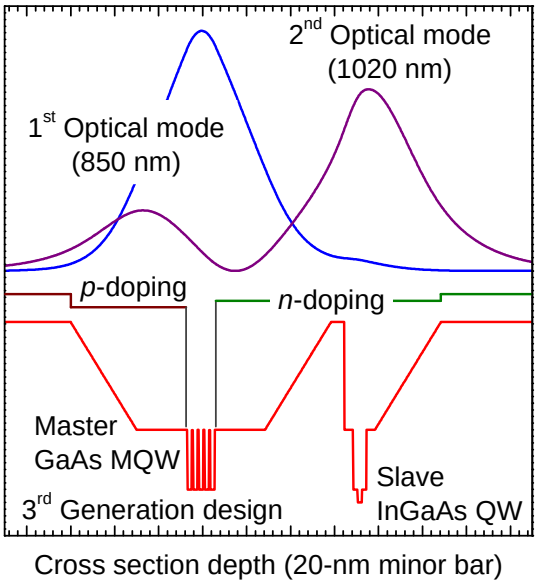

Fig 7.5. Third generation design of the dual-wavelength laser with its doped and active regions and where the second order transverse mode is utilized.

TABLE VII.II
THIRD GENERATION DWLD EPITAXIAL LAYERS / DESIGN

Description	Material	Layer thickness (nm)	Dopant concentration (cm^{-3})
p++ contact	GaAs	125	Be – Graded: 1×10^{19} to 2×10^{18}
Cladding	Graded: $Al_{0.1}Ga_{0.9}As$ to $Al_{0.7}Ga_{0.3}As$	200	Be – 2×10^{18}
Cladding	$Al_{0.7}Ga_{0.3}As$	1500	Be – 2×10^{18}
Cladding	Graded: $Al_{0.7}Ga_{0.3}As$ to $Al_{0.2}Ga_{0.8}As$	150	Be – 1×10^{17}
	$Al_{0.2}Ga_{0.8}As$	115	Be – 1×10^{17}
Active QW	GaAs	10	
	$Al_{0.2}Ga_{0.8}As$	3	
Active QW	GaAs	10	
	$Al_{0.2}Ga_{0.8}As$	3	
Active QW	GaAs	10	
	$Al_{0.2}Ga_{0.8}As$	3	
Active QW	GaAs	10	
	$Al_{0.2}Ga_{0.8}As$	3	
Active QW	GaAs	10	
	$Al_{0.2}Ga_{0.8}As$	115	Si – 1×10^{18}
Cladding	Graded: $Al_{0.2}Ga_{0.8}As$ to $Al_{0.7}Ga_{0.3}As$	150	Si – 1×10^{18}
Cladding	$Al_{0.7}Ga_{0.3}As$	30	Si – 2×10^{18}
	$Al_{0.2}Ga_{0.8}As$	20	Si – 1×10^{18}
	GaAs	10	Si – 2×10^{18}
Active QW	$In_{0.2}Ga_{0.8}As$	8	Si – 2×10^{18}
	GaAs	10	Si – 2×10^{18}
	$Al_{0.2}Ga_{0.8}As$	20	Si – 1×10^{18}
Cladding	Graded: $Al_{0.2}Ga_{0.8}As$ to $Al_{0.7}Ga_{0.3}As$	150	Si – 1×10^{18}
Cladding	$Al_{0.7}Ga_{0.3}As$	1500	Si – 2×10^{18}
Cladding	Graded: $Al_{0.7}Ga_{0.3}As$ to $Al_{0.1}Ga_{0.9}As$	200	Si – 2×10^{18}
Buffer	GaAs	400	Si – 2×10^{18}

The third generation design is modeled sub-threshold in Silvaco just as the other designs to understand the current injection of the active regions, and the results are similar to those of the second generation design. The band diagram of the design with an applied voltage bias of 1.45 V is shown in Fig. 7.6, and the quasi-Fermi separation within the active regions vs. the applied bias is plotted in Fig. 7.7. As in the second generation design, the master active region reaches transparency at a voltage bias lower than the slave active region, and the plot of the injection efficiencies in Fig. 7.8 indicates essentially zero current leakage into the slave active region, validating the assumption used in the internal optical pumping model. The injection efficiency of the master laser decreases faster than the second generation design with increased current due to the more complicated heterostructure of the third generation design. However hypothetically assuming 100% injection efficiency for the master laser, the thresholds of the master and slave lasers are 704 A/cm^2 and 817 A/cm^2 according to the internal optical pumping model. The vertical lines representing the laser thresholds in Fig. 7.8 are adjusted upwards to account for the lower injection efficiency predicted by the Silvaco results.

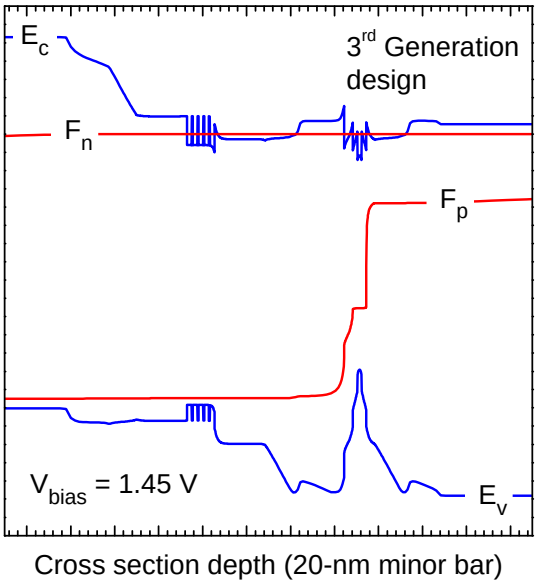

Fig. 7.6. Calculated band diagram of the third generation dual-wavelength laser design with an applied voltage bias of 1.45 V.

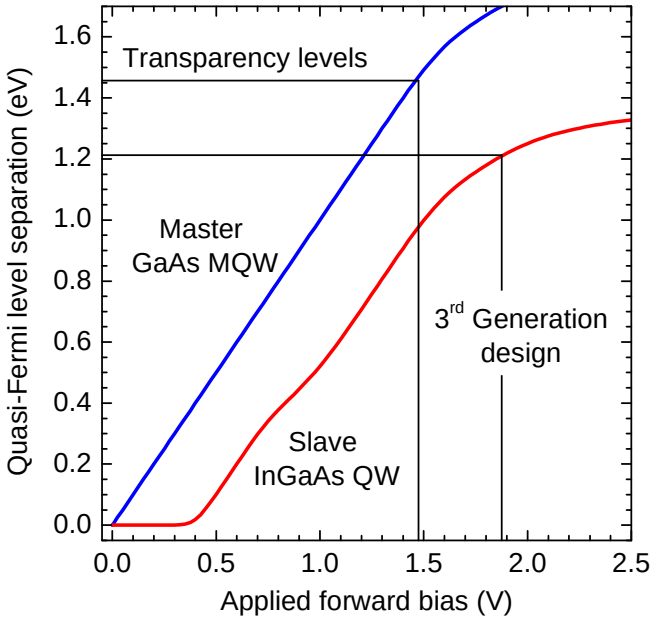

Fig. 7.7. Calculated quasi-Fermi level separation in the active regions as a function of applied bias for the third generation dual-wavelength laser design.

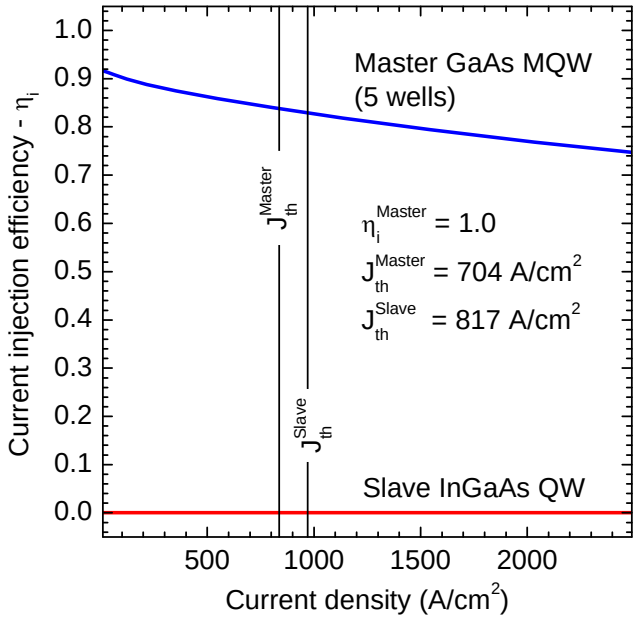

Fig. 7.8. Calculated current injection efficiency vs. applied current density for the master and slave laser active regions in the third generation design. The theoretical thresholds, assuming 100% injection efficiency for the master active region are listed, whereas the vertical threshold lines are corrected for the non-100% efficiency.

III. NOVEL DUAL-WAVELENGTH LASER DESIGN SUMMARY

The results of the internal optical pumping model for the three different dual-wavelength laser designs are listed in Table VII.III along with the results of a conventional single-wavelength multiple-quantum-well laser diode for comparison. The assumption of 100% injection efficiency for the master laser and negligible current injection into the slave active region is a fair assumption for the second and third generation designs, and the thresholds listed for these designs are somewhat realistic. Although the actual experimental thresholds will be different due to variations in growth, processing, and material parameters, the thresholds are predicted to be of the same order. For the first generation design, a significant

current leakage is present, but hypothetically if there was zero current leakage, the results of the internal optical pumping model indicate thresholds not even possible in a real device. The table therefore illustrates the development moving from each generation of designs in implementing the internal optical pumping model and reducing the laser thresholds.

TABLE VII.III
PARAMETERS AND RESULTS OF THE INTERNAL OPTICAL PUMPING MODEL APPLIED TO THE DIFFERENT DWLD DESIGNS

Component	Parameter	Conv. MQW laser	1st Gen. DWLD design	2nd Gen. DWLD design	3rd Gen. DWLD design
GaAs MQW master	Injection efficiency – η_i	1.0	1.0	1.0	1.0
	Number of wells – n_w	5	3	5	5
	Optical conf. – $\Gamma_{w,\,avg.}$ (%)	4	3.09	4.25	3.54
InGaAs slave absorption	Optical conf. – Γ_S (%)	-	2.41	0.68	0.17
	Modal absorption in QW (cm^{-1})	-	596.9	168.4	42.11
	Optical conf. – Γ_b (%)	-	2.40	1.34	0.34
	Modal absorption in GaAs barrier (cm^{-1})	-	217.1	121.2	30.76
	Total abs. loss (cm^{-1})	-	814.1	289.7	72.87
Cavity losses (850 nm)	Free carrier abs. (cm^{-1})	-	0.86	3.99	1.58
	Assumed intrinsic loss (cm^{-1})	10	10	10	10
	Mirror loss (cm^{-1})	12.04	12.04	12.04	12.04
Master laser threshold (A/cm^2)		493.3	500,120	1539	703.5
InGaAs slave gain	Injection efficiency – η_i	-	0.0	0.0	0.0
	Optical conf. – Γ_S (%)	-	2.36	0.96	2.66
Cavity losses (1020 nm)	Free carrier abs. (cm^{-1})	-	0.99	4.70	3.20
	Assumed intrinsic loss (cm^{-1})	-	10	10	10
	Mirror loss (cm^{-1})	-	12.04	12.04	12.04
Slave laser threshold (A/cm^2)		-	500,220	1806	816.7

IV. EXPERIMENTAL RESULTS

After designing and modeling the second and third generation dual-wavelength laser designs, collaboration was sought to grow the designs using molecular beam epitaxy (MBE). Unfortunately, the MBE machine at Arizona State University (ASU), which was used to grow the first generation design, was down for extensive repairs and upgrades when these later designs were ready for growth. Quotes from foundry growth services were obtained from IQE, EpiWorks, LandMark Optoelectronics, and Sumika Electronic Materials, but funding limitations prevented using these services. Outreach was made to groups at various national labs including National Institute of Standards and Technology, National Research Council Canada, and Sandia National Labs for collaboration, and while willing parties were available, their machines were also down for repairs or occupied with high priority projects. After over nine months of searching, the MBE group at the University of California, Los Angeles (UCLA), agreed to collaborate on the epitaxial growth of the second and third generation dual-wavelength laser designs. It was then another few months before the growth of the designs took place.

To determine the quality of the material grown at UCLA, two photoluminescence (PL), structures were grown immediately before the growth of the second and third generation designs. The epitaxial layers of the PL samples are listed in Table VII.IV and Table VII.V, and the PL samples were returned to ASU to do the PL measurements. An Ar-laser set at 515 nm was used to optically pump the samples, and the baseline power was 35 mW. The results of the two

samples compared to a reference sample grown at ASU demonstrated good PL signals, and the spectra are shown in Fig. 7.9. The InGaAs single quantum well 980 nm PL sample grown at UCLA had a similar design as the reference sample from ASU although with different target wavelengths, and the spectra indicate the growth of the InGaAs at UCLA is as near of quality as previous growths at ASU. The GaAs multiple-quantum-well PL sample consists of five quantum wells similar to the second and third generation designs, and the pumping intensity was therefore increased to three-times and five-times the 35 mW baseline used for the single quantum well samples to obtain the spectra plotted in Fig. 7.9. Based on the good PL and the optical quality of material grown at UCLA, the growth quality of the second and third generation dual-wavelength laser designs is considered limited only by the design of the devices and not the growth capabilities of the MBE machine.

TABLE VII.IV
GAAS MQW PL SAMPLE EPITAXIAL LAYERS / DESIGN

Description	Material	Layer thickness (nm)	Dopant concentration (cm^{-3})
Cap	GaAs	30	-
Cladding	$Al_{0.65}Ga_{0.35}As$	30	-
	$Al_{0.3}Ga_{0.7}As$	25	-
	$Al_{0.2}Ga_{0.8}As$	10	-
Active QW	GaAs	10	-
	$Al_{0.2}Ga_{0.8}As$	3	-
Active QW	GaAs	10	-
	$Al_{0.2}Ga_{0.8}As$	3	-
Active QW	GaAs	10	-
	$Al_{0.2}Ga_{0.8}As$	3	-
Active QW	GaAs	10	-
	$Al_{0.2}Ga_{0.8}As$	3	-
Active QW	GaAs	10	-
	$Al_{0.2}Ga_{0.8}As$	10	-
	$Al_{0.3}Ga_{0.7}As$	25	-
Cladding	$Al_{0.65}Ga_{0.35}As$	30	-
Buffer	GaAs	400	-

TABLE VII.V
INGAAS SQW PL SAMPLE EPITAXIAL LAYERS / DESIGN

Description	Material	Layer thickness (nm)	Dopant concentration (cm^{-3})
Cap	GaAs	30	-
	$Al_{0.3}Ga_{0.7}As$	50	-
	GaAs	50	-
Active QW	$In_{0.2}Ga_{0.8}As$	8	-
	GaAs	50	-
	$Al_{0.3}Ga_{0.7}As$	50	-
Buffer	GaAs	250	-

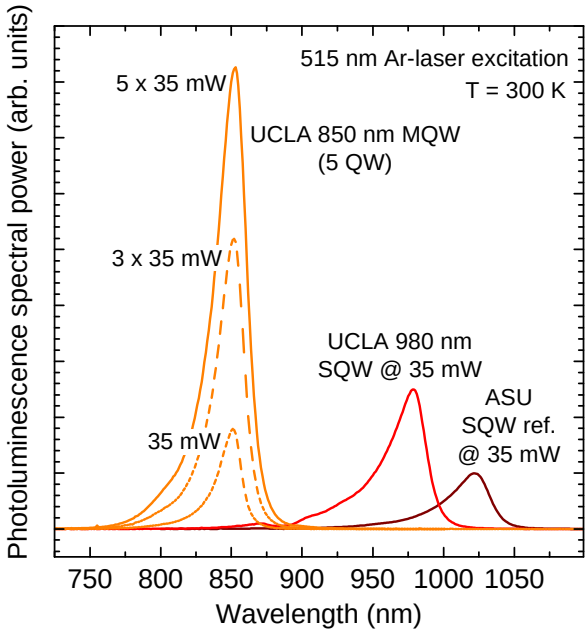

Fig. 7.9. Photoluminescence of test samples grown at UCLA to evaluate optical material quality.

The second and third generation dual-wavelength laser designs were grown at UCLA immediately after the PL samples. One change was made in the

design of the slave active region at this point to reduce the strain in the epitaxial growth. The composition of the quantum well was changed to $In_{0.2}Ga_{0.8}As$, and the thickness was reduced to 8 nm. The changes should only slightly change the experimental behavior of the designs with one of the more significant changes being the predicted wavelength moving to 980 nm from 1020 nm. After the PL measurements, samples of the grown epitaxial wafers implementing the two designs were sent to collaborators at the University of Arkansas for device processing, and the steps of the processing are found in chapter five. The processed laser diodes were then returned to ASU for testing.

The results of the second and third generation dual-wavelength designs are disappointing as laser output is only observed from the master GaAs multiple-quantum-well laser for both designs. The measured spectra of the second and third designs at one times, three times, and five times current threshold are shown in Fig. 7.10 and Fig. 7.11 respectively. Examining the spectra on a log-scale, there is no indication of any luminescence, stimulated or spontaneous, from the InGaAs slave quantum well near 980 nm at even five times injection to the master laser.

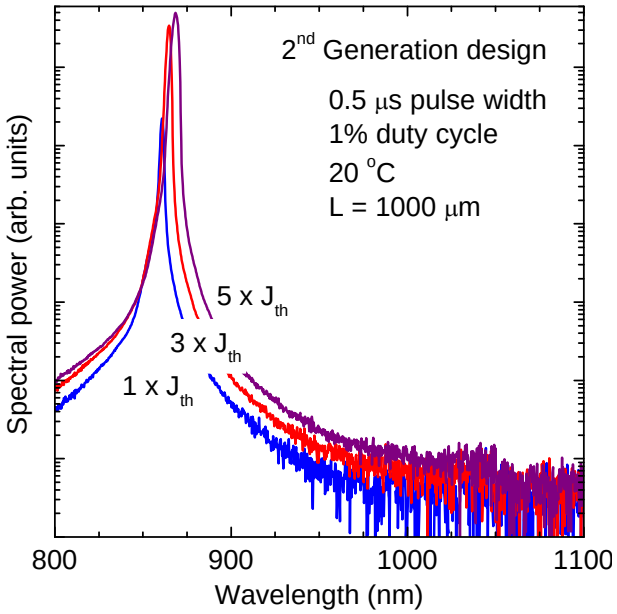

Fig. 7.10. Electroluminesence spectra of a second generation dual-wavelength laser diode showing master laser output but no emission from slave active region (J_{th} = 700 A/cm^2).

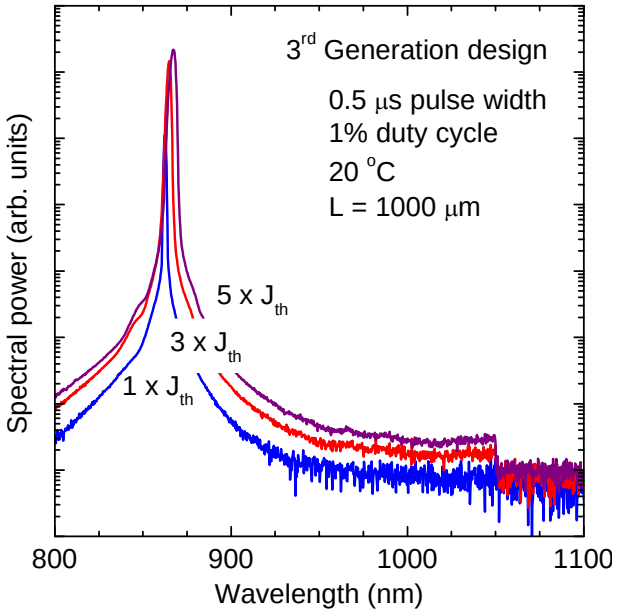

Fig. 7.11. Electroluminesence spectra of a third generation dual-wavelength laser diode showing master laser output but no emission from slave active region (J_{th} = 660 A/cm^2).

The absence of any emission from the InGaAs slave quantum well active region suggests possible issues with the material quality, and there are a couple possibilities for the shift in the material quality of the PL samples to the second and third generation designs. The first possibility is related to the designs themselves and the introduction of growth interruptions in the MBE growth of the dual-wavelength designs to satisfy thermal requirements. By positioning the slave active region outside the waveguide core and in the high Al cladding, sharp changes in the growth temperature are necessary. In growing good quality AlGaAs with MBE, growth temperatures above 580 °C are necessary to lower the incorporation of non-radiative defects in the layers, and the number of defects continues to be reduced as the temperature is increased [23], although the use of a surfactant becomes important above 620 °C [79]. However, the best growth temperature for InGaAs is much lower in the range 500-510 °C to prevent In evaporation from the layers. With the close proximity both spatially and temporally in the growth of the high Al cladding and InGaAs slave active region, interruptions in the growth are introduced prior to and after the GaAs barrier layers to accommodate the temperature ramps. These interruptions can lead to defects in the layers which then serve as non-radiative recombination centers.

The second possibility for poor quality of the InGaAs slave active region is calibration issues related to the choice of substrates used in the growth. Most of UCLA's growth experience is with two inch substrates, and two inch substrates were used for the PL samples. However, to grow the dual-wavelength structures, three inch doped-substrates provided by ASU were used. Due to the change in

substrate size, the possibility exists that the growth temperature of the InGaAs quantum well was actually much higher than the ideal growth temperature and In evaporation occurred during the growth. Related is another possibility where the longer duration of the growth at higher growth temperatures due to the addition of the master laser leads to degradation of the InGaAs layer.

To investigate the actual root cause, low temperature PL measurements are done on the second and third generation design grown wafers. At low cryogenic temperatures, non-radiative recombination due to defects is suppressed and the luminescence due to radiative recombination increases. If the growth quality of the slave InGaAs quantum well is good and the poor device performance is due to defects from the growth interruptions, than a PL signal is still expected from the InGaAs quantum well at low temperature. However, if quality issues exist with the grown InGaAs material, little or no PL signal is expected even at low temperature.

The PL spectra of the second and third generation dual-wavelength laser samples at 10 K are plotted in Fig. 7.12 and Fig. 7.13. A strong PL signal is observed from the master GaAs multiple-quantum-well region as expected with the peak wavelength blue-shifted due to the low-temperature. PL is observed from the InGaAs slave active region for both designs, but the intensity is quite low compared to the GaAs active region. Even more interesting is the broad spectrum width of the InGaAs PL, indicative of poor material quality. One possibility for the broad spectra is evaporation of In during the growth, altering the composition and forming non-uniform InGaAs islands. The non-uniformities result in various

band gaps, and at low temperatures non-homogeneous broadening results in an overall broad spectrum. One method to verify this is to reduce the pumping intensity and thus the carrier density inside the active region, and observe the spectrum width. This can be done by moving the lens that focuses the pumping excitation on the sample and adjusting the spot size on the sample while maintaining the same laser excitation power. In Fig. 7.14, two PL spectra of the third generation design are shown with the focusing lens focused and defocused. The broad width of the InGaAs spectra does not change, suggesting a non-homogenous broadening of the active region.

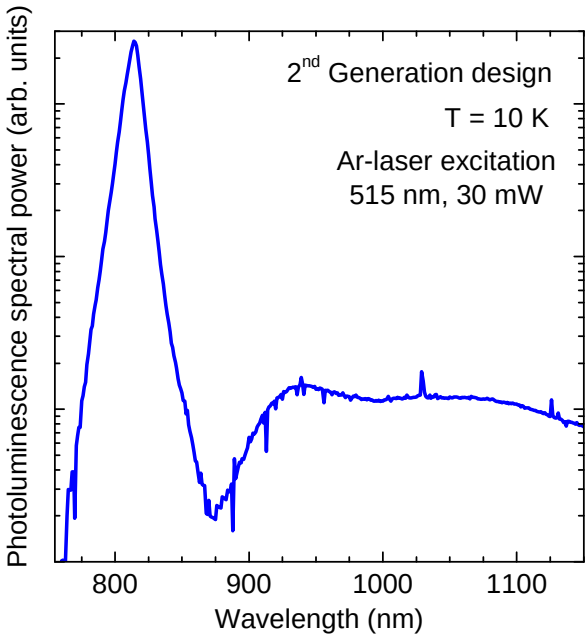

Fig. 7.12. Low-temperature photoluminescence of second generation dual-wavelength sample.

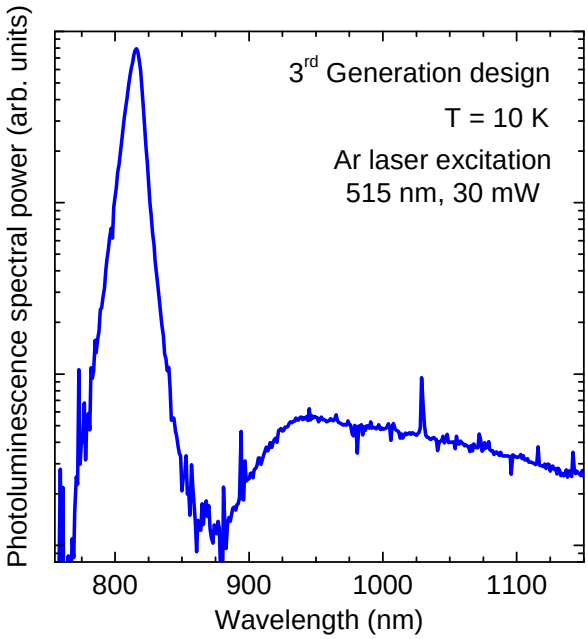

Fig. 7.13. Low-temperature photoluminescence of third generation dual-wavelength sample.

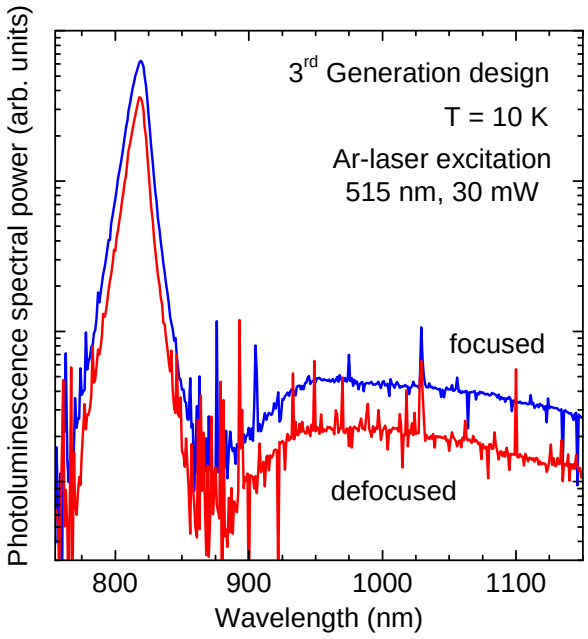

Fig. 7.14. Low-temperature photoluminescence of third generation dual-wavelength sample with focused and defocused excitation.

Based on the low temperature PL results, the poor experimental results of the second and third generation designs is due to the poor material quality of the InGaAs slave active region. At room-temperature, non-radiative recombination due to defects dominates and no luminescence is observed. Whereas the experimental results were disappointing, the results do not argue against the actual device designs, and rather challenges in the actual growth and implementation of the designs is appearing more challenging than first thought. In the future, different approaches exist for improving the growth quality. One idea is to experiment with different temperature ramps near the growth of the InGaAs slave active region to eliminate the need for growth interruptions. The risk with this approach is the introduction of defects during the growth of the high Al layers. Further investigation is needed in determining whether the temperature ramp or the growth interruptions will introduce more defects than the other. Finally another idea is to use metal organic chemical vapor deposition instead of MBE, since this method of epitaxial growth does not have the same thermal constraints for growing the various layers as does MBE and the nitrogen-purged chamber reduces the defect risks associated with growth interruptions.

V. SUMMARY OF SECOND AND THIRD GENERATION DESIGNS

Second and third generation designs of the dual-wavelength laser diode were developed to optimize the optical confinement factors of the slave active region based on the internal optical pumping theory and the results of the first generation design. In addition, the later designs seek to nearly eliminate current

leakage into the slave region so it is entirely dependent on the internal optical pumping for carrier generation. Both these aims are accomplished by positioning the slave active region in the cladding rather than the core of the waveguide, which introduces new challenges in growing the designs from a thermal perspective with MBE. Real laser diode devices grown by UCLA with the second and third generation designs do not show any room temperature luminescence associated with the InGaAs slave active region, and low temperature PL revealed problems with the material quality. If challenges with the epitaxial growth can be overcome, dual-wavelength laser output is still predicted from devices based on the two designs.

8 Conclusion

Dual-wavelength laser sources either have existing applications in, or are being investigated for use in wavelength division multiplexing, differential techniques in spectroscopy for gas and chemical sensing, multiple-wavelength interferometry, THz generation, and different uses in microelectromechanical systems and lab-on-chip microfluidic systems. In the drive for ever smaller and increasing mobile electronic devices, dual-wavelength laser output from a single semiconductor laser diode would be an enabling factor for these technologies. Tremendous advancements have been made in the device design of semiconductor lasers, and the history of these devices and the creative milestones in their development were noted earlier. The output of conventional laser diodes is however limited to a single wavelength band with possibly a few subsequent lasing modes depending on the device design.

The novel dual-wavelength internal-optically-pumped laser diodes proposed here enable laser output at two wavelength bands with large spectral separation from a single diode and waveguide structure. The shorter-wavelength master active region is positioned within the junction of a conventional diode, and carriers are injected with applied electrical current as in typical laser diodes. The longer-wavelength slave active region is positioned outside the junction and core of the waveguide but still within the guided optical mode. The internal optical field of the master laser mode then optically pumps the slave laser to its threshold, and simultaneous laser output at the two wavelengths is produced. The design in

theory enables dual-wavelength laser output for continued increase in applied current and is not limited to a certain current range or cavity length.

It was shown the critical aspects of the novel dual-wavelength design are first a method for decoupling the quasi-Fermi distributions of the two regions or preventing the redistribution of the carriers from the larger band gap active region to the smaller band gap active region, and second, optimization of the optical confinement factor of the slave active region. The internal optical pumping model developed in chapter three reveals an optimum confinement factor that results in the lowest current threshold for the slave laser and balances the modal absorption loss added to the master laser and the modal gain needed by the slave laser. Using material parameters for the GaAs and InGaAs quantum wells selected for actual device designs, the internal optical pumping model indicates a set of 5 GaAs quantum wells and a single InGaAs quantum well will result in the lowest thresholds when the cavity length is 1000 μm. The optimum optical confinement factor with these parameters for the slave laser is then ~0.7%.

A first generation design of the dual-wavelength laser diode was designed and grown prior to development of the modeling and having a full understanding of the critical aspects of the design. Broad-contact-area laser diodes were fabricated, and a new experimental setup was designed and assembled to test the laser diodes. The observed electroluminescence spectra revealed laser output only from the longer-wavelength slave laser at reasonable current; however, at extremely large current injection, multi-wavelength laser output was observed with the onset of lasing from the master GaAs multiple-quantum-well active

region. Modeling of the device post the experimental results revealed the optical confinement factor of the slave laser (~2.4% at λ = 850 nm), was too large and introduced too large of a modal absorption loss to enable lasing by the master laser at low current. Modeling of the device subthreshold using Silvaco showed a degree of current leakage into the slave active region such that the slave active region reaches transparency before the master active region, and the slave laser reaches threshold first. Then thermal effects due to the high current levels lead to increased carrier injection in the master laser active region and multi-wavelength lasing at extremely high-injection. Even though dual-wavelength lasing is observed, the first generation design does not demonstrate the predicted behavior of the internal optical pumping model.

New designs of the dual-wavelength laser diode were designed using the models to optimize the optical confinement factors and reduce the current leakage. To obtain the right optical confinement factor in the second generation design, the slave active region is positioned outside of the waveguide core, which also increases the heterobarrier separating the active regions. The subthreshold modeling, using Silvaco, predicts negligible carrier leakage into the slave active region with the increased heterobarrier, thereby forcing the slave to rely on the internal optical pumping for carrier generation. The third generation design of the dual-wavelength laser diode uses a novel concept of utilizing the second order optical mode in the transverse direction to achieve both a small and large optical confinement factor of the slave active region in determining the thresholds of the master and slave lasers respectively. The master laser uses the first order mode

which has a small slave optical confinement factor and low modal absorption loss, and the slave laser uses the second order mode which has a larger optical confinement factor and larger modal gain. By using two transverse optical modes, the internal optical pumping model, in theory, suggests a 50% reduction in the dual-laser thresholds compared to those calculated for the second generation design.

Experimental demonstration of the second and third generation dual-wavelength designs was delayed due to the scheduled renovation and upgrade of the molecular beam epitaxy (MBE), machine at Arizona State University. Multiple external groups were approached, and the MBE group at the University of California, Los Angeles agreed to help in the epitaxial growth of the second and third generation designs. Preliminary photoluminescence results indicated good quality in growing the required active regions, and samples with the second and third generation designs were grown. The experimental results of processed broad-area-contact laser diodes were disappointing as no luminescence, stimulated or spontaneous, from the slave active region was observed at room temperature. Low temperature photoluminescence measurements of actual grown samples revealed poor material quality for the InGaAs slave quantum well layer. The possible reasons for the poor growth quality is either problems with the temperature calibration in going from 2” to 3” substrates or problems with the temperature ramps and growth interruptions in transitioning from the higher-temperature AlGaAs growth of the cladding layers to the lower-temperature growth needed for the InGaAs active layer.

The experimental results of the second and third design do not disprove the ideas of the second and third generation designs of the dual-wavelength laser, and the challenge becomes one of epitaxial growth. Possibilities for improving the growth include adjustments to the temperature ramp to avoid the growth interruptions or using metal organic chemical vapor deposition, which does not have the same growth temperature constraints as MBE and is nitrogen purged to prevent defect formation. At the current time, problems related to funding and resources prevent aggressive advancement in determining the best growth conditions for the designs and experimental demonstration of the dual-wavelength laser diodes. It is hoped in the future the second and third generation dual-wavelength laser diodes will be demonstrated experimentally since stable dual-wavelength laser output from a single semiconductor laser diode would lead to new devices and advances in the applications noted herein.

REFERENCES

[1] R. D. Dupuis, "An introduction to the development of the semiconductor-laser," *IEEE J. Quant. Electron.,* vol. 23, pp. 651-657, Jun, 1987.

[2] J. P. Gordon, H. J. Zeiger and C. H. Townes, "Molecular microwave oscillator and new hyperfine structure in the microwave spectrum of NH_3," *Physical Review,* vol. 95, pp. 282-284, 1954.

[3] J. von Neumann, "Notes on the photon-disequilibrium-amplification scheme (JvN), September 16, 1953," *IEEE J. Quant. Electron.,* vol. 23, pp. 659-673, Jun, 1987.

[4] M. G. A. Bernard and G. Duraffourg, "Laser conditions in semiconductors," *Physica Status Solidi,* vol. 1, pp. 699-703, 1961.

[5] N. G. Basov, O. N. Krokhin and Y. M. Popov, "Production of negative-temperature states in P-N junctions of degenerate semiconductors," *Soviet Physics JETP-USSR,* vol. 13, pp. 1320-1321, 1961.

[6] R. N. Hall, R. O. Carlson, T. J. Soltys, G. E. Fenner and J. D. Kingsley, "Coherent light emission from GaAs junctions," *Phys. Rev. Lett.,* vol. 9, pp. 366-368, 1962.

[7] M. I. Nathan, W. P. Dumke, G. Burns, F. H. Dill and G. Lasher, "Stimulated emission of radiation from GaAs p-n junctions," *Appl. Phys. Lett.,* vol. 1, pp. 62-64, 1962.

[8] N. Holonyak and S. F. Bevacqua, "Coherent (visible) light emission from $Ga(As_{1-x}P_x)$ junctions," *Appl. Phys. Lett.,* vol. 1, pp. 82-83, 1962.

[9] T. M. Quist, R. H. Rediker, R. J. Keyes, W. E. Krag, B. Lax, A. L. Mcwhorter and H. J. Zeigler, "Semiconductor maser of GaAs," *Appl. Phys. Lett.,* vol. 1, pp. 91-92, 1962.

[10] H. Kroemer, "A proposed class of heterojunction injection lasers," *Proc. IEEE,* vol. 51, pp. 1782-1783, 1963.

[11] Z. Alferov and R. F. Kazarinov, "Semiconductor laser with electrical pumping," U.S.S.R. Patent 181737, 1963.

[12] Z. I. Alferov, V. M. Andreev, D. Z. Garbuzov, Y. V. Zhilyaev, E. P. Morozov, E. L. Portnoi and V. G. Trofim, "Investigation of influence of AlAs-GaAs heterostructure parameters on laser threshold current and realization of continuous emission at room temperature," *Soviet Physics Semiconductors-USSR,* vol. 4, pp. 1573, 1971.

[13] I. Hayashi, M. B. Panish, P. W. Foy and S. Sumski, "Junction lasers which operate continuously at room temperature," *Appl. Phys. Lett.*, vol. 17, pp. 109-111, 1970.

[14] C. H. Henry, "The origin of quantum wells and the quantum well laser," in *Quantum Well Lasers*, P. S. Zory, Ed. Academic Press, Inc., 1993, pp. 1.

[15] R. Dingle, W. Wiegmann and C. H. Henry, "Quantum states of confined carriers in very thin $Al_xGa_{1-x}As$-GaAs-$Al_xGa_{1-x}As$ heterostructures," *Phys. Rev. Lett.*, vol. 33, pp. 827-830, 1974.

[16] R. Dingle and C. H. Henry, "Quantum effects in heterostructure lasers," U.S. Patent 3 982 207, September 21, 1976.

[17] R. D. Dupuis, P. D. Dapkus, N. Holonyak, E. A. Rezek and R. Chin, "Room-temperature laser operation of quantum-well $Ga_{(1-x)}Al_xAs$-GaAs laser-diodes grown by metalorganic chemical vapor deposition," *Appl. Phys. Lett.*, vol. 32, pp. 295-297, 1978.

[18] R. D. Dupuis, P. D. Dapkus, R. Chin, N. Holonyak and S. W. Kirchoefer, "Continuous 300-degrees-K laser operation of single-quantum-well $Al_xGa_{1-x}As$-GaAs heterostructure diodes grown by metalorganic chemical vapor deposition," *Appl. Phys. Lett.*, vol. 34, pp. 265-267, 1979.

[19] R. D. Dupuis, P. D. Dapkus, N. Holonyak and R. M. Kolbas, "Continuous room-temperature multiple-quantum-well $Al_xGa_{1-x}As$-GaAs injection-lasers grown by metalorganic chemical vapor deposition," *Appl. Phys. Lett.*, vol. 35, pp. 487-489, 1979.

[20] A. Y. Cho, R. W. Dixon, H. C. Casey and R. L. Hartman, "Continuous room-temperature operation of GaAs-$Al_xGa_{1-x}As$ double-heterostructure lasers prepared by molecular-beam epitaxy," *Appl. Phys. Lett.*, vol. 28, pp. 501-503, 1976.

[21] W. T. Tsang, "Low-current-threshold and high-lasing uniformity GaAs-$Al_xGa_{1-x}As$ double-heterostructure lasers grown by molecular beam epitaxy," *Appl. Phys. Lett.*, vol. 34, pp. 473-475, 1979.

[22] W. T. Tsang, "Very low current threshold GaAs-$Al_xGa_{1-x}As$ double-heterostructure lasers grown by molecular beam epitaxy," *Appl. Phys. Lett.*, vol. 36, pp. 11-14, 1980.

[23] W. T. Tsang, F. K. Reinhart and J. A. Ditzenberger, "The effect of substrate temperature on the current threshold of GaAs-$Al_xGa_{1-x}As$ double-heterostructure lasers grown by molecular beam epitaxy," *Appl. Phys. Lett.*, vol. 36, pp. 118-120, 1980.

[24] W. T. Tsang, "Extremely low threshold (AlGa)As modified multiquantum well heterostructure lasers grown by molecular beam epitaxy," *Appl. Phys. Lett.*, vol. 39, pp. 786-788, 1981.

[25] W. T. Tsang, "Extremely low threshold (AlGa)As graded-index waveguide separate confinement heterostructure lasers grown by molecular beam epitaxy," *Appl. Phys. Lett.*, vol. 40, pp. 217-219, 1982.

[26] E. F. Schubert, L. W. Tu, G. J. Zydzik, R. F. Kopf, A. Benvenuti and R. Pinto, "Elimination of heterojunction band discontinuities by modulation doping," *Appl. Phys. Lett.*, vol. 60, pp. 466-466, 1992.

[27] Y. Arakawa and H. Sakaki, "Multidimensional quantum well laser and temperature dependence of its threshold current," *Appl. Phys. Lett.*, vol. 40, pp. 939-941, 1982.

[28] N. Kirstaedter, N. N. Ledentsov, M. Grundmann, D. Bimberg, V. M. Ustinov, S. S. Ruvimov, M. V. Maximov, P. S. Kopev, Z. I. Alferov, U. Richter, P. Werner, U. Gosele and J. Heydenreich, "Low threshold, large T_0 injection laser emission from (InGa)As quantum dots," *Electron. Lett.*, vol. 30, pp. 1416-1417, Aug 18, 1994.

[29] K. Kamath, P. Bhattacharya, T. Sosnowski, T. Norris and J. Phillips, "Room-temperature operation of $In_{0.4}Ga_{0.6}As/GaAs$ self-organised quantum dot lasers," *Electron. Lett.*, vol. 32, pp. 1374-1375, Jul 18, 1996.

[30] G. T. Liu, A. Stintz, H. Li, K. J. Malloy and L. F. Lester, "Extremely low room-temperature threshold current density diode lasers using InAs dots in $In_{0.15}Ga_{0.85}As$ quantum well," *Electron. Lett.*, vol. 35, pp. 1163-1165, July, 1999.

[31] B. E. A. Saleh and M. C. Teich, *Fundamentals of Photonics.* New Jersey: John Wiley & Sons, 2007.

[32] J. Faist, F. Capasso, D. L. Sivco, C. Sirtori, A. L. Hutchinson and A. Y. Cho, "Quantum cascade laser," *Science*, vol. 264, pp. 553-556, April, 1994.

[33] S. Nakamura, M. Senoh, S. Nagahama, N. Iwasa, T. Yamada, T. Matsushita, Y. Sugimoto and H. Kiyoku, "Room-temperature continuous-wave operation of InGaN multi-quantum-well structure laser diodes," *Appl. Phys. Lett.*, vol. 69, pp. 4056-4058, Dec, 1996.

[34] D. Jacob, N. H. Tran, F. Bretenaker and A. Le Floch, "Differential absorption measurement of methane with two spatially resolved laser lines," *Appl. Opt.*, vol. 33, pp. 3261-3264, 1994.

[35] M. W. Sigrist, Ed., *Air Monitoring by Spectroscopic Techniques.* Wiley-Interscience, 1994.

[36] R. Wolthuis, D. McCrae, E. Saaski, J. Hartl and G. Mitchell, "Development of a medical fiber-optic pH sensor based on optical absorption," *IEEE Transactions on Biomedical Engineering,* vol. 39, pp. 531-537, 1992.

[37] R. A. Wolthuis, G. L. Mitchell, E. Saaski, J. C. Hartl and M. A. Afromowitz, "Development of medical pressure and temperature sensors employing optical spectrum modulation," *IEEE Transactions on Biomedical Engineering,* vol. 38, pp. 974-981, 1991.

[38] C. Wang and C. Pan, "Two-wavelength interferometer based on a two-color laser-diode array and the second-order correlation technique," *Opt. Lett.,* vol. 20, pp. 1071-1073, 05/01, 1995.

[39] S. Hoffmann and M. R. Hofmann, "Generation of terahertz radiation with two color semiconductor lasers," *Laser & Photonics Reviews,* vol. 1, pp. 44-56, 2007.

[40] C. Wang and C. Pan, "Tunable dual-wavelength operation of a diode array with an external grating-loaded cavity," *Appl. Phys. Lett.,* vol. 64, pp. 3089-3091, 1994.

[41] C. Wang and C. Pan, "Tunable multiterahertz beat signal generation from a two-wavelength laser-diode array," *Opt. Lett.,* vol. 20, pp. 1292-1294, 06/01, 1995.

[42] S. Iio, M. Suehiro, T. Hirata and T. Hidaka, "Two-longitudinal-mode laser diodes," *IEEE Photonics Technology Letters,* vol. 7, pp. 959-961, 1995.

[43] S. D. Roh, R. B. Swint, A. M. Jones, T. S. Yeoh, A. E. Huber, J. S. Hughes and J. J. Coleman, "Dual-wavelength asymmetric cladding InGaAs-GaAs ridge waveguide distributed Bragg reflector lasers," *IEEE Photonics Technology Letters,* vol. 11, pp. 15-17, 01, 1999.

[44] S. D. Roh, T. S. Yeoh, R. B. Swint, A. E. Huber, C. Y. Woo, J. S. Hughes and J. J. Coleman, "Dual-wavelength InGaAs-GaAs ridge waveguide distributed Bragg reflector lasers with tunable mode separation," *IEEE Photonics Technology Letters,* vol. 12, pp. 1307-1309, 10, 2000.

[45] Y. Tokuda, Y. Abe, T. Matsui, N. Tsukada and T. Nakayama, "Dual-wavelength emission from a twin-stripe single quantum well laser," *Appl. Phys. Lett.,* vol. 51, pp. 1664-1666, 11/23, 1987.

[46] S. Saki, T. Aoki and M. Umeno, "InGaAsP/InP dual wavelength lasers," *Electron. Lett.,* vol. 18, pp. 17-18, 01/07, 1982.

[47] S. Sakai, T. Aoki and M. Umeno, "Dual wavelength InGaAsP/InP TJS lasers," *Electron. Lett.,* vol. 18, pp. 18-20, 01/07, 1982.

[48] H. Nagai, Y. Suzuki and Y. Noguchi, "InGaAsP/InP dual-wavelength BH laser array," *Electron. Lett.*, vol. 18, pp. 371-372, 04/29, 1982.

[49] N. Bouadma, J. C. Bouley and J. Riou, "Dual-wavelength (GaAl)As laser," *Electron. Lett.*, vol. 18, pp. 871-873, 1982.

[50] P. R. Berger, N. K. Dutta, J. Lopata, S. N. G. Chu and N. Chand, "Monolithic integration of GaAs and $In_{0.2}Ga_{0.8}As$ lasers by molecular beam epitaxy on GaAs," *Appl. Phys. Lett.*, vol. 58, pp. 2698-2700, 06/10, 1991.

[51] K. J. Beernink, R. L. Thornton and H. F. Chung, "Low threshold current dual wavelength planar buried heterostructure lasers with close spatial and large spectral separation," *Appl. Phys. Lett.*, vol. 64, pp. 1082-1084, 02/28, 1994.

[52] K. J. Beernink, D. Sun, R. L. Thornton and D. W. Treat, "Dual-wavelength AlGaAs/GaAs laser by selective removal of a quantum well in an asymmetric dual quantum well structure," *Appl. Phys. Lett.*, vol. 68, pp. 284-286, 01/15, 1996.

[53] D. Sun, D. W. Treat, K. Beernink, R. D. Bringans and G. J. Kovacs, "Red and infrared side by side semiconductor quantum well lasers integrated on a GaAs substrate," *Appl. Phys. Lett.*, vol. 73, pp. 1793-1795, 1998.

[54] M. L. Osowski, R. M. Lammert and J. J. Coleman, "A dual-wavelength source with monolithically integrated electroabsorption modulators and Y-junction coupler by selective-area MOCVD," *IEEE Photonics Technology Letters*, vol. 9, pp. 158-160, 02, 1997.

[55] M. J. Hamp and D. T. Cassidy, "Critical design parameters for engineering broadly tunable asymmetric multiple-quantum-well lasers," *IEEE J. Quant. Electron.*, vol. 36, pp. 978-983, 08, 2000.

[56] C. Lin, B. Lee and P. Lin, "Broad-band superluminescent diodes fabricated on a substrate with asymmetric dual quantum wells," *IEEE Photonics Technology Letters*, vol. 8, pp. 1456-1458, 11, 1996.

[57] S. Ikeda, A. Shimizu and T. Hara, "Asymmetric dual quantum well laser-wavelength switching controlled by injection current," *Appl. Phys. Lett.*, vol. 55, pp. 1155-1157, 1989.

[58] A. Shimizu and S. Ikeda, "Theory of asymmetric dual quantum well lasers," *Appl. Phys. Lett.*, vol. 59, pp. 765-767, 08/12, 1991.

[59] H. Wang, D. M. Bruce and D. T. Cassidy, "On the evolution of carrier distribution and wavelength switching in asymmetric multiple quantum-well lasers," *IEEE J. Quant. Electron.*, vol. 43, pp. 243-248, 03, 2007.

[60] W. Jiang, D. A. Thompson and B. J. Robinson, "Influence of facet coating on the dual wavelength operation of asymmetric InGaAs-GaAs quantum-well lasers," *IEEE J. Quant. Electron.,* vol. 41, pp. 625-629, 2005.

[61] V. Jayaraman, J. C. Geske, M. H. MacDougal, F. H. Peters, T. D. Lowes and T. T. Char, "Uniform threshold current, continuous-wave, singlemode 1300 nm vertical cavity lasers from 0 to 70 C," *Electron. Lett.,* vol. 34, pp. 1405-1407, 1998.

[62] J. F. Carlin, R. P. Stanley, P. Pellandini, U. Oesterle and M. Ilegems, "The dual wavelength Bi-vertical cavity surface-emitting laser," *Appl. Phys. Lett.,* vol. 75, pp. 908-910, 1999.

[63] M. Brunner, K. Gulden, R. Hovel, M. Moser, J. F. Carlin, R. P. Stanley and M. Ilegems, "Continuous-Wave Dual-Wavelength Lasing in a Two-Section Vertical-Cavity Laser," *IEEE Photonics Technology Letters,* vol. 12, pp. 1316-1318, 2000.

[64] R. Kaspi, A. P. Ongstad, G. C. Dente, M. L. Tilton and A. Tauke-Pedretti, "Optically Pumped Midinfrared Laser With Simultaneous Dual-Wavelength Emission," *IEEE Photon. Technol. Lett.,* vol. 20, pp. 1467, 2008.

[65] A. P. Ongstad, R. Kapsi, A. Tauke-Pedretti, J. C. Chavez, M. L. Tilton and G. C. Dente, "Controlling the outcoupled power in a dual wavelength optically pumped semiconductor laser," *Appl. Phys. Lett.,* vol. 94, pp. 241111-1, 2009.

[66] A. Tauke-Pedretti, A. P. Ongstad, M. L. Tilton, J. C. Chavez and R. Kapsi, "Power Sharing in Dual-Wavelength Optically Pumped Midinfrared Laser," *IEEE Photon. Technol. Lett.,* vol. 21, pp. 1011, 2009.

[67] S. L. Chuang, *Physics of Optoelectronic Devices.* United States: John Wiley & Sons, 1995.

[68] L. A. Coldren and S. W. Corzine, *Diode Lasers and Photonic Integrated Circuits.* United States: John Wiley & Sons, 1995.

[69] P. W. A. McIlroy, A. Kurobe and Y. Uematsu, "Analysis and application of theoretical gain curves to the design of multi-quantum-well lasers," *IEEE J. Quant. Electron.,* vol. QE-21, pp. 1958-63, 1985.

[70] T. A. DeTemple and C. M. Herzinger, "On the semiconductor laser logarithmic gain-current density relation," *IEEE J. Quant. Electron.,* vol. 29, pp. 1246-1252, 1993.

[71] J. E. A. Whiteaway, G. H. B. Thompson, P. D. Greene and R. W. Glew, "Logarithmic gain/current-density characteristic of InGaAs/InGaAlAs/InP multi-

quantum-well separate-confinement-heterostructure lasers," *Electron. Lett.*, vol. 27, pp. 340-2, 02/14, 1991.

[72] H. K. Choi and C. A. Wang, "InGaAs/AlGaAs strained single quantum well diode lasers with extremely low threshold current density and high efficiency," *Appl. Phys. Lett.*, vol. 57, pp. 321-3, 1990.

[73] H. C. Casey and M. B. Panish, *Heterostructure Lasers, Part B, Materials and Operating Characteristics.* New York: Academic Press, 1978.

[74] Anonymous *ATLAS User's Manual.* Santa Clara, CA: SILVACO International, 2007.

[75] Ioffe Physical Technical Institute. (2010). *NSM archive - Physical properties of semiconductors* [Online]. Available: http://www.ioffe.ru/SVA/NSM/Semicond/

[76] S. Adachi, Ed., *Properties of Aluminium Gallium Arsenide.* London, United Kingdom: INSPEC, the Institution of of Electrical Engineers, 1993.

[77] S. Adachi, *Properties of Group-IV, III-V and II-VI Semiconductors.* Hoboken, NJ: John Wiley & Sons, 2005.

[78] S. W. Corzine, R. H. Yan and L. A. Coldren, "Theoretical gain in strained InGaAs/AlGaAs quantum wells including valence-band mixing effects," *Appl. Phys. Lett.*, vol. 57, pp. 2835-7, 12/24, 1990.

[79] S. R. Johnson, Y. G. Sadofyev, D. Ding, Y. Cao, S. A. Chaparro, K. Franzreb and Y. -. Zhang, "Sb-mediated growth of n- and p-type AlGaAs by molecular beam epitaxy," *J. Vac. Sci. Technol. B*, vol. 22, pp. 1436, 2004.